TITLE

Non-axisymmetric evolutionary equilibrium plasma models in presence of three-dimensional conducting structures

Coordinator: Prof. Gianmaria De Tommasi

Supervisor:

Prof. Fabio Villone

Co-Supervisors:

Prof. Raffaele Albanese

Prof. Raffaele Martone

Prof. Andrea Gaetano Chiariello

Ph.D. student:
Antonio Iaiunese

List of Figures

List of Tables

Acknowledgements

The activity described in this manuscript was carried out with the assistance, guidance, and direct participation of several people with whom I was honored to collaborate.

I want to express my gratitude to my supervisor, Prof. Fabio Villone, and co-supervisors, Prof. Raffaele Albanese, Prof. Andrea Gaetano Chiariello, and Prof. Raffaele Martone, for their invaluable guidance, support, and encouragement throughout my doctoral studies. Their insights and expertise have been instrumental in the development of my research, and I consider myself fortunate to have had them as my mentors. I am also grateful to Prof. Salvatore Ventre and Prof. Vincenzo Paolo Loschiavo, for their time, expertise, and feedback, which were extremely valuable to the development of my thesis.

I would like to thank the professors and staff at the University of Napoli Federico II and the University of Padova involved in the PhD Course in Fusion Science and Engineering, for their support and efforts in the efficient organization of the Course, and my fellow doctoral colleagues in the DIETI department and CREATE Consortium, for their friendship and collaboration. I am grateful for their companionship along this journey. I would also like to thank the researchers at the IPP in Prague, including Dr. David Tskhakaya, Dr. Vadim Yanovskiy, the team at the Theory and Modelling Department, and the COMPASS team. They provided me with fundamental help for this activity, and enriched my visit to Prague with their insights and expertise.

I am also grateful to my closest friends, for their friendship and companionship, throughout all these years.

<div align="center">To my Family</div>

I am immensely grateful to my beloved family, my mother Stefania, my father Nicola, and my sister Giusi, for their constant love, support, and encouragement, not only for my doctoral studies, but throughout my entire life. I love you so much, and I could not have done any of this without them.

Contents

Acronyms

ASDEX Axially Symmetric Divertor EXperiment.

BC Boundary Conditions.

BH Big Hole.

COMPASS COMpact ASSembly.

CS Central Solenoid.

DEMO DEMOnstration power plant.

DN Dirichlet Null conditions.

DTT Divertor Tokamak Test.

ELM Edge-Localized Mode.

EPR External Partial Rogowski.

FEM Finite Element Method.

ICF Inertial Confinement Fusion.

IPR Internal Partial Rogowski.

ITER International Thermonuclear Experimental Reactor.

JET Joint European Torus.

JT-60 Japan Torus-60.

LCMS Last Closed Magnetic Surface.

MCF Magnetic Confinement Fusion.

MHD Magneto-Hydro-Dynamics.

NBI Neutral Beam Injectors.

NM Neumann conditions from Measurements.

NN Neumann Null conditions.

NRMSE Normalized Root Mean Square Error.

ODE Ordinary Differential Equation.

PF Poloidal Field.

PM Protruding Mesh.

RFP Reversed Field Pinch.

RFX Reversed Field eXperiment.

RHS Right-Hand Side.

SH Small Holes.

SOL Scrape-Off Layer.

SPARC Smallest/Soonest Possible ARC.

TF Toroidal Field.

VDE Vertical Displacement Event.

W7-X Wendelstein 7-X.

Summary

Nuclear fusion is a process that involves the combination of two atomic nuclei to form a heavier atomic nucleus, with the release of a large amount of energy. This process happens at the heart of stars, and represents the potentially future main source of energy for the mankind. One of the main challenges in the development of a nuclear fusion reactor is the confinement of plasma. Magnetic confinement is one of the most promising methods for this purpose, and is based on the use of magnetic fields to confine plasma in a toroidal chamber.

Tokamaks are machines that represent nowadays the main approach to the development of a nuclear fusion reactor. In a Tokamak, the plasma is confined by means of a magnetic field generated by a set of coils and the plasma itself.

One of the main problems associated with Tokamaks are the disruptions phenomena, events in which the plasma suddenly loses stability and collapses. Disruptions can cause serious damage to the structure, and their control (or mitigation) represents one of the main challenges to be overcome for the development of a safe and efficient nuclear fusion reactor. The magnetic forces acting on the device vessel during a disruption are of great importance for the estimation of the damage suffered by the structure. However, direct measurement of these forces is difficult and complicated.

In this PhD thesis, the study and implementation of a model to calculate the total net magnetic forces acting on the vessel during a disruption, from information obtained only by magnetic diagnostics, is proposed. The approach can be applied on many fusion devices, here it has been used to evaluate the forces on the COMPASS Tokamak, and the results have been compared with CarMa0NL, an advanced and well-established code. Also experimental data, from the COMPASS shots database, have been used for the method, and the results will be discussed.

The candidate's main contribution has been in the development of the model that allows to calculate the forces from the knowledge of the magnetic measurements, as well as in carrying out the tests aimed at evaluating the

1

implementation of the method, and applying it to the COMPASS device.

The thesis is organized as follows:

- Chapter 1: Controlled thermonuclear fusion. In this chapter, an highlight on the nuclear fusion, the main plasma models, and the most important fusion devices will be given.

- Chapter 2: Tokamaks. In this chapter, an insight on the Tokamaks devices will be given.

- Chapter 3: Equilibrium codes. This chapter contains an overview of the equilibrium codes necessary to the model here presented, along with an additional tool, capable to perform an interpolation of the flux density field through the use of the Chebyshev polynomials.

- Chapter 4: Force calculation. This chapter is focused on the description of the model and details about its numerical implementation.

- Chapter 5: Model validation. In this chapter, a parametric analysis on the numerical implementation of the model will be shown, along with the results obtained from the comparison with the CarMa0NL tool.

- Chapter 6: Results. In this chapter, some applications on simulations and real diagnostics data will be shown.

- Conclusions.

1

Controlled thermonuclear fusion

T HIS chapter is an introduction about the principles of nuclear fusion reactions and plasma models, with a focus on the Magnet-Hydro-Dynamic model. Then, a short description of the Reversed Field Pinchs and Stellarator devices will be given.

1.1 Principles of nuclear fusion

The nuclear fusion is a process that takes place when atomic nuclei come close together enough to overcome their natural repulsion, collide and fuse, forming a heavier nucleus, with a total mass reduced. This rearrangement leads to an energy release in the form of kinetic energy, subdivided between the particles of the nuclei involved, the *nucleons*. The quantity of energy is strongly dependent by such particles. It is the fundamental process that powers the sun and other stars.

Into the sun, the reactions happen between the nuclei of hydrogen isotopes, that forms a compound of charged particles, the *plasma*. The fusion is provided by the high temperature and elevate pressures, due to the mass of the star, and generate helium nuclei. Fusion obtained in this way is called thermonuclear; obviously, also the gravity of the star is involved.

An example of fusion reaction of such kind is the one between deuterium nuclei $(D-D)$ [1], an isotope of hydrogen, where the nucleons are a proton and a neutron:

$$D^2 + D^2 \longrightarrow He^3 + n^1 + 3.27\,\text{MeV}$$
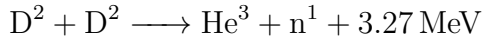
This reaction produces an helium nucleus (He), a neutron (n) and 3.27MeV of energy. Another possible reaction is the following:

$$D^2 + D^2 \longrightarrow T^3 + H^1 + 4.03\,\text{MeV}$$
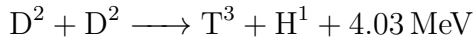
where T indicates the tritium, another hydrogen (H) isotope. Other examples are the reaction deuterium-helium ($D-He^3$) and deuterium-tritium ($D-T$):

$$D^2 + He^3 \longrightarrow He^4 + H^1 + 18.3\,\text{MeV}$$
$$_1D^2 + {}_1T^3 \longrightarrow {}_2He^4 + {}_0n^1 + 17.6\,\text{MeV}$$
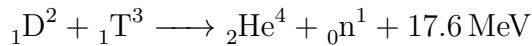
This last reaction produces an energy of 17.6MeV, subdivided between the helium nucleus $_2He^4$ (α particles) and the neutron, respectively with 3.5MeV and 14.1MeV. Then, the neutron contains most of the total energy released.

In order to achieve fusion artificially and maintain it long enough to produce energy, certain challenging conditions must be met. Firstly, to initiate the reaction, the electrostatic repulsion (Coulomb barrier) between nuclei must be overcome [1]. This can be achieved by raising the atoms to extremely high temperatures (in the order of tens or hundreds of millions of degrees). Naturally, there is no container capable of holding plasma at such temperatures, so plasma confinement techniques have been developed to prevent contact with the walls: Inertial Confinement Fusion (ICF) and Magnetic Confinement Fusion (MCF).

The ICF involves the compression of a small pellet of fusion fuel to high density and temperature in a short time span [2]. This compression is typically achieved through the application of intense laser beams. The energy from the beams is absorbed by the outer layers of the pellet, causing an implosion of the remaining fuel. The high-pressure and temperature conditions generated during this implosion enable fusion reactions to occur. While ICF has shown promise, for example providing the first-ever fusion reaction with an energy production greater than the one necessary to trigger it [3], it faces significant challenges in achieving sustained fusion reactions. The compression process must be highly uniform to avoid instabilities, and the energy losses due to radiation and lasers must be minimized. Additionally, target fabrication and repetition rates of experiments remain major technical obstacles.

The MCF relies on the use of strong magnetic fields to confine and control a hot plasma, for a relatively long time with low density. The primary

advantage of MCF lies in its potential for sustained and steady-state operation, making it an attractive approach for future power plants. On the other hand, the complexity and the cost of building and maintaining the necessary infrastructure is an actual problem. The approach involved in this thesis' activity is the MCF.

Furthermore, a positive energy balance condition must be added. The energy produced by the reaction over a certain period of time should be sufficient to compensate for both plasma losses and the energy required to heat the plasma itself [1]:

$$Q = \frac{P_{produced}}{P_{supplied} + P_{losses}} > 1 \tag{1.1}$$

A parameter that describes the losses is the *confinement time τ_E*, defined as:

$$P_{losses} = \frac{W}{\tau_E} \tag{1.2}$$

where W is the energy in the plasma at a certain instant.

Fusion reactions are characterized by their activity's dependence on temperature. To discuss this matter, let's introduce a definition. The *cross-section (σ)* is a parameter that describes the fusion event's activity rate. It indicates the area of an equivalent surface that, when intercepted by a reacting particle, results in the reaction. Consequently, the *reaction rate*, which is the average number of reactions per unit of time and volume, is denoted by $\langle \sigma v \rangle$, where v is the particle velocity distribution. It can be shown that among the fusion reactions depicted, the D−T reaction has the highest cross-section (and thus the highest reaction rate) at the lowest temperature (Fig. 1.1). The main drawback of the D−T reaction is related to tritium. It is radioactive, and while deuterium is widely available in seawater, tritium is rare and must be produced somehow. The solution lies in a lithium reaction, abundant in nature, with a neutron:

$$^{17}\text{Li} + \text{n} \longrightarrow {}^{4}\text{He} + \text{T} + 4.86\,\text{MeV}$$

In this way, problems related to tritium transport can be avoided by producing it locally.

An appropriate treatment of the powers involved is provided by the fundamental *Lawson criterion*:

$$nT\tau_E > 3 \cdot 10^{21} m^{-3} keV s \tag{1.3}$$

where T is the temperature and n is the density of both deuterium and tritium (assuming $n_D = n_T = n$). The (1.3) represents the ignition condition
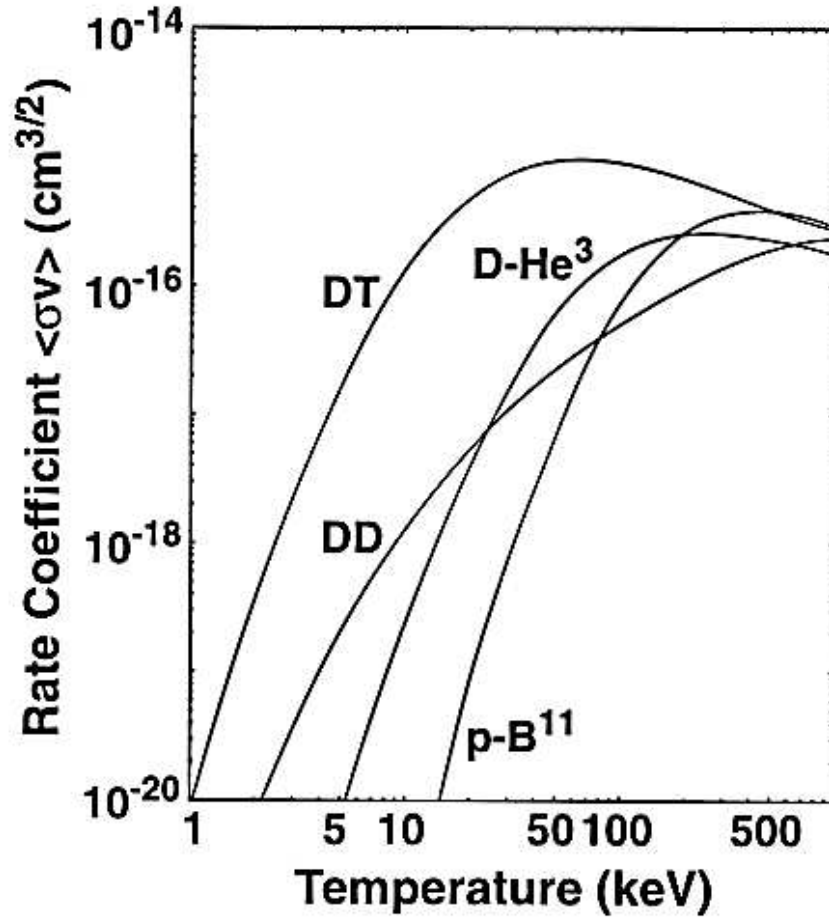
Figure 1.1: Reaction rate as a function of temperature [4]

as it clearly expresses the requirements for density, temperature, and confinement time to achieve a favorable power balance. From the criterion's perspective, the two confinement techniques have almost opposite characteristics: ICF relies on achieving high density in a very short time, while MCF aims for longer confinement times at very high temperatures and lower density. It can be understood that τ_E is a critical parameter when considering the use of magnetic confinement techniques.

It is essential to note that the Lawson criterion, as presented, only takes into account the power used to heat the plasma, the power produced by fusion reactions, and the plasma losses. It does not consider the entire set of powers involved that are crucial for reactor operation, such as magnetic field coil and sensor power supplies, cooling systems, and more. Today, more complex definitions are considered.

6

1.2   Magneto-Hydro-Dynamics model

The plasma is composed of fully ionized matter, exhibiting specific properties that allow it to be referred to as the "fourth state" of matter. The term "plasma" was proposed by Irving Langmuir in 1927. To provide a more rigorous definition, plasma is a quasi-neutral gas of charged particles that exhibit collective behavior. Being an ionized gas, the charged particles interact with each other and the external environment through electromagnetic fields. All physical models of plasma rely on a set of fundamental equations derived from mechanics, fluid dynamics, and electromagnetism [5].

A first model is the particle model, which deals with characterizing the trajectory of a particle in the plasma when it is subjected to an electromagnetic field, either uniform or variable, describing the velocity drift acting on the charges. This model is also capable to describe the *mirror trapping* phenomena, used by the first fusion devices, and abandoned due to inevitable problems into the particles confinement [6].

A second model is the statistical model, within the framework of the so-called kinetic theory of plasma. This theory aims to study the plasma using statistical modeling of particles, described through their positions and velocities [1].

From the statistical model, it is possible to derive a set of equations useful to introduce the Magneto-Hydro-Dynamics (MHD) model. This model treats the plasma as a conducting fluid interacting with magnetic fields; unlike other models, it does not treat ions and electrons separately. The "philosophy" behind MHD is to identify a state of the plasma, specified by the mass density ρ, temperature T, velocity $\boldsymbol{v}$ and magnetic flux density $\boldsymbol{B}$ at each point $\boldsymbol{r}$ in space and at every instant t. The following assumptions are made:

- neutral plasma, i.e., $n_e = n_i \equiv n$, where n_i and n_e are respectively ions and electrons concentrations and the electron mass is neglected;

- thermodynamic equilibrium, i.e., ions and electrons at the same temperature T;

- collisionless plasma;

- low-frequency and non-relativistic phenomena.

From these hypothesis, it is possible to obtain the equations listed below, that constitute the set of *MHD model equations*.

$$\frac{\partial \boldsymbol{B}}{\partial t} = \boldsymbol{\nabla} \times (\boldsymbol{v} \times \boldsymbol{B}) + \eta \boldsymbol{\nabla}^2 \boldsymbol{B} \qquad \text{with} \qquad \eta = 1/(\mu_0 \sigma) \qquad (1.4)$$

$$\rho \frac{d\boldsymbol{v}}{dt} = -\nabla p + \frac{1}{\mu_0}(\boldsymbol{\nabla} \times \boldsymbol{B}) \times \boldsymbol{B} \tag{1.5}$$

$$\frac{\partial \rho}{\partial t} + \boldsymbol{\nabla} \cdot (\rho \boldsymbol{v}) = 0 \tag{1.6}$$

$$p = (k_B/m)\rho T \tag{1.7}$$

$$(\frac{\partial}{\partial t} + \boldsymbol{v} \cdot \boldsymbol{\nabla})(\frac{p}{\rho^\gamma}) = 0 \tag{1.8}$$

$$\boldsymbol{\nabla} \cdot \boldsymbol{B} = 0 \tag{1.9}$$

Here, η is the magnetic diffusivity, μ_0 is the vacuum permeability, σ is the electrical conductivity, p is the plasma pressure, k_B is the Boltzmann constant, m is the average particle mass and γ is the adiabatic expansion coefficient.

Eqs. from (1.4) to (1.9) are respectively the induction equation, the force balance, the mass conservation, the state equation, the adiabatic equation and the solenoidality of $\boldsymbol{B}$. It is beyond the focus of this thesis to study in detail this set of equations, and they are here listed only for clarity and completeness.

This set of nonlinear equation can be written as 9 scalar equation, since (1.9) can be derived from the others, with 9 unknowns, namely the components of the vector fields $\boldsymbol{B}$ and $\boldsymbol{v}$, and additionally, the scalar fields p, ρ, and T. Moreover, from these equations, other quantities of interest such as the current density $\boldsymbol{J}$ and the electric field $\boldsymbol{E}$ can be derived. There are also advanced versions of the MHD model, like the relativistic MHD model used in astrophysics. In this context, only the so-called *ideal MHD* will be described.

The MHD model provides valuable insights into the plasma, and one of the first aspects is related to the pressure balance. Firstly, let's recall the Ampère-Maxwell equation, where the displacement current has been neglected. This is allowed by the hypothesis made earlier:

$$\boldsymbol{\nabla} \times \boldsymbol{B} = \mu_0 \boldsymbol{J} \tag{1.10}$$

This equation allows to obtain:

$$\boldsymbol{J} \times \boldsymbol{B} = \frac{1}{\mu_0}(\boldsymbol{\nabla} \times \boldsymbol{B}) \times \boldsymbol{B} \tag{1.11}$$

Using the vector identity:

$$\boldsymbol{\nabla}(\boldsymbol{V_1} \cdot \boldsymbol{V_2}) = (\boldsymbol{V_2} \cdot \boldsymbol{\nabla})\boldsymbol{V_1} + (\boldsymbol{V_1} \cdot \boldsymbol{\nabla})\boldsymbol{V_2} + \boldsymbol{V_1} \times (\boldsymbol{\nabla} \times \boldsymbol{V_2}) + \boldsymbol{V_2} \times (\boldsymbol{\nabla} \times \boldsymbol{V_1}) \tag{1.12}$$

where $\boldsymbol{V_1}$ and $\boldsymbol{V_2}$ are two generic vectors, and by setting $\boldsymbol{V_1} = \boldsymbol{V_2} = \boldsymbol{B}$, considering $\boldsymbol{B} \cdot \boldsymbol{B} = B^2$, the following expression for (1.11) is obtained:

$$\boldsymbol{J} \times \boldsymbol{B} = -\boldsymbol{\nabla}\left(\frac{B^2}{2\mu_0}\right) + \frac{(\boldsymbol{B} \cdot \boldsymbol{\nabla})\boldsymbol{B}}{\mu_0} \tag{1.13}$$

The term $B^2/2\mu_0$ represents the *magnetic pressure*, as its gradient is a force. This pressure combines with the kinetic pressure p to provide the total pressure:

$$\text{Total Pressure} = \text{Magnetic Pressure} + \text{Kinetic Pressure} = \frac{B^2}{2\mu_0} + p \tag{1.14}$$

The relative importance of these two terms is given by the *beta* parameter:

$$\beta = \frac{\text{Kinetic Pressure}}{\text{Magnetic Pressure}} = \frac{p}{B^2/2\mu_0} = \frac{2\mu_0 p}{B^2} \tag{1.15}$$

Tokamak devices are designed so that β takes on relatively small values, indicating that magnetic pressure dominates over kinetic pressure.

The other term of (1.13), $(\boldsymbol{B} \cdot \boldsymbol{\nabla})\boldsymbol{B}/\mu_0$, is the *radial magnetic tension*, which can also be written as:

$$\frac{(\boldsymbol{B} \cdot \boldsymbol{\nabla})\boldsymbol{B}}{\mu_0} = \frac{B^2}{\mu_0}(\boldsymbol{b} \cdot \boldsymbol{\nabla})\boldsymbol{b} \qquad \text{where} \qquad \boldsymbol{b} = \boldsymbol{B}/B \tag{1.16}$$

It applies at points where there is a curvature of the magnetic field. In fact, it can be shown that:

$$(\boldsymbol{B} \cdot \boldsymbol{\nabla})\boldsymbol{B} = -\frac{B^2}{R_c}\hat{\boldsymbol{R}}_{\boldsymbol{c}} \tag{1.17}$$

where R_c is the radius of curvature, and $\hat{\boldsymbol{R}}_{\boldsymbol{c}}$ is the radial unit vector.

Other characteristics of the plasma can be derived from (1.4). To describe the importance of the two terms on the right-hand side of the equation, the *Reynolds number* (Re) is defined as a parameter to compare their magnitudes, considering characteristic physical dimensions:

$$Re = \frac{vB/L}{\eta B/L^2} = \frac{Lv}{\eta} = \mu_0 \sigma L v \tag{1.18}$$

where L and v are typical length and velocity values in the plasma. In (1.18), spatial dependence is accounted for through L, and there is no temporal dependence due to the assumption of stationarity. Qualitatively, the Reynolds number indicates the relative importance of plasma conductivity and motion

in determining the evolution of the magnetic field $\boldsymbol{B}$. Two limiting cases can be identified: $Re << 1$ and $Re >> 1$.

For $Re << 1$, the resistivity term dominates, and the relation reduces to the *diffusion equation*:

$$\frac{\partial \boldsymbol{B}}{\partial t} \approx \eta \boldsymbol{\nabla}^2 \boldsymbol{B} \tag{1.19}$$

This case is of little interest for fusion applications, whereas more interesting is the case $Re >> 1$ (ideal MHD), where the velocity term prevails:

$$\frac{\partial \boldsymbol{B}}{\partial t} \approx \boldsymbol{\nabla} \times (\boldsymbol{v} \times \boldsymbol{B}) \tag{1.20}$$

This behavior governs the plasma's operation. Let's consider the magnetic flux through a surface S bounded by a curve C:

$$\psi = \int_S \boldsymbol{B} \cdot d\boldsymbol{S} \tag{1.21}$$

where $\boldsymbol{S}$ is the normal vector to the surface. For simplicity, the time dependence has been omitted. The time variation of the magnetic flux can be due to changes in time for $\boldsymbol{B}$ or due to motion of the surface S. The convective derivative of the flux is given by:

$$\frac{d\psi}{dt} = \int_S \frac{\partial \boldsymbol{B}}{\partial t} \cdot d\boldsymbol{S} + \int_C \boldsymbol{B} \cdot (\boldsymbol{v} \times d\boldsymbol{l}) \tag{1.22}$$

where $\boldsymbol{l}$ is the tangent vector to curve C. Substituting equation (1.20) in the first term of right-hand side (RHS) and rearranging the vector product with the scalar product for the second term, the following is obtained:

$$\frac{d\psi}{dt} = \int_S \boldsymbol{\nabla} \times (\boldsymbol{v} \times \boldsymbol{B}) \cdot d\boldsymbol{S} + \int_C (\boldsymbol{B} \times \boldsymbol{v}) \cdot d\boldsymbol{l} \tag{1.23}$$

Finally, using Stokes' theorem on the second term on the RHS:

$$\frac{d\psi}{dt} = \int_S \boldsymbol{\nabla} \times (\boldsymbol{v} \times \boldsymbol{B}) \cdot d\boldsymbol{S} - \int_S \boldsymbol{\nabla} \times (\boldsymbol{v} \times \boldsymbol{B}) \cdot d\boldsymbol{S} = 0 \tag{1.24}$$

In other words, in a highly conductive plasma, the magnetic flux through any surface is conserved. This result is known as *Alfvén's theorem*. The result implies the "freezing-in" of magnetic field lines, meaning that when a surface (e.g., a group of particles) moves, the magnetic field lines move with it, keeping the magnetic flux constant. This property, also common to superconducting materials, is also referred to as the superconductivity condition of the plasma.

The model is very suitable for studying equilibrium and stability in the plasma. Firstly, it is essential to specify the required shape of the plasma for it to be in equilibrium. Without going into details, it can be demonstrated that a magnetic field in a finite volume cannot have simply connected geometry for lines (*hairy ball theorem*). The simplest geometry compatible with this theorem is the toroidal shape. This solution is adopted in the majority of present-day devices such as Tokamaks, Reversed Field Pinchs (RFPs) and Stellarators. In practice, geometries with axial symmetry are often used; for example Tokamaks and RFPs, as shown in Fig. 1.2, where also the quasi-toroidal coordinates system, commonly used in such devices, is reported. By
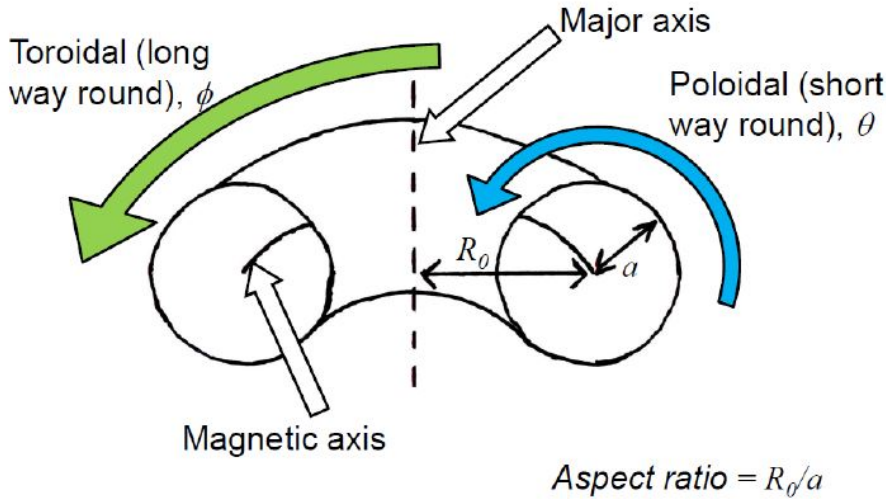
Figure 1.2: Toroidal geometry, with a quasi-toroidal coordinate system

using a quasi-toroidal reference system, it is possible to define a toroidal direction ϕ, a poloidal direction θ, and a radial direction R with respect to the axis of symmetry. In the figure, the torus has a circular cross-section with a major radius R_0 and a minor radius a. The ratio between R_0 and a is defined as the *aspect ratio*. To achieve confinement, the magnetic field must possess two components, a toroidal component B_ϕ and a poloidal component B_θ. The field lines form concentric toroidal-shaped surfaces, called *magnetic flux surfaces*. In an asymmetric toroidal geometry, the *rotational transform* ι can be defined as follows:

$$\frac{\iota}{2\pi} = \frac{d\Psi}{d\Phi} \tag{1.25}$$

where Ψ and Φ are the poloidal and toroidal magnetic flux, respectively. The

safety factor q is then defined as:

$$q = \frac{2\pi}{\iota} \qquad (1.26)$$

which represents the ratio between the number of toroidal and poloidal turns associated with the evolution of the field line. If q is rational, the line closes after a certain number of turns (*closed line*); if q is irrational, the line "winds" around the torus without ever closing, forming a surface (*ergodic line*). For toroidal systems with high aspect ratio, q can be calculated as follows:

$$q = \frac{r}{R_0} \frac{B_\phi}{B_\theta} \qquad (1.27)$$

Now, let's derive the equilibrium equation under static conditions, starting with the one-dimensional case. The (1.5), neglecting the force of gravity and under the assumptions made, reduces to:

$$\boldsymbol{J} \times \boldsymbol{B} = \boldsymbol{\nabla} p \quad \text{where} \quad \boldsymbol{J} = \frac{1}{\mu_0} (\boldsymbol{\nabla} \times \boldsymbol{B}) \qquad (1.28)$$

Let's suppose to deal with an indefinite cylindrical structure and use appropriate cylindrical coordinates (r and θ directed orthogonally to the cylinder axis, z coinciding with the axis). Let's assume that all quantities depend only on r. Using (1.13) and writing the field with two components B_z and B_θ, the magnetostatic equation can be written as the following Ordinary Differential Equation (ODE):

$$\frac{d}{dr} \left(\frac{B_z^2 + B_\theta^2}{2\mu_0} + p \right) + \frac{B_\theta^2}{\mu_0 r} = 0 \qquad (1.29)$$

The first term represents the total pressure gradient, consisting of magnetic and kinetic pressure, and the second term represents the magnetic tension. Both terms, written in vector form, are directed along the r direction. Two particular configurations can be identified: *Theta-pinch* and *Z-pinch*.

In the Theta-pinch configuration, the θ component of the field is zero, resulting in:

$$\frac{d}{dr} \left(\frac{B_z^2}{2\mu_0} + p \right) = 0 \quad \rightarrow \quad p + \frac{B^2}{2\mu_0} = \text{constant} \qquad (1.30)$$

This means that the total pressure is independent of the radius, and an increase in p coincides with a reduction in B. This field configuration can be obtained through a current in the θ direction.

In the case of Z-pinch, the field is directed along θ, resulting in a plasma current in the z direction. In this case, the kinetic pressure is balanced by the magnetic tension associated with the radius curvature. Alternatively, the plasma current can be modeled as a current flow in the same direction, which compresses due to the Lorentz force. It can be derived that the behavior of the kinetic pressure in the radial direction is decreasing, and by imposing that the pressure at the plasma boundary is zero ($p(a) = 0$, otherwise, the plasma would diffuse), it is possible to calculate the expression for the pressure on the axis:

$$p(0) = \frac{\mu_0 I^2}{4\pi^2 a^2} \tag{1.31}$$

Theta-pinch and Z-pinch field configurations are useful for understanding plasma instability problems within cylindrical structures.

A case of particular interest for applications is the equilibrium in toroidal systems with axial symmetry (2D).

Before introducing the study of the actual equilibrium, it is useful to express the magnetostatic equations in a convenient form. To do so, an appropriate cylindrical coordinate system (r, ϕ, z) is chosen, as shown in Fig. 1.3. The assumption of axial symmetry implies that $\frac{\partial}{\partial \phi} = 0$. Additionally, it
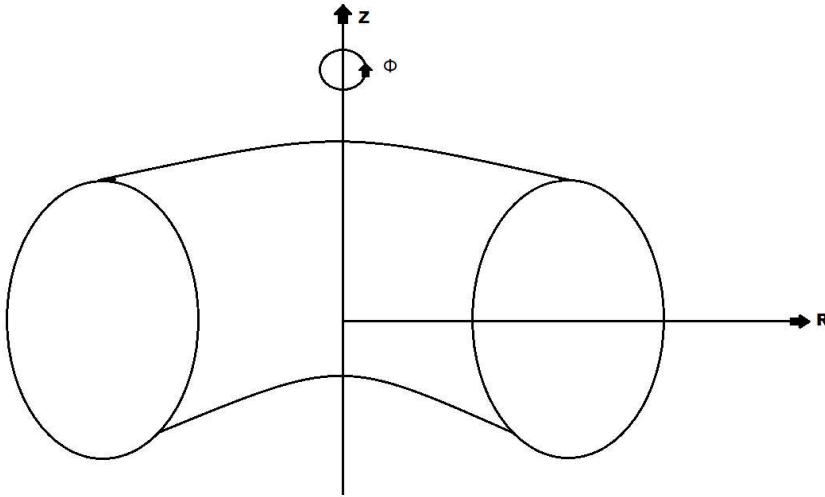
Figure 1.3: Cylindrical coordinate system

is assumed to be in a vacuum. For a circumference C on a plane orthogonal to z and passing through the point (r, z), the poloidal magnetic flux function Ψ can be defined as:

$$\Psi(r, z) = \int_S \boldsymbol{B_{pol}} \cdot \hat{n} dS \tag{1.32}$$

13

where S is any surface with boundary C ($\partial S = C$), and $\hat{n}$ is the unit normal vector consistent with z. Naturally, an equivalent expression for (1.32) is:

$$\Psi(r, z) = \oint_C \boldsymbol{A}_\phi \cdot \hat{dl} \tag{1.33}$$

where $\hat{dl}$ is the tangent vector to C. It is often useful to use the *poloidal flux per radian*:

$$\psi(r, z) = \frac{\Psi(r, z)}{2\pi} \tag{1.34}$$

The poloidal components of the induction can be easily derived from the flux (Figs. 1.4, 1.5), resulting in the following expressions:

$$B_r = -\frac{1}{r}\frac{\partial \psi}{\partial z} \tag{1.35}$$

$$B_z = \frac{1}{r}\frac{\partial \psi}{\partial r} \tag{1.36}$$
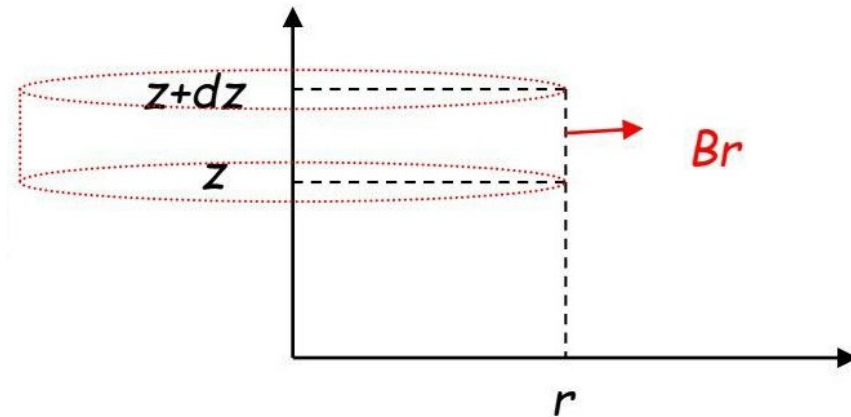
Figure 1.4: Calculation of B_r
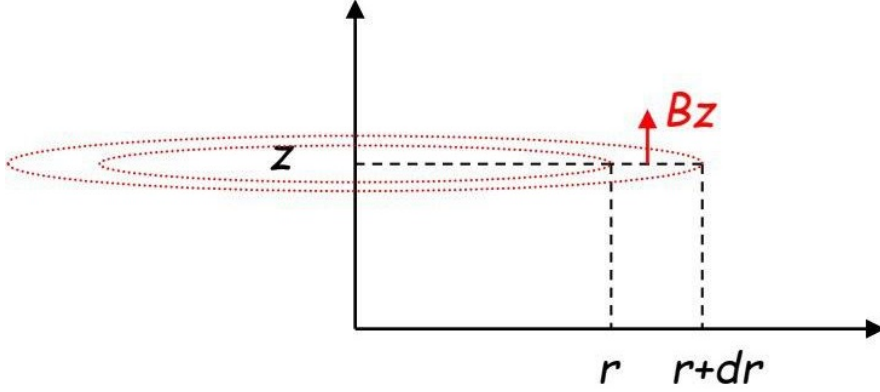
Figure 1.5: Calculation of B_z

Similarly, it can be defined the *poloidal current function per radian*:

$$F(r, z) = \frac{1}{2\pi} \int_S \boldsymbol{J_{pol}} \cdot \hat{n} dS \tag{1.37}$$

from which the two current components can be deduced:

$$J_r(r, z) = -\frac{1}{r} \frac{\partial (F/\mu_0)}{dz} \tag{1.38}$$

$$J_z(r, z) = \frac{1}{r} \frac{\partial (F/\mu_0)}{dr} \tag{1.39}$$

From the Ampère's circuital law, a relationship between poloidal current and toroidal component of the magnetic field is deduced:

$$F(r, z) = \frac{r}{\mu_0} B_\phi(r, z) \tag{1.40}$$

In conclusion, since the overall magnetic field, given by the superposition of the poloidal and toroidal components, is:

$$\boldsymbol{B} = B_r \hat{r} + B_z \hat{z} + B_\phi \hat{\phi} = \boldsymbol{B_{pol}} + B_\phi \hat{\phi} \tag{1.41}$$

taking into account (1.35) and (1.36), it can be written as:

$$\boldsymbol{B} = \frac{1}{r} \boldsymbol{\nabla} \psi(r, z) \times \hat{\phi} + \frac{F(r, z)}{r\mu_0} \hat{\phi} \tag{1.42}$$

The same reasoning can be applied to the total current density:

$$\boldsymbol{J} = \boldsymbol{J_{pol}} + J_\phi \hat{\phi} \tag{1.43}$$

From the Ampere's law, by explicitly taking the curl of the magnetic field, the following expression for J_ϕ can be obtained:

$$J_\phi = \hat{\phi} \cdot \boldsymbol{\nabla} \times \boldsymbol{B} = -\frac{1}{\mu_0 r}\Delta^*\psi \tag{1.44}$$

where $\Delta^*\psi$ is the *Grad-Shafranov operator*:

$$\Delta^*\psi = r\frac{\partial}{\partial r}\left(\frac{1}{r}\frac{\partial \psi}{\partial r}\right) + \frac{\partial}{\partial z}\left(\frac{\partial \psi}{\partial z}\right) \tag{1.45}$$

Thus, the total current density becomes:

$$\boldsymbol{J} = \frac{1}{r}\boldsymbol{\nabla}\left(\frac{F}{\mu_0}\right)\times\hat{\phi} - \frac{1}{\mu_0 r}\Delta^*\psi\hat{\psi} \tag{1.46}$$

To introduce the study of equilibrium, the following assumptions are made:

- ideal MHD model;

- steady-state conditions, i.e., $\frac{\partial}{\partial t} = 0$;

- static conditions, i.e., velocity $\boldsymbol{v} = 0$.

With these three assumptions, from (1.5), it is easy to derive again the (1.28), and therefore:

$$\boldsymbol{J}\cdot\boldsymbol{\nabla}p = 0 \tag{1.47}$$

$$\boldsymbol{B}\cdot\boldsymbol{\nabla}p = 0 \tag{1.48}$$

which can be rewritten as:

$$\boldsymbol{J}\cdot\boldsymbol{\nabla}p = \frac{1}{\mu_0 r}\hat{\phi}\cdot\boldsymbol{\nabla}\,p\times\boldsymbol{\nabla}\,F = 0 \tag{1.49}$$

$$\boldsymbol{B}\cdot\boldsymbol{\nabla}p = \frac{1}{r}\hat{\phi}\cdot\boldsymbol{\nabla}\,p\times\boldsymbol{\nabla}\,\psi = 0 \tag{1.50}$$

It is therefore deduced that:

$$\boldsymbol{\nabla}p\times\boldsymbol{\nabla}\,\psi = \boldsymbol{\nabla}p\times\boldsymbol{\nabla}\,F = 0 \qquad => \qquad \boldsymbol{\nabla}F\times\boldsymbol{\nabla}\,\psi = 0 \tag{1.51}$$

or equivalently, a coincidence between the isoflux, isobar, and iso-current lines, which means a condition of parallelism:

$$\boldsymbol{\nabla}\psi//\boldsymbol{\nabla}F//\boldsymbol{\nabla}p \tag{1.52}$$

It is possible to write a bijective mapping between the functions ψ, F, and p throughout the space occupied by the plasma:

$$p = p(\psi), \quad F = F(\psi) \tag{1.53}$$

Thus, (1.28) simplifies to:

$$\boldsymbol{J} \times \boldsymbol{B} = -\frac{\Delta^*\psi}{\mu_0 r^2}\boldsymbol{\nabla}\psi - \frac{F}{\mu_0 r^2}\boldsymbol{\nabla}F = \boldsymbol{\nabla}p \tag{1.54}$$

which leads to:

$$\Delta^*\psi\boldsymbol{\nabla}\psi = -F\boldsymbol{\nabla}F - \mu_0 r^2\boldsymbol{\nabla}p = -F\frac{dF}{d\psi}\boldsymbol{\nabla}\psi - \mu_0 r^2\frac{dp}{d\psi}\boldsymbol{\nabla}\psi \tag{1.55}$$

and then:

$$\Delta^*\psi = -F\frac{dF}{d\psi} - \mu_0 r^2\frac{dp}{d\psi} \tag{1.56}$$

which, considering (1.44), can be rewritten as the *Grad-Shafranov equation*:

$$J_\phi = \frac{1}{r}\frac{d(F^2/2\mu_0)}{d\psi} + r\frac{dp}{d\psi} \tag{1.57}$$

This equation relates the toroidal current density with the poloidal current function and the pressure, both functions of ψ at equilibrium. The (1.56) is a second-order nonlinear elliptic partial differential equation. Once the relations $p(\psi)$ and $F(\psi)$ are defined, the (1.57) becomes an equation with ψ as an unknown. It is generally solved with numerical techniques, given appropriate boundary conditions; such a solution allows obtaining an expression for the flux and, therefore, for $\boldsymbol{B}$ and $\boldsymbol{J}$ under equilibrium conditions within the framework of the MHD model. Many equilibrium codes are based on the solution of this equation; this aspect will be treated in a dedicated chapter.

The next step involves discussing stability. First, it is useful to highlight some conservation laws within the framework of the ideal MHD model. By recalling (1.5) and taking the dot product with the velocity $\boldsymbol{v}$ on both sides, the following power balance per unit volume is obtained:

$$\rho\,\boldsymbol{v}\cdot[\frac{\partial\boldsymbol{v}}{\partial t} + (\boldsymbol{v}\cdot\boldsymbol{\nabla})\boldsymbol{v}] = -(\boldsymbol{v}\cdot\boldsymbol{\nabla})p + \frac{1}{\mu_0}\,\boldsymbol{v}\cdot[(\boldsymbol{\nabla}\times\boldsymbol{B})\times\boldsymbol{B}] \tag{1.58}$$

From which, using the mass conservation law and vector identities, it is possible to write:

$$\frac{\partial}{\partial t}(\frac{1}{2}\rho v^2) + \boldsymbol{\nabla}\cdot(\frac{1}{2}\rho v^2\boldsymbol{v}) = -(\boldsymbol{v}\cdot\boldsymbol{\nabla})p + \frac{1}{\mu_0}\,\boldsymbol{v}\cdot[(\boldsymbol{\nabla}\times\boldsymbol{B})\times\boldsymbol{B}] \tag{1.59}$$

From the Poynting's law, considering that there is only magnetic energy and no dissipation:

$$\frac{\partial}{\partial t}(\frac{1}{2\mu_0}B^2) + \boldsymbol{\nabla}\cdot(\frac{\boldsymbol{E}\times\boldsymbol{B}}{\mu_0}) = 0 \tag{1.60}$$

By adding (1.59) and (1.60) to the adiabatic equation (1.8), it is possible to obtain the *ideal conservation energy law*:

$$\frac{\partial}{\partial t}(\frac{1}{2}\rho v^2 + \frac{1}{2\mu_0}B^2 + \frac{p}{\gamma-1}) + \boldsymbol{\nabla}\cdot(\frac{1}{2}\rho v^2\boldsymbol{v} + \frac{\boldsymbol{E}\times\boldsymbol{B}}{\mu_0} + \frac{\gamma}{\gamma-1}p\boldsymbol{v}) = 0 \tag{1.61}$$

The above equation represents an energy conservation law for the ideal MHD model. Integrating it within a volume V bounded by infinity or within a power-impermeable surface, it can be demonstrated that:

$$K + W = constant \tag{1.62}$$

where:

$$K = \int_V \frac{1}{2}\rho v^2 dV, \qquad W = \int_V (\frac{1}{2\mu_0}B^2 + \frac{p}{\gamma-1})dV \tag{1.63}$$

The terms K and W represent respectively kinetic energy and potential energy. The (1.62) states that the sum of these two energies is conserved within a volume V. This result will be useful for studying equilibrium stability.

The equilibrium can be stable or unstable depending on whether the system returns to or moves away from the equilibrium position due to a perturbation. To describe stability conditions, the assumption of small displacement is made, allowing a first-order analysis.

For this purpose, all variables are described as the sum of the equilibrium contribution (indicated with subscript 0) and the perturbation contribution (with subscript 1). For example, for the magnetic field $\boldsymbol{B}$:

$$\boldsymbol{B} = \boldsymbol{B_0} + \boldsymbol{B_1}, \qquad \text{where} \quad B_1 << B_0 \tag{1.64}$$

The MHD model (from 1.4 to 1.9), written for differences respect to the equilibrium, leads to the following *linearized MHD model*:

$$\frac{\partial\boldsymbol{B_1}}{\partial t} = \boldsymbol{\nabla}\times(\boldsymbol{v_1}\times\boldsymbol{B_0}) \tag{1.65}$$

$$\rho\frac{\partial\boldsymbol{v_1}}{\partial t} = -\boldsymbol{\nabla}p_1 + \frac{1}{\mu_0}(\boldsymbol{\nabla}\times\boldsymbol{B_0})\times\boldsymbol{B_1} + \frac{1}{\mu_0}(\boldsymbol{\nabla}\times\boldsymbol{B_1})\times\boldsymbol{B_0} \tag{1.66}$$

$$\frac{\partial\rho_1}{\partial t} = -\boldsymbol{v_1}\cdot\boldsymbol{\nabla}\rho_0 - \rho_0\boldsymbol{\nabla}\cdot\boldsymbol{v_1} \tag{1.67}$$

$$\frac{\partial p_1}{\partial t} = -\boldsymbol{v_1} \cdot \boldsymbol{\nabla} p_0 - \gamma p_0 \boldsymbol{\nabla} \cdot \boldsymbol{v_1} \qquad (1.68)$$

This set of equations describes the dynamics of the plasma around the equilibrium position. Perturbations of the fluid modeled by the ideal MHD model can be expressed in terms of the displacement vector $\boldsymbol{\xi}(\boldsymbol{r_0}, t)$, such that:

$$\boldsymbol{r} = \boldsymbol{r_0} + \boldsymbol{\xi} \quad \rightarrow \quad \boldsymbol{v} = \frac{d\boldsymbol{r}}{dt} = \frac{d\boldsymbol{r_0}}{dt} + \frac{\partial \boldsymbol{\xi}}{\partial t} + (\boldsymbol{v_1} \cdot \boldsymbol{\nabla})\boldsymbol{\xi} \qquad (1.69)$$

where $\boldsymbol{r}$ is the position vector and $\boldsymbol{v}$ is the velocity vector. Remembering that $\boldsymbol{v_0} = 0$ and neglecting second-order terms, it follows:

$$\boldsymbol{v} = \boldsymbol{v_1} = \frac{\partial \boldsymbol{\xi}}{\partial t} \qquad (1.70)$$

By substituting this expression into (1.67), the following expression for the mass density is obtained:

$$\rho_1 = -\boldsymbol{\xi} \cdot \boldsymbol{\nabla} \rho_0 - \rho_0 \boldsymbol{\nabla} \cdot \boldsymbol{\xi} \qquad (1.71)$$

which means that the variation in mass density depends on a term related to the position variation ($\boldsymbol{\xi}$) and a term of compression ($\boldsymbol{\nabla} \cdot \boldsymbol{\xi}$). Performing the same procedure on (1.65) and (1.68):

$$\boldsymbol{B_1} = \boldsymbol{\nabla} \times (\boldsymbol{\xi} \times \boldsymbol{B_0}) \qquad (1.72)$$

$$p_1 = -\boldsymbol{\xi} \cdot \boldsymbol{\nabla} p_0 - \gamma p_0 \boldsymbol{\nabla} \cdot \boldsymbol{\xi} \qquad (1.73)$$

Substituting these three equations into (1.66), the following is obtained:

$$\rho_0 \frac{\partial^2 \boldsymbol{\xi}}{\partial t^2} = \boldsymbol{\nabla}(\boldsymbol{\xi} \cdot \boldsymbol{\nabla} p_0 + \gamma p_0 \boldsymbol{\nabla} \cdot \boldsymbol{\xi}) + \frac{1}{\mu_0}[(\boldsymbol{\nabla} \times \boldsymbol{B_0}) \times (\boldsymbol{\nabla} \times (\boldsymbol{\xi} \times \boldsymbol{B_0})) +$$
$$+ \boldsymbol{\nabla} \times (\boldsymbol{\nabla} \times (\boldsymbol{\xi} \times \boldsymbol{B_0})) \times \boldsymbol{B_0}] \qquad (1.74)$$

The RHS can be written as $\boldsymbol{F}(\boldsymbol{\xi})$ since it is a function of p_0, ρ_0, $\boldsymbol{B_0}$ (known) and $\boldsymbol{\xi}$:

$$\rho_0 \frac{\partial^2 \boldsymbol{\xi}}{\partial t^2} = \boldsymbol{F}(\boldsymbol{\xi}) \qquad (1.75)$$

The equation (1.75) provides the evolution of the displacement following a perturbation for a given equilibrium. It can be extended to include other components such as gravity, resistivity, and other phenomena that are neglected here.

There are various methods for stability analysis. Two methods will be illustrated here: the *method of normal modes* and the *energy method*.

The first method represents the perturbation in the form:

$$\boldsymbol{\xi} = \hat{\boldsymbol{\xi}}(\boldsymbol{r})e^{j\omega t} \tag{1.76}$$

For this class of displacements, equation (1.75) becomes:

$$-\rho_0\omega^2\hat{\boldsymbol{\xi}} = \boldsymbol{F}(\hat{\boldsymbol{\xi}}) \tag{1.77}$$

where ω^2 must be real, as $\boldsymbol{F}(\hat{\boldsymbol{\xi}})$ is real. If $\omega^2 > 0$, the two real roots imply that $\boldsymbol{\xi}$ in (1.76) remains bounded (stable system). Conversely, if $\omega^2 < 0$, $\boldsymbol{\xi}$ diverge (unstable system).

To implement the second method, the energy method, the (1.75) is multiplied with $\boldsymbol{\xi}$ and integrated over a volume V. This yields to the following expression:

$$\frac{d}{dt}\left[\int_V \frac{1}{2}\rho_0\left|\frac{\partial\boldsymbol{\xi}}{\partial t}\right|^2 dV\right] = \frac{d}{dt}\left[\int_V \frac{1}{2}\boldsymbol{\xi}\cdot\boldsymbol{F}(\boldsymbol{\xi})dV\right] \tag{1.78}$$

The two terms in (1.78) represent variations in kinetic and potential energy (as $\boldsymbol{F}(\boldsymbol{\xi})$ is a conservative force) caused solely by the perturbation. Thus, it can be written:

$$\delta K + \delta W = constant \tag{1.79}$$

The equation (1.79) represents an energy conservation equation. Consequently, a necessary and sufficient condition for stability is:

$$\delta W \geq 0 \tag{1.80}$$

for every possible perturbation, that is, for every $\boldsymbol{\xi}$. If there exists at least one displacement value for which $\delta W \leq 0$, then the system is unstable.

What are the consequences of these instabilities? Considering the case of a plasma in an indefinite cylindrical structure, as discussed earlier, the Z-pinch condition presents two types of instabilities (Fig. 1.6):

- Kink: it is a helical instability. Considering a point with curvature, there are lower curvatures, which are tighter with a stronger magnetic field, and upper curvatures with weaker fields. Consequently, the force due to the magnetic field in the lower curvature (directed upward) cannot be balanced by the same force due to the field in the upper curvature (directed downward). Overall, there is a net upward force, and the perturbation diverges.

- Sausage: it is an instability caused by constrictions that occur along the cylindrical plasma. In the points where the structure narrows, the interaction between the magnetic field and the current is higher compared to points with no constriction. This interaction tends to increase the magnitude of the perturbation, causing it to diverge.
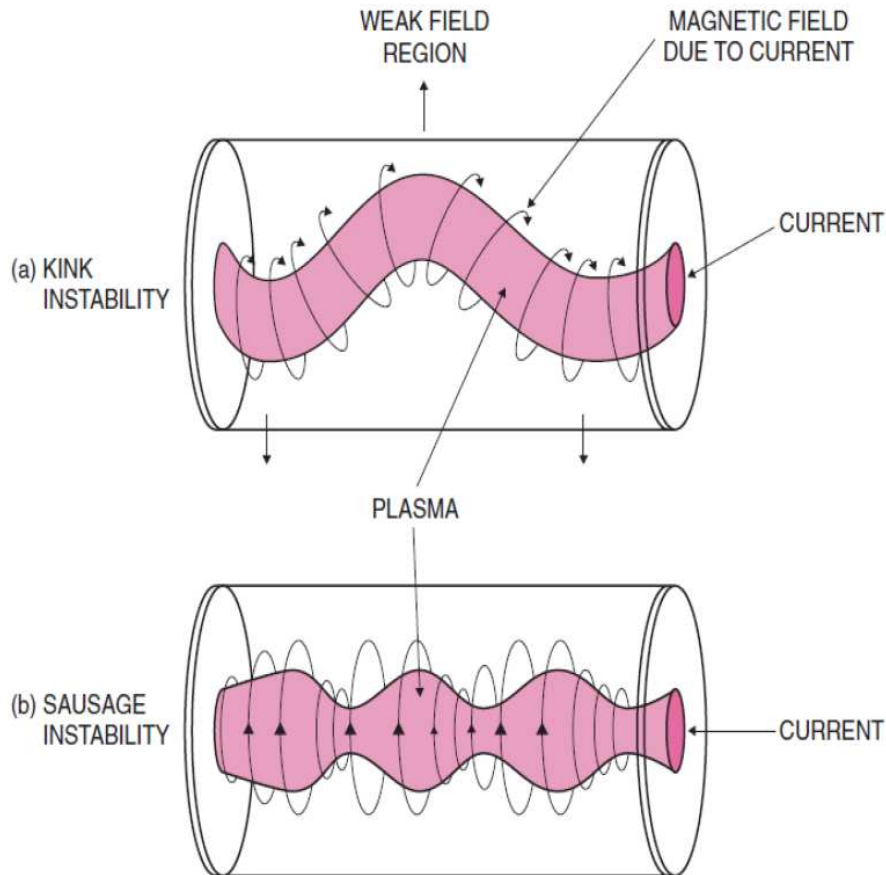
Figure 1.6: Kink and sausage instabilities

Kink and sausage instabilities can be "stabilized" by adding an axial field. This field causes a magnetic flux through the cylinder section, so when a perturbation arises, the flux must remain constant (as seen previously in the ideal MHD model). The axial field creates a force that stabilizes the plasma. Specifically, in the kink case, the field lines bend due to curvature, generating a magnetic tension that opposes the instability. In the sausage case, a magnetic pressure is generated at the constriction points, preventing further narrowing and tending to stabilize it.

1.3 MCF machines

Now, a brief description of the main machines that use magnetic confinement techniques will be provided. Some of these machines have already been men-

tioned earlier in reference to the evolution of scientific research in controlled nuclear fusion. Below, the RFP and Stellarator configurations will be briefly introduced, while Tokamaks will be described in the subsequent chapter.

- RFP: it is a toroidal device with axial symmetry (Fig. 1.7). The main difference between RFP and Tokamak lies in the field configuration: in RFP machines, the toroidal magnetic field has nearly the same intensity of the poloidal field, while in Tokamaks the toroidal field is usually much stronger. Additionally, in RFP machines, the field in the outer region of the plasma is reversed compared to the inner region. The largest machine of this type currently in operation is the Modified Reversed Field eXperiment (RFX-Mod) at the research facilities of the National Research Council (CNR) in Padua, Italy, an upgraded version of the previous RFX [7]. RFX is particularly focused on plasma turbulence studies to provide useful data for the development of ITER (International Thermonuclear Experimental Reactor) and DEMO (DEMOnstration Power Plant), two important future devices.
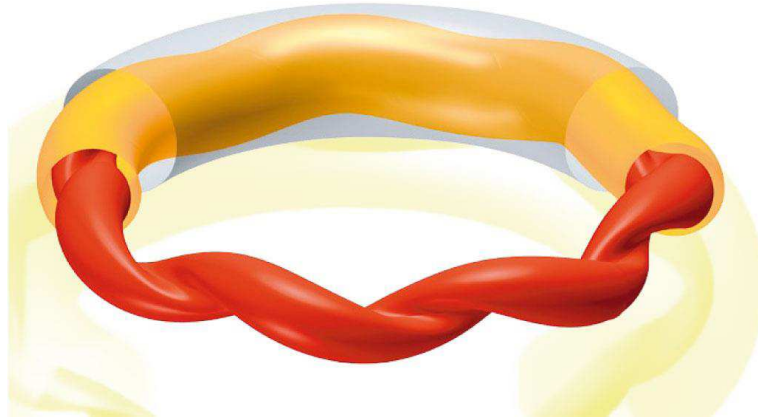
Figure 1.7: Representation of the plasma in the RFP-Mod configuration

- Stellarator: it is a device with a complex 3D geometry (Fig. 1.8), suitable for studying specific equilibrium conditions. The largest stellarator currently operational is the Wendelstein 7-X (W7-X), located in Greifswald, Germany. Despite its complex and expensive design, the stellarator can make a significant contribution to the scientific community in the field of fusion research.
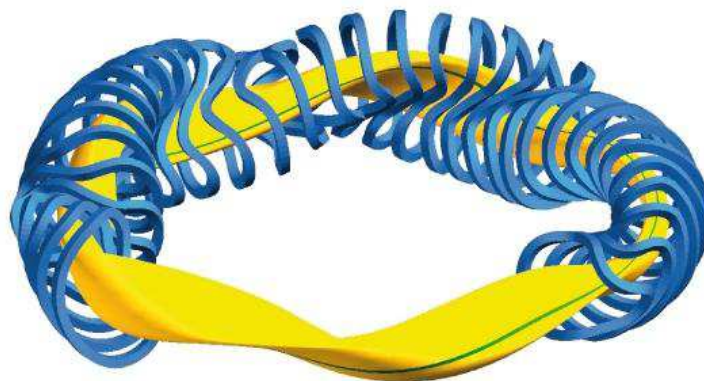
Figure 1.8: Representation of the plasma in the stellarator configuration, surrounded by coils arranged in a complex 3D geometry

Bibliography

[1] Wesson, J., & Campbell, D. J. (2011). Tokamaks (Vol. 149). Oxford university press.

[2] Nakai, S., & Takabe, H. (1996). Principles of inertial confinement fusion-physics of implosion and the concept of inertial fusion energy. Reports on progress in physics, 59(9), 1071.

[3] Zylstra, A. B., Kritcher, A. L., Hurricane, O. A., Callahan, D. A., Ralph, J. E., Casey, D. T., ... & Young, C. V. (2022). Experimental achievement and signatures of ignition at the National Ignition Facility. Physical Review E, 106(2), 025202.

[4] I, Wikigian [CC BY-SA 3.0 (http://creativecommons.org/licenses/by-sa/3.0/)]

[5] Chen, F. F. (1984). Introduction to plasma physics and controlled fusion (Vol. 1, pp. 19-51). New York: Plenum press.

[6] Fitzpatrick, R. (2022). Plasma physics: an introduction. Crc Press.

[7] Pizzo, F., Computational Electromagnetism and Optimization Problems in HPC environment Application to Thermonuclear Fusion Devices, Ph.D. Thesis, Seconda Università degli Studi di Napoli

BIBLIOGRAPHY

2
Tokamaks

THIS chapter serves as a comprehensive introduction to Tokamak devices, providing an overview of their historical development, fundamental principles and key components. A description of the COMPASS Tokamak, of great importance in this activity, will be given, with an overview of the most interesting upcoming devices.

2.1 Historical evolution of Tokamak devices

Among the various fusion reactor concepts, the Tokamak stands out as the most promising and extensively researched configuration for achieving controlled nuclear fusion. The Tokamak, derived from the Russian acronym for "toroidal chamber with magnetic coils", represents a crucial milestone in the pursuit of sustainable, safe, and large-scale energy generation.

The concept of confining plasma using magnetic fields was first proposed in the 1950s by the Soviet physicists Andrej Sakharov and Igor' Tamm [1]. In the same period, in the USA, similar studies were conduced on the Stellarator configuration. These research remained firstly secret in both countries, but in a series of conferences in Geneva in 1955 and 1958, the existence and working principles of the Tokamaks were disclosed. The first experimental device was developed in 1958 at the Kurchatov Institute in Moscow, followed by a series of experiments and devices in the 1960s and early 1970s, dedicated to the study of the plasma thermal confinement. Since then, significant progresses have been made. Important milestones are the construction of the JET (Joint European Torus) [2] device in the UK, ASDEX (Axially Symmetric Divertor

EXperiment) in Germany, DIII-D in the USA and JT-60 (Japan Torus-60) in Japan, among many others. Important research will be carried out on some future devices, such as ITER, in construction in France, and SPARC (Smallest/Soonest Possible ARC) [3], in design phase at the Commonwealth Fusion System.

2.2 Main components

A Tokamak device consists of several essential components, each playing a crucial role in achieving controlled fusion. Here, only part of the components will be described. A particular focus will be given on the following:

- the magnetic system;

- passive structures, such as the vessel;

- diagnostics.

Each one of this component will be treated in a dedicated subsection.

2.2.1 The magnetic system

The magnetic system is the set of all the components dedicated to the creation of the magnetic field, necessary for the correct operation of the device. It can be split in several subsystems, each one with a specific role.

The primary component of the magnetic field is the toroidal component B_ϕ. It is produced by the current circulating in dedicated poloidal windings that surround the toroidal chamber (Fig. 2.1), the Toroidal Field (TF) coils system. In current machines, these windings are realized using superconductors and have a D-shaped form, in order to reduce the mechanical efforts of the structure. As mentioned earlier, B_ϕ serves the purpose of stabilization and partially confinement. It's worth noting that due to the toroidal nature, as described in [4], the following relationship stands:

$$2\pi R B_\phi = \mu_0 I_T \qquad \Rightarrow \qquad B_\phi \propto \frac{1}{R} \qquad (2.1)$$

where I_T is the total current that flows into the conductors.

Additionally, from the particle perspective, the field gradient leads to a particle drift, which can be corrected using a poloidal field B_θ. One of the primary sources of poloidal field is the current I_p flowing within the plasma itself. This current is induced resorting to a transformer effect, where an
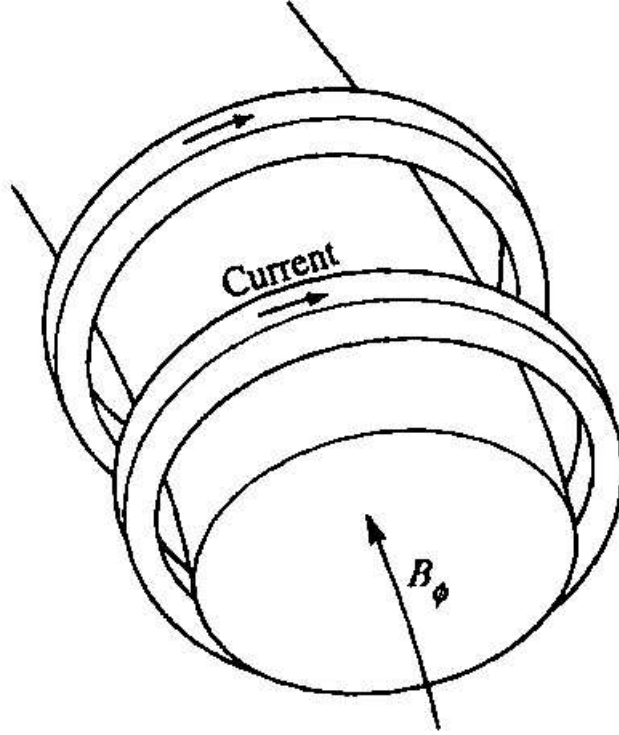
Figure 2.1: Poloidal windings

external winding acts as the primary (the Central Solenoid, CS) and the plasma as the secondary. In some cases (e.g., the JET device), a ferromagnetic core is also employed (Fig. 2.2). Considering the *virial theorem*, it becomes clear that external currents are required for plasma equilibrium. Due to the currents flowing into it, that interact with the fields produced by external sources and by itself, the plasma is subject to a centrifugal force. To balance it, a vertical field B_V, known as the *equilibrium field*, is applied to create a centripetal force (Fig. 2.3).

Two important parameters defining the plasma shape are the *elongation*, which is b/a in Fig. 2.3, and the *triangularity*, indicating the internal shift of the upper point of the ellipse, and calculated as the ratio between the radius of the upper point and a. To improve machine performance, an elongated plasma shape is preferred, requiring an additional force distribution with zero net result:

$$\Delta F_U + \Delta F_L = 0 \tag{2.2}$$

The forces ΔF_U and ΔF_L can be achieved using a *quadrupolar field dis-*

29
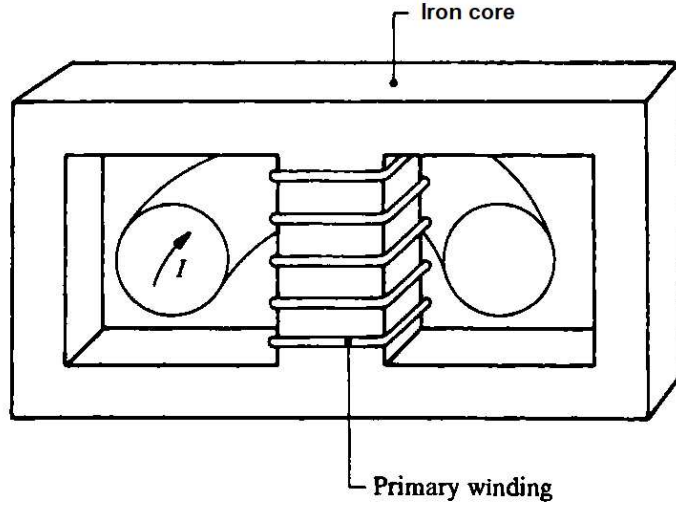
Figure 2.2: Primary winding with a ferromagnetic core
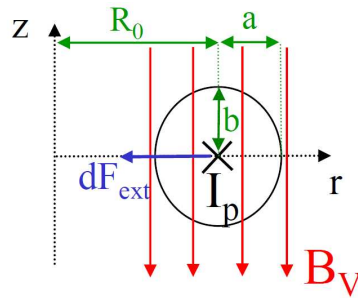
Figure 2.3: Vertical field generating a radial force inward; *a* and *b* are the half-sizes of the plasma

tribution. However, its combination with the vertical equilibrium field alters the overall curvature, making the plasma unstable for vertical displacements (Fig. 2.4).

A parameter that assesses the degree of vertical instability is the *field index n*, defined as:

$$n = -\frac{R_0}{B_V}\frac{\partial B_r}{\partial z} \tag{2.3}$$

If $n > 0$, the equilibrium is unstable.

In general, the external currents are provided by a Poloidal Field (PF) coils system.

The assumption of axisymmetry is only approximately satisfied. An important 3D component of the field results from the toroidal field ripple,
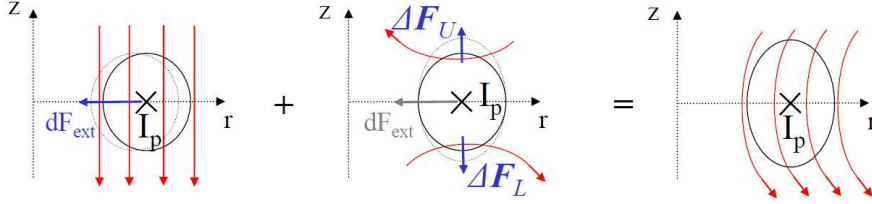
Figure 2.4: Instability due to the combination of vertical and quadrupole fields

mainly due to discrete toroidal field windings. Two methods counteract the ripple effect: one uses ferromagnetic inserts to align the field (passive correction), and the other employs correction coils (active correction).

The performance of a Tokamak relies on the strength of the available magnetic fields. Therefore, copper windings are excluded due to their significant Joule heating limits [4]. Instead, superconductors are utilized to achieve higher magnetic field strengths. Copper windings are used only for specific applications, they are located inside the vessel and require limited currents.

2.2.2 The vacuum vessel

The vacuum vessel (Fig. 2.5) is the primary boundary between the plasma and the surrounding environment. It provides a high-vacuum environment and improves radiation shielding and plasma stability. Furthermore, it is a mechanical support for a big set of in-vessel components, such as the in-vessel coils system, the blanket, and the divertor.

Usually, the vessel is covered with a series of openings, or ports, to give access to remote handling, diagnostics, heating and vacuum systems. All these openings break the axial-symmetry in the vessel structure, and this leads to the rise of 3D behaviour in the plasma and the magnetic field. This aspect is important for the focus of this thesis, in particular about the study of the impact of these openings during the disruptions.

One of the most important components of the vacuum vessel is the blanket, which serves three fundamental purposes:

- Absorption of neutrons resulting from the fusion reaction and conversion into thermal energy. This energy is then transferred to an appropriate liquid or gaseous coolant, which is subsequently transformed into electrical energy using conventional techniques, such as turbine-driven generators (Fig. 2.6).
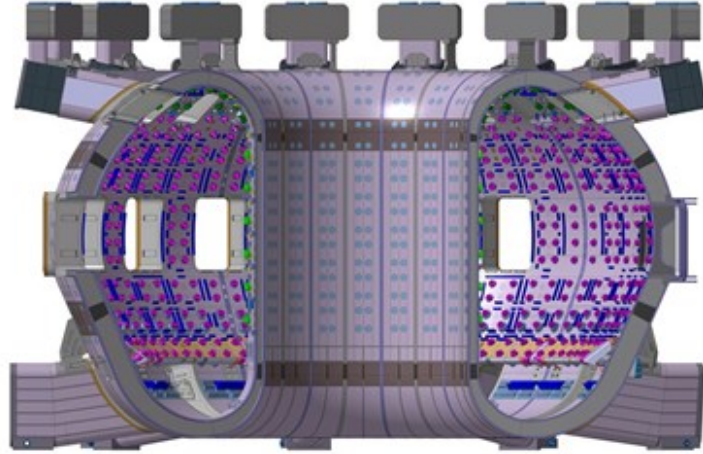
Figure 2.5: Representation of a Tokamak vacuum vessel (ITER)
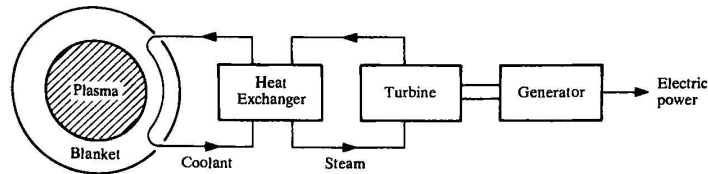
Figure 2.6: Conversion of nuclear energy into electrical energy

- Moderation of neutron velocities to limit damage to components, such as superconducting windings and walls.

- In the case of a *breeding* blanket, tritium production necessary for the reaction can be achieved. To accomplish this, the blanket is filled with lithium compounds (e.g., LiO_2), exploiting the lithium-neutron reaction mentioned earlier.

To improve neutron shielding, an additional *shield* is often added (Fig. 2.7).

2.2.3 Magnetic diagnostics

Fusion machines are equipped with a complex diagnostic system based on various technologies aimed at monitoring the plasma and different components of the reactor. The diagnostics system is capable of monitoring the following physical subjects:
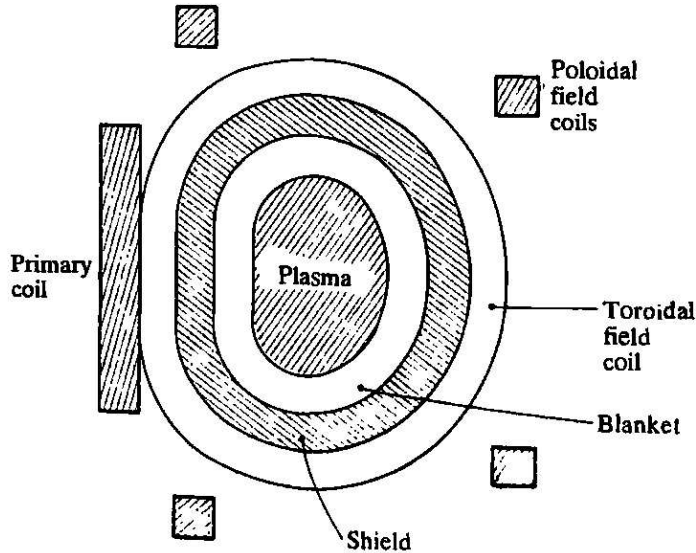
Figure 2.7: Arrangement of coils, blanket, and shield in a Tokamak

- plasma stability;

- particle containment and transport coefficients;

- plasma heating;

- plasma impurities;

and many others. This thesis will focus solely on magnetic diagnostics, specifically electromagnetic measurements. Two types of magnetic sensors are here described:

- saddle coils: windings that surround the plasma and part of the structure (Fig. 2.8(a)). They are used to measure the magnetic flux by integrating the induced voltage, and then they are capable to give the average component of the field normal to the coil surface;

- pick-up coils, or Rogowski coils: probes designed for measuring the magnetic field (Fig. 2.8(b)) tangential to the axis of the probe itself.

Unfortunately, there are no direct measurements to evaluate the electrical and magnetic characteristics of the plasma from the current profile. In principle, one could solve the MHD equilibrium model to determine these parameters. However, numerically solving this problem can be time-consuming, even

33
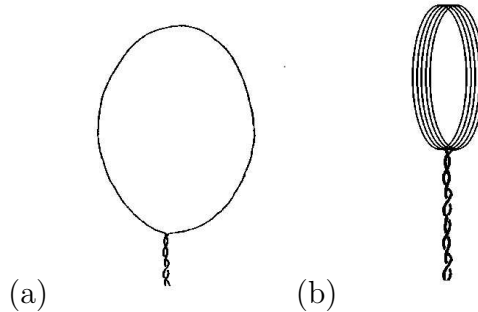
Figure 2.8: (a) Saddle coils; (b) pick-up coils

with modern computers, making it impractical for real-time control analysis, especially concerning plasma instabilities.

2.3 Configurations and scenarios

In the design and operation of a Tokamak, it is crucial to define the equilibrium conditions of the plasma, which are characterized, among other factors, by its boundary. The most commonly used definition for the plasma boundary is the *Last Closed Magnetic Surface* (LCMS), which is the largest closed surface that does not intersect the innermost wall of the chamber, known as the *first wall*. Two main configurations are considered:

- *limiter configuration*: the plasma has an oval section and touches the vessel at a single point known as the *limiter point* (Fig. 2.9(a));

- *diverted configuration*: the plasma has a "drop" shape, does not touch the walls, and the boundary is characterized by a point with zero poloidal magnetic field, known as the *X-point* (Fig. 2.9(b)).

In addition to these configurations, there are more complex ones, some of which are variations of the diverted configuration, such as double null configurations, reverse triangularity, and others. Determining the plasma boundary involves both the currents from external coils and the plasma's own current, leading to a challenging problem known as the *free boundary problem*.

The shape of the plasma changes during the discharge. An example of a *scenario* is illustrated in Fig. 2.10, where, in particular, the behavior of the plasma current is shown. Typically, a scenario consists of three main phases:

- *ramp-up*: in this phase, the central solenoid is activated, and the plasma current increases. Usually, the plasma "birth" occurs in a limiter-like
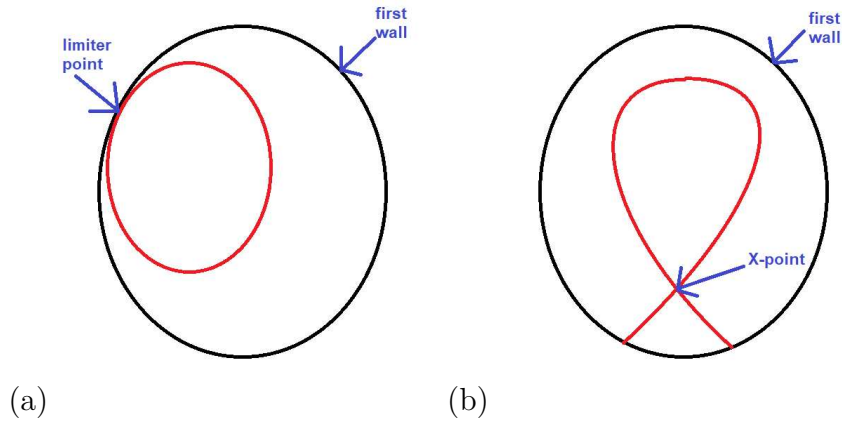
Figure 2.9: (a) Limiter configuration; (b) diverted configuration
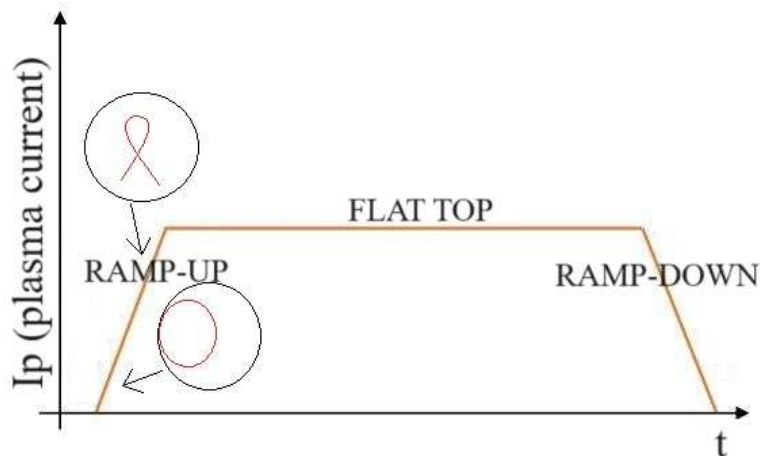
Figure 2.10: Example of a scenario

configuration and then evolves into a more complex diverted configuration (as shown in Fig. 2.10, where the formation of the X-point is indicated);

- *flat-top*: this phase involves maintaining the plasma current as constant as possible;

- *ramp-down*: this phase is the opposite of the ramp-up phase, the plasma current decreases, and the shape returns to a limiter-like configuration.

Based on equilibrium and stability requirements, as well as the desired scenario, it becomes apparent that the various windings responsible for providing the poloidal component of the magnetic field operate on different time

scales. The central solenoid must have dynamics that allow for rapid changes in the plasma current during the ramp-up phase. In the flat-top phase, the current must be kept constant, necessitating a limited electromotive force to minimize the plasma's ohmic losses. The equilibrium fields must operate on the same time scales as the plasma current to follow its variations promptly, and the field of the control system needs to act on time scales related to instabilities, typically on the order of tenths or units of milliseconds. Balancing these factors is essential for achieving stable and controlled plasma confinement in a Tokamak device.

2.4 Disruptions

Disruptions phenomena are a main concern in Tokamaks [5, 6]. A disruption is an event that terminates suddenly a plasma discharge, usually as a consequence of an instability, leading to a loss of particle containment. The events that lead to a disruption are, usually, first an initiating event, followed by a thermal quench and then a current quench.

There are many possible initiating events, that lead to different kind of quenches. The causes can be divided into two categories: external and internal.

- The external causes include mechanical faults, or wrong instructions and failures of the magnetic control system. The latter ones can be accidental or provoked by purpose, in order to study the disruptions.

- The internal causes include plasma events like Edge-Localized Modes (ELMs), H-L transitions, instabilities like kink or ballooning modes, or magnetic islands interactions.

The thermal quench is a pulsed release of heat energy on the plasma facing surface [7]. This leads to a temperature loss in the plasma, and may result in melting or vaporization of the wall.

The current quench is a sudden termination of the plasma current [8]. As a consequence, the plasma energy is transferred to the surrounding structures, such as vessel, coils, and supporting structures, causing the rise of eddy currents. These currents, interacting with the magnetic field, lead to magnetic forces and a mechanical damage.

Usually, following a current quench, there is a Vertical Displacement Event (VDE), i.e. a vertical displacement of the plasma position. This is also an event that causes the rise of magnetic forces.

The disruptions have always aroused interest in Tokamak research, and it is estimated that they will be even more destructive in future machines, like ITER and DEMO. The concern around these phenomena is one of the reasons why the activity shown in this thesis was performed.

2.5 The COMPASS device

The COMPASS (COMpact ASSembly) device is a compact experimental Tokamak, originally located in the Culham Centre for Fusion Energy (UK), and moved to the Institute of Plasma Physics of the Academy of Sciences of the Czech Republic, in Prague, in 2006 [9]. COMPASS was designed to study the physics of the plasma edge and the Scrape-Off Layer (SOL), and to provide data for a ITER-like plasma shape, in order to help on the scaling toward the ITER device.

The major and minor radii are $R = 0.56$ m and $a = 0.2$ m, with a maximum plasma current of 400 kA, a toroidal magnetic field between 0.8 T and 2.1 T, and an elongation of 1.8. The device can generate plasma with different gases [10] and different configurations, like circular, elongated and single null X-point.

COMPASS is equipped with an extensive diagnostics system (Fig. 2.11) [11]. Considering only the magnetic diagnostics, there are a set of Mirnov coils, Internal and External Partial Rogowski coils (IPR and EPR, respectively) capable to measure the local tangential field, internal and external Rogowski to measure plasma current, vessel current and the sum of both, a set of 104 saddle loops (76 working) to measure the normal field on the external side of the vessel, and many others. The most important diagnostics for this activity are the saddle loops and, on a minor extent, the EPR. More details about these two component will be given in the following.

The vacuum vessel has a divertor covered with carbon tiles, capable to handle the presence of two Neutral Beam Injectors (NBI), and several openings, necessary for diagnostics and remote handling.

In Fig. 2.12, a sketch of part of the magnetic system of COMPASS is reported.
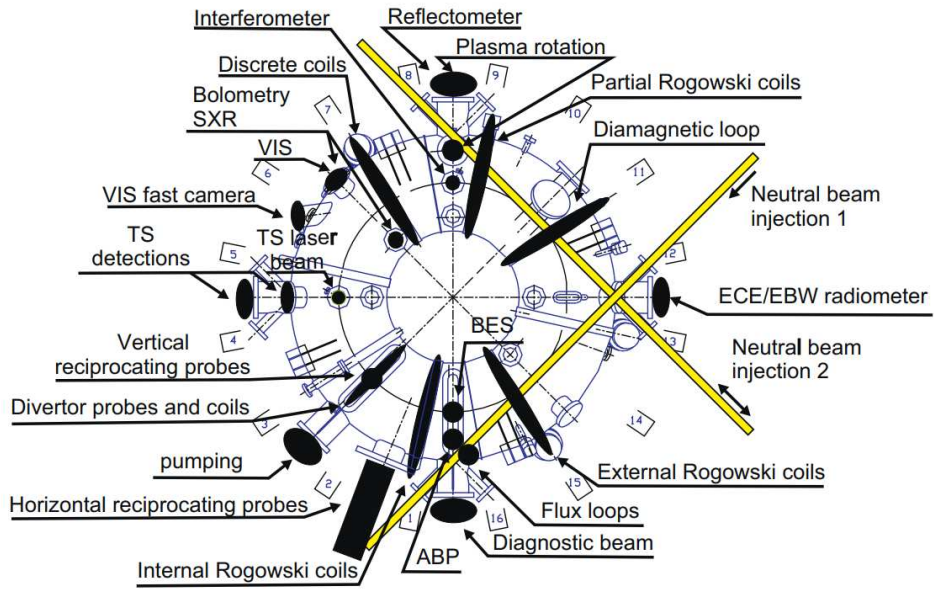
Figure 2.11: Overview of the COMPASS diagnostic systems [11]
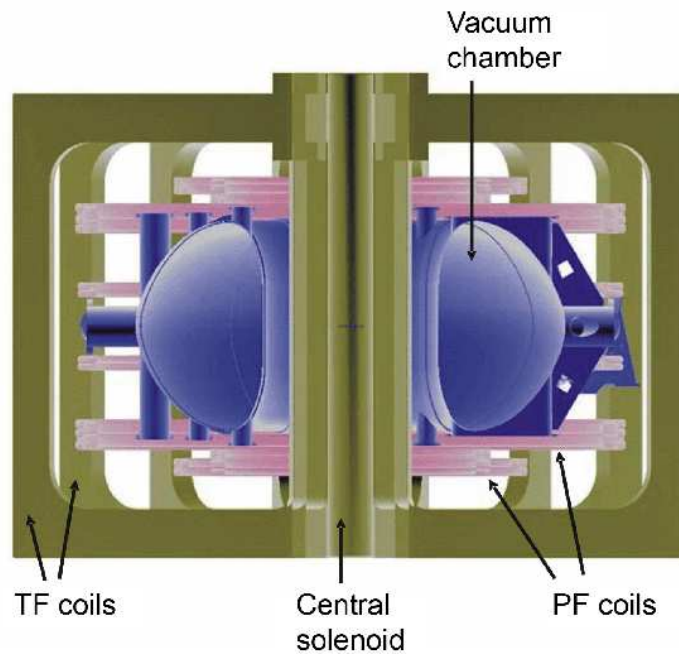
Figure 2.12: Sketch of some components of the magnetic system of the COM-PASS device, along with the vacuum chamber [12]

2.6   Future devices

This section provides an overview of the main features of the most important Tokamaks currently under construction or in the design phase: ITER and DTT. Fusion research requires substantial technical, economic, and human resources.

2.6.1   ITER

ITER is the leading international fusion project, involving contributions from numerous countries worldwide, with significant involvement of the European Union. Its overall structure is 24 m high, 30 m wide, with a total weight of 23,000 tons, a plasma volume of 840 m^3, and a major radius of 6.2 m. Its main objective is to achieve a confinement time of 400-500 seconds and develop a power output of 500 MW with a discharge multiplication factor (Q) of 10.

The magnetic system of ITER is described below:

- The toroidal field system consists of 18 D-shaped superconducting coils. The achievable toroidal field reaches a maximum of 11.8 T at coil and 5.3 T on the axis, with a stored energy of 41 GJ. Each coil weighs 310 tons, measuring 17 m in height and 9 m in width, resulting in a total weight of over 3,400 tons.

- The poloidal field system is comprised of 6 circular-shaped superconducting coils. The larger coils have a diameter of 24 m and weigh up to 400 tons. The achievable poloidal field strength is about 6 T, with a stored energy of about 4 GJ.

- The central solenoid consists of 6 coils with a total height of 18 meters and a weight of approximately 1000 tons. It is capable of sustaining a plasma current of 15 MA for 300-500 seconds. The system can withstand electromagnetic forces up to 60 MN.

- There are also 18 additional superconducting correction coils to compensate for any field errors resulting from construction imperfections in the various windings. These coils carry currents in the order of 10 kA and measure approximately 10 m in size.

- Additional coils within the vessel provide fine control of the field, such as the divertor region windings, essential for X-point management.

In Fig. 2.13, a sketch of part of the magnetic system of ITER is reported.

2.6.2 DTT

DTT (Divertor Tokamak Test) (Fig. 2.14) is one of the main investments in fusion research, mostly funded by Italy. In this device, the plasma has a major radius of 2.15 m, a minor radius of 0.65 m, and an elongation of 1.6-1.8 [13]. The toroidal magnetic field reaches 6 T on the axis, and the discharge duration is in the order of 100 seconds. Similar to ITER, DTT will be equipped with a complex system of windings for generating the toroidal and poloidal fields, inducing current in the plasma, and creating complex plasma configurations. A significant additional plasma heating system, providing about 45 MW of additional heating power, will be included. DTT is specifically designed to investigate the treatment of the plasma surface layer and divertor technologies for DEMO. It will create operating conditions comparable to those expected in DEMO for these specific aspects. Therefore, the design of DTT has been developed as a "scaled" version of larger machines, allowing for the evaluation of different technologies and techniques for achieving the divertor configuration. Its construction has just begun, and it is expected to operate for over twenty years after approximately seven years of construction.

a)

b)
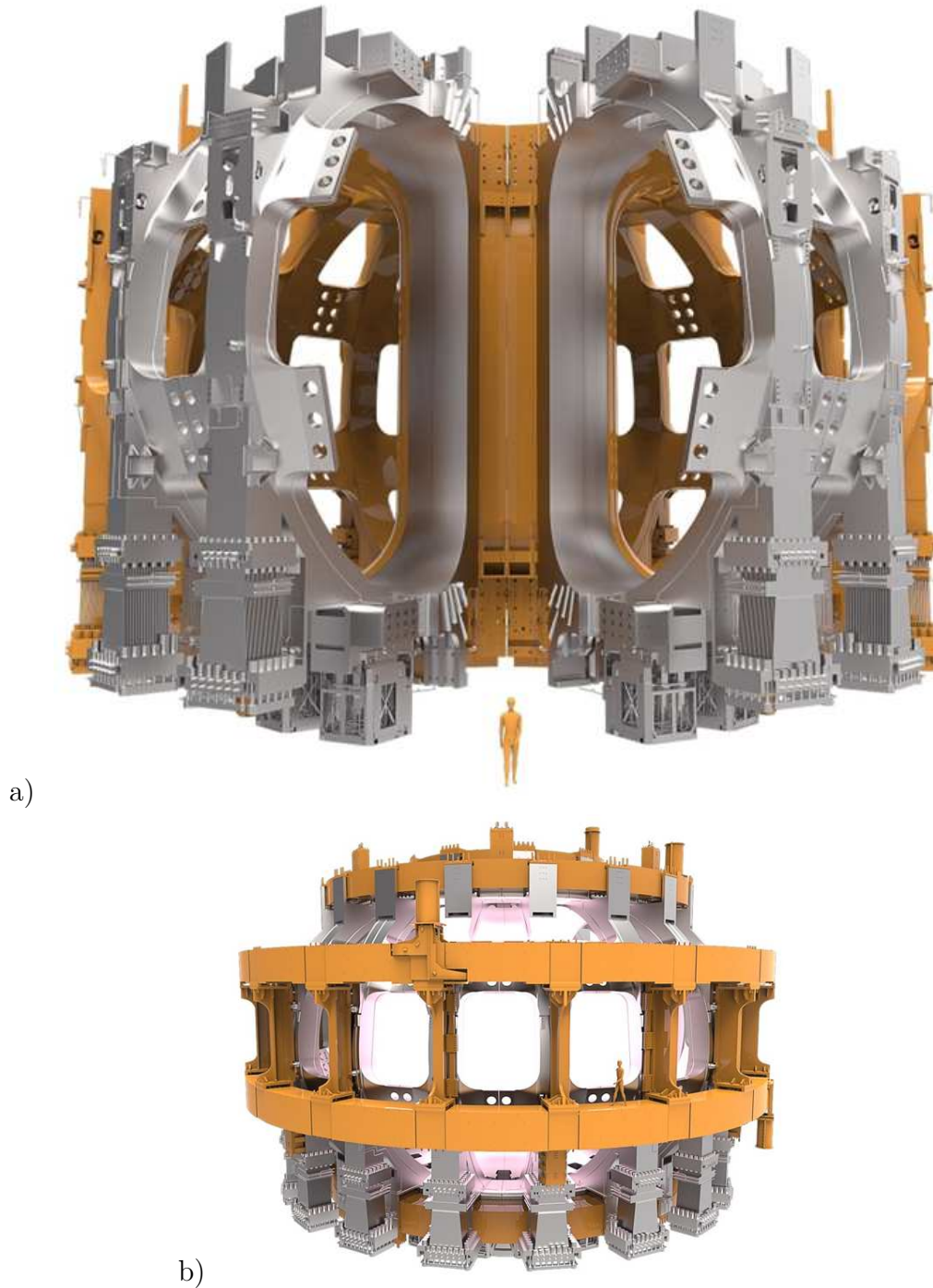
Figure 2.13: Sketch of some components of the magnetic system of ITER: a) TF and b) PF coils systems [14]
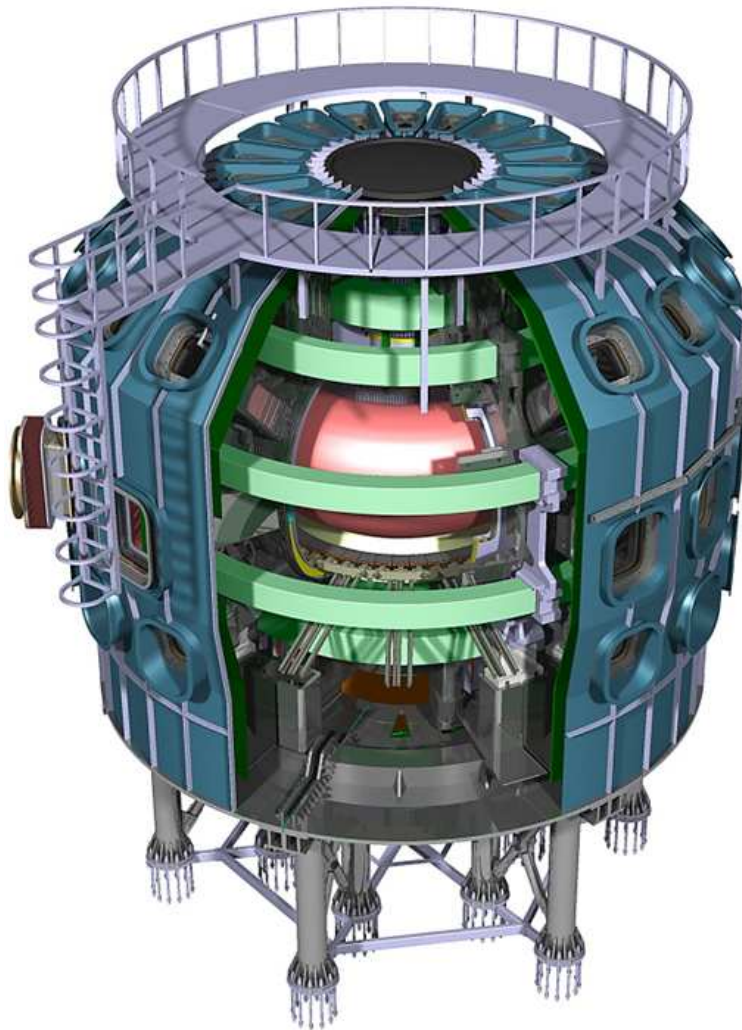
Figure 2.14: Representation of DTT [15]

Bibliography

[1] Smirnov, V. P. (2009). Tokamak foundation in USSR/Russia 1950–1990. Nuclear fusion, 50(1), 014003.

[2] The JET Team, The JET Project - Design Proposal, Rep. EURJET-R5, CEC, Brussels (1975).

[3] Creely, A. J., Greenwald, M. J., Ballinger, S. B., Brunner, D., Canik, J., Doody, J., ... & Sparc Team. (2020). Overview of the SPARC tokamak. Journal of Plasma Physics, 86(5), 865860502.

[4] Wesson, J., & Campbell, D. J. (2011). Tokamaks (Vol. 149). Oxford university press.

[5] Schuller, F. C. (1995). Disruptions in tokamaks. Plasma Physics and Controlled Fusion, 37(11A), A135.

[6] De Vries, P. C., Johnson, M. F., Alper, B., Buratti, P., Hender, T. C., Koslowski, H. R., ... & JET-EFDA Contributors. (2011). Survey of disruption causes at JET. Nuclear fusion, 51(5), 053018.

[7] Nedospasov, A. V. (2008). Thermal quench in tokamaks. Nuclear fusion, 48(3), 032002.

[8] Hender, T. C., Wesley, J. C., Bialek, J., Bondeson, A., Boozer, A. H., Buttery, R. J., ... & Zohm, H. (2007). MHD stability, operational limits and disruptions. Nuclear fusion, 47(6), S128.

[9] R Pánek et al 2016 Plasma Phys. Control. Fusion 58 014015

[10] Panek R et al 2006 Czech. J. Phys. 56 B125

[11] Weinzettl V et al 2011 Fusion Eng. Des. 86 1227–31

[12] ipp.cas.cz/vedecka_struktura_ufp/tokamak/COMPASS/systemy/magneticke-civky.html

[13] Martone R. et al., DTT Divertor Tokamak Test facility Interim Design Report, ENEA (ISBN 978-88-8286-378-4), April 2019 ("Green Book"), https://www.dtt-dms.enea.it/share/s/avvglhVQT2aSkSgV9vuEtw.

[14] https://www.iter.org/mach/magnets

[15] https://www.dtt-project.it/

3
Equilibrium codes

T<small>HIS</small> chapter describes the characteristics of some of the equilibrium codes capable to evaluate the magnetic field in the region of interest, along with some useful numerical tools.

3.1 Overview on equilibrium codes

The activity described in this thesis requires an accurate and reliable description of the magnetic flux density field map on the vessel surface, before and during a transient event, such as disruptions or plasma instabilities. The reasons will be explored further in the following chapter, where the details of the formulation will be addressed; and it will be clarified the important role of the magnetic field. In fact, in order to evaluate the total magnetic force on a structure, the volume integration of the cross product between the current density and the magnetic field is required; then, both vectors are necessary. The method applied in this thesis is based on an application on fusion devices of the Maxwell stress tensor theory, that allows to evaluate the total force acting on a volume from the knowledge of the magnetic field only on a surface.

During transient events, the equilibrium of the plasma can be severely disrupted, and its behavior can become highly non-linear. Equilibrium codes can be used to predict how the magnetic flux density field will evolve. In literature, a vast set of numerical codes are available, also with the purpose to analyse the electromagnetic interaction between the plasma and the surrounding structures [1]-[16].

Most of these codes solve MHD equations. For the ones that treat the plasma with two-dimensional (2D) models, the resulting equilibrium solution is related to the poloidal magnetic flux, that can be used to calculate the solution for the magnetic flux density field. Instead, in case of three-dimensional (3D) codes, the map of the flux density field is directly obtained.

Not all available codes are able to find a solution during a transient phenomenon. In the following, a set of equilibrium codes will be described: the CarMa0NL code [17], a technique based on Chebyshev polynomials interpolation of the magnetic flux density field [18, 19], and the EFIT code [20, 21]. CarMa0NL can be considered a "direct" tool able to find the equilibrium once the currents in the conductors and some physical characteristics of the plasma have been provided. The same is for the technique base on Chebyshev polynomial, that requires only the description of the device sources (plasma, conductors, structures) from an electromagnetic point of view. Instead, EFIT is an "inverse" tool, capable to give the equilibrium solution from diagnostics data. The characteristics of each one will be described in the dedicated sections.

The candidate's scientific contribution, concerning this chapter, was focused on the CarMa0NL tool, in particular its direct use to carry out simulations of disruptions, as will be clarified shortly.

3.2   CarMa0NL

CarMa0NL is a computational tool able to solve the nonlinear evolution of an axisymmetric plasma in the limits of the evolutionary equilibrium, in presence of 3D conductors modeling the Tokamak structures, during transient events. The meaning of "evolutionary equilbrium" will be specified shortly.

The main limitation of this tool is the assumption of the 2D plasma behavior, while the structures are 3D. In principle, a perturbation of the plasma produces 3D eddy currents in the structures, that in turn should cause 3D perturbations in the plasma. For this code, these perturbations are averaged along the toroidal angle.

The interaction between the 2D plasma and the 3D structures is made possible using a suitable coupling surface that allows to use different approaches for the plasma in the domain Ω (inside the surface) and the structures (outside). More specifically, for the plasma it is used an approach similar to the one used in CarMa [12], but with a non-linear behavior, while for the conductors is used the CARIDDI approach [15].

It is beyond the scope of this thesis to provide an accurate description of the tool. Only the most important information will be given.

For the part inside the coupling surface, the mathematical formulation considers the MHD equations, in the magneto-quasi-static limit for the Maxwell equations, and neglecting the viscous force in the momentum balance. Some of these equations have been already recalled in Ch. 1, and are here reported for convenience:

$$\boldsymbol{\nabla} \times \boldsymbol{E} = -\frac{\partial \boldsymbol{B}}{\partial t} \tag{3.1}$$

$$\boldsymbol{\nabla} \times \boldsymbol{H} = \boldsymbol{J} \tag{3.2}$$

$$\boldsymbol{\nabla} \cdot \boldsymbol{B} = 0 \tag{3.3}$$

$$\frac{\partial \rho}{\partial t} + \boldsymbol{\nabla} \cdot (\rho \boldsymbol{v}) = 0 \tag{3.4}$$

$$\frac{\partial (\rho \boldsymbol{v})}{\partial t} + \boldsymbol{\nabla} \cdot (\rho \boldsymbol{v} \boldsymbol{v}) = \boldsymbol{J} \times \boldsymbol{B} - \boldsymbol{\nabla} p \tag{3.5}$$

$$\frac{\partial p}{\partial t} + \boldsymbol{v} \cdot \boldsymbol{\nabla} p + \Gamma p \boldsymbol{\nabla} \cdot \boldsymbol{v} = 0 \tag{3.6}$$

$$\boldsymbol{E} + \boldsymbol{v} \times \boldsymbol{B} = \eta_p \boldsymbol{J} \tag{3.7}$$

Eqs. (3.1),(3.2) and (3.3) are Maxwell equations in the magneto-quasi-static limit, (3.4) is the plasma mass continuity, (3.5) is the momentum balance without the viscous force, (3.6) is the adiabatic law, where $\Gamma = 5/3$ is the specific heat ratio, and (3.7) is the generalized Ohm's law, where η_p is the plasma resistivity.

Then, the plasma mass density is neglected: from a physical point of view, this means that the plasma moves instantaneously between equilibrium states; which is an evolutionary equilibrium. This happens when the time evolution of the plasma is ruled by the electromagnetic dynamics of the conductors surrounding the plasma, and it is the case of position and shape control, vertical displacement, and others [17]. This allows to exclude (3.4), and (3.5) becomes:

$$\boldsymbol{J} \times \boldsymbol{B} - \nabla p = 0 \tag{3.8}$$

This hypothesis is considered valid when the time scale of the phenomena of interest is much longer than the time of Alfvén. This is in general verified in a wide range of events [6, 12, 22, 23]. From these assumptions, it is possible to obtain the classical Grad-Shafranov equation, already introduced and explained in Ch. 1 in (1.57), valid in all Ω. Defining $\partial \Omega$ as the boundary of the coupling surface, the equation to be solved is:

$$\begin{aligned} L\psi &= j_\phi(\psi) \\ \psi_{|\partial\Omega} &= \hat{\psi} \end{aligned} \tag{3.9}$$

where L is the Grad-Shafranov operator, ψ is the magnetic flux per radian, j_ϕ is the plasma toroidal current density and $\hat{\psi}$ is an unknown boundary condition, that can be written as the sum of two contributions, one from the plasma ($\hat{\psi}_p$), one from the external conductors ($\hat{\psi}_e$):

$$\hat{\psi} = \hat{\psi}_p + \hat{\psi}_e \tag{3.10}$$

The plasma toroidal current density j_ϕ is a function of the magnetic flux:

$$j_\phi(\psi) = \frac{f}{\mu_0 r}\frac{df}{d\psi} + r\frac{dp}{d\psi} \tag{3.11}$$

where f is the poloidal current function per radian, related to the toroidal magnetic field by $B_\phi = f/r$, and p, already defined, is the plasma pressure. But j_ϕ is also a function of a set of parameters: $\underline{s} = \lambda$, which depends on the total toroidal plasma current I_p, and $\underline{w} = [\alpha_m \alpha_n \beta_0]$, which depends on the plasma internal inductance l_i and the poloidal beta β_p. From [6]:

$$j_\phi(\psi, \underline{s}, \underline{w}) = \lambda\left[(1 - \beta_0)\frac{R_0}{r} + \beta_0\frac{r}{R_0}\right]\left(1 - \bar{\psi}^{\alpha_m}\right)^{\alpha_n}$$
$$\bar{\psi} = \frac{\psi - \psi_A}{\psi_B - \psi_A} \tag{3.12}$$

where ψ_A and ψ_B are the magnetic flux values, respectively, on the magnetic axis and on the plasma boundary. From this, giving a weak form of (3.9) and using a finite element formulation, it is possible to obtain a numerical solution for the magnetic flux in Ω that depends only on the contributions of the external sources to the boundary condition $\hat{\psi}$ and on the plasma parameters previously mentioned.

For the part outside the coupling surface, in order to ensure the solenoidality of the current density, a vector potential $\boldsymbol{T}$ is introduced, such as:

$$\boldsymbol{J} = \nabla \times \boldsymbol{T} \tag{3.13}$$

Then, using again a finite element approach, this time with 3D elements, it is possible to write:

$$\boldsymbol{T} = \sum_k I_k \boldsymbol{N_k} \tag{3.14}$$

where k span the number of edges of the 3D mesh, and $\boldsymbol{N_k}$ are the basis functions that represent numerically the vector potential.

In this way, it is possible to obtain a formulation for the contribution of the external conductors to the boundary conditions in (3.9) that depends

only on the values I_k in (3.14) and on a set of matrices obtainable from the knowledge of the geometry of the structures.

Combining the two approaches, the final system is a nonlinear equations system, where the unknowns are the values of ψ at the nodes of the 2D mesh inside Ω, and depends on the values I_p, l_i and β_p. These quantities are considered given. From these solutions, it is possible to obtain the value of the magnetic flux density field in any point of the external structures domain. A deeper formulation is present in [17] and related papers.

The CarMa0NL code has been used successfully on several devices (e.g. JET, COMPASS) in order to study the consequences of various kind of disruptions or plasma instabilities on the surrounding structures, especially in terms of the magnetic forces applied on the vessel. This is particularly useful for the scope of the activity presented in this thesis. In fact, the code is capable to calculate the field on the vessel surface during the disruption, and also the magnetic force acting on the structure, just performing the vector multiplication between the current density and the field inside each 3D element of the mesh. This makes the code an excellent way to validate the method here developed.

3.3 The Chebyshev polynomials interpolation approach

In modern Tokamaks, the complexity and high number of conductors that must be modeled can make the magnetic flux density field calculation very demanding in terms of computational burden, in particular when a 3D map is required. In fact, in this case, an accurate description of the conductors and of the plasma is necessary. For this reason, an interesting approach able to provide a solution for the equilibrium field is to perform an interpolation of the field in the points where it is necessary, instead of a direct calculation. Here, a method based on Chebyshev polynomials for the interpolation of the magnetic flux density field is described. Chebyshev polynomials are capable to represent smooth functions very efficiently [24, 25], which is the case of the magnetic field inside a Tokamak device. This, together with their simple numerical implementation and some interesting properties that will be recalled in the paragraph, has led to preferring the use of Chebyshev polynomials over other interpolation methods.

Despite this method has not been used for the force calculations that will be described in the next chapters, it is an interesting possible development in future related activities, due to its capability to evaluate the field in a large

set of points, located everywhere in the structure, as shown in the following.

Let's consider a domain V_I, where a set of N_{samp} sampling points has been selected. Each point of this domain is represented with a cartesian coordinates system $[x, y, z]$. V_I is a parallelepiped, geometrically defined by the intervals $\Delta x = x_2 - x_1$, $\Delta y = y_2 - y_1$ and $\Delta z = z_2 - z_1$. The points in V_I are mapped in the domain V_M, in which the points $[\tilde{x}, \tilde{y}, \tilde{z}]$ are such that:

$$\begin{bmatrix} -1 \leq \tilde{x} \leq 1 \\ -1 \leq \tilde{y} \leq 1 \\ -1 \leq \tilde{z} \leq 1 \end{bmatrix} \tag{3.15}$$

This can be made through the transformation:

$$\begin{bmatrix} \tilde{x} = 2\frac{x-x_1}{x_2-x_1} - 1 \\ \tilde{y} = 2\frac{y-y_1}{y_2-y_1} - 1 \\ \tilde{z} = 2\frac{z-z_1}{z_2-z_1} - 1 \end{bmatrix} \tag{3.16}$$

This domain can also rotate. In order to take into account this, a rotation matrix $\underline{M_{rot}}$ of dimensions 3×3 is introduced. Taking into account the solenoidality of $\boldsymbol{B}$, it is possible to define a magnetic vector potential $\boldsymbol{A}$ with components $[A_x\hat{\boldsymbol{x}}, A_y\hat{\boldsymbol{y}}, A_z\hat{\boldsymbol{z}}]$, calculated in the point $\boldsymbol{r}$ with components $[x, y, z]$ in the domain V_I. It is possible to write:

$$\boldsymbol{A}(\boldsymbol{r}) \approx \sum_{i=0}^{i=N_x} \sum_{j=0}^{j=N_y} \sum_{k=0}^{k=N_z} T_i(\tilde{x})T_j(\tilde{y})T_k(\tilde{z})[\alpha_{ijk}\hat{\boldsymbol{x}} + \beta_{ijk}\hat{\boldsymbol{y}} + \gamma_{ijk}\hat{\boldsymbol{z}}] \tag{3.17}$$

where N_x, N_y e N_z are the orders of the polynomials for the corresponding side of the domain, α_{ijk}, β_{ijk} and γ_{ijk} are the coefficients of the polynomials, $T_i(\zeta)$ is the Chebyshev polynomial of the first kind of order i, calculated in the point ζ in the interval $[-1, 1]$. For convenience, the expression for $Ti(\zeta)$ and its derivative is here reported:

$$T_i(\zeta) = \cos(n \arccos(\zeta)) \tag{3.18}$$

$$U_i(\zeta) = \frac{\sin((n+1)\arccos(\zeta))}{\sin(\arccos(\zeta))} \tag{3.19}$$

$$\frac{\partial T_i(\zeta)}{\partial \zeta} = nU_{i-1}(\zeta) \tag{3.20}$$

where $|\zeta| < 1$, $i \geq 0$, $U_i(\zeta)$ is the Chebyshev polynomial of the second kind of order i, and $U_{-1}(\zeta) = 0$.

Let's impose the following gauge on $\boldsymbol{A}(\boldsymbol{r})$:

$$div(\boldsymbol{A}(\boldsymbol{r})) = \frac{\partial A_x}{\partial x} + \frac{\partial A_y}{\partial y} + \frac{\partial A_z}{\partial z} = 0 \tag{3.21}$$

The field $\boldsymbol{B}(\boldsymbol{r})$ can be obtained with the curl of $\boldsymbol{A}(\boldsymbol{r})$:

$$\boldsymbol{B}(\boldsymbol{r}) \approx \sum_{i=0}^{i=N_x} \sum_{j=0}^{j=N_y} \sum_{k=0}^{k=N_z} \boldsymbol{\nabla} \times (T_i(\tilde{x}) T_j(\tilde{y}) T_k(\tilde{z})) [\alpha_{ijk}\hat{\boldsymbol{x}} + \beta_{ijk}\hat{\boldsymbol{y}} + \gamma_{ijk}\hat{\boldsymbol{z}}] \tag{3.22}$$

Eq. (3.21) allows to impose another equation to the system, for a total of four equations for each point.

In matrix formulation:

$$\begin{bmatrix} B_x^{ijk}(\boldsymbol{r}) \\ B_y^{ijk}(\boldsymbol{r}) \\ B_z^{ijk}(\boldsymbol{r}) \\ 0 \end{bmatrix} = \underline{\underline{M}}_C \begin{bmatrix} \alpha_{ijk} \\ \beta_{ijk} \\ \gamma_{ijk} \end{bmatrix} \tag{3.23}$$

where $\underline{\underline{M}}_C$ is a matrix that contain the values of the polynomials and their derivatives in (3.22). To obtain the coefficients α_{ijk}, β_{ijk} and γ_{ijk}, it is sufficient to calculate $\underline{\underline{M}}_C$ and the value of $\boldsymbol{B}$ in a suitable number of sampling points for each side (N_{sampx}, N_{sampy}, N_{sampz}) and perform an inversion (or psedudo-inversion). In this way, the matrix will have $N_{rows} = 4 \cdot N_{samp}$ rows e $N_{columns} = 3 \cdot (N_x+1) \cdot (N_y+1) \cdot (N_z+1)$ columns. In order to have an overdetermined system, it is necessary to impose $N_{rows} > N_{columns}$. For this reason, if the number of sampling points and the polynomials order is supposed the same for each side, such as $N_x = N_y = N_z = N_{pol}$ and $N_{sampx} = N_{sampy} = N_{sampz} = N_{side}$, it is sufficient to impose $N_{side} >= N_{pol}+1$. A possible choice is the equality $N_{side} = N_{pol} + 1$, that reduces at the minimum the number of sampling points required. The accuracy of the interpolation depends on the number of sampling points, the order of the polynomials, and the dimensions of the domain. The choice of these parameters is, naturally, strongly dependent on the smoothness of the field inside the domain: if it is mainly uniform, a low number of samplings and a low order are sufficient to obtain the required accuracy, otherwise, a strongly space-varying field requires more samplings and a greater polynomials order.

This approach has several strength points. It is independent on how the field is calculated in the sampling points, to obtain the coefficients α_{ijk}, β_{ijk} and γ_{ijk} in (3.23). Once it has been done, the original sources can be disregarded. For this reason, the method is very general and can be applied, for example, as a post-processor for an actual equilibrium code, that provides

the field on the sampling points. Once the Chebyshev polynomials coefficients
have been evaluated, it is no more necessary to use the actual sources to
calculate the field inside the domain, but is sufficient to evaluate the value
of Chebyshev polynomials and their derivatives in the points where required,
and then perform a matrix multiplication. About this, an useful property
of the Chebyshev polynomials is that a derivative of the polynomial with a
certain degree is still a Chebyshev polynomial, as seen in (3.20). This allow to
implement very easily the calculation of the polynomial values. In addition,
since every domain the domain V_I is always mapped in the interval [-1,1]
for each side, the interpolating function is certainly bounded in this interval,
since the Chebyshev polynomials assume the maximum (1) or minimum (-1)
value in 1 or -1 in abscissa.

To apply the method on the entire volume of a Tokamak device or, in
general, a part of it, a possible approach is to cover it with a set of domains,
each one with its pre-calculated polynomials coefficients. Once the field in
a point is required, it is sufficient to find the coefficients corresponding to
the domain where that point is located, and proceed as previously explained.
An example of a volume covered by a set of domains is sketched in Fig. 3.1.
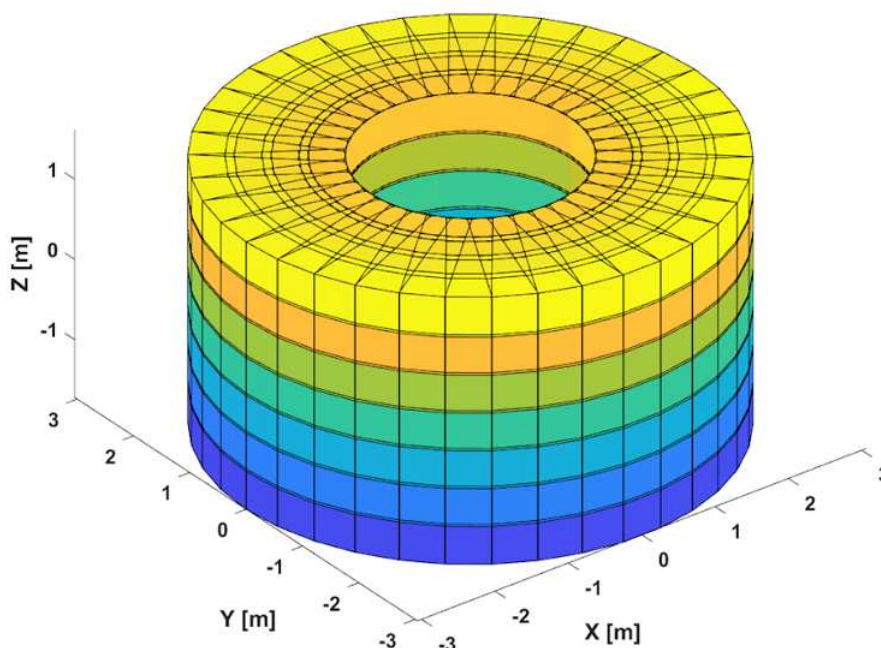A disadvantage of the method is about the initial calculation required to

Figure 3.1: Example of a volume covered by a set of domains [19]

obtain the Chebyshev polynomials coefficient, that can be very demanding,

especially when the sources are numerous and a high interpolation accuracy is required. Furthermore, it can be necessary to provide the coefficients for a high number of domains, when their volume is much smaller than the volume to cover. By consequence, since for each domain is necessary to memorize a certain number of coefficients, the request of memory in the computation device can be expensive. The Chebyshev polynomials interpolation approach has been successfully used as a tool for the fast tracking of magnetic field lines in a Tokamak [18], in order to evaluate the connection length [19]. Other applications are under study.

3.4 EFIT

EFIT [20, 21] is a code capable to reconstruct the plasma shape and the plasma current density, satisfying the MHD equilibria. From the knowledge of these measurements, only global parameters are obtainable, such as the total plasma current I_p, and some information about β_p and l_i. The method is based on the parametrization of the plasma toroidal current density j_ϕ in terms of these quantities. Then, the use of the Green's function approach to compute MHD equilibrium, using the Grad-Shafranov equation, allows to compute the magnetic flux with an iterative scheme, specifically Picard. At each step, the solution of the flux is obtained through the knowledge of j_ϕ at the previous step, that is obtained, as said, from the measurements. The method is particularly useful for Tokamaks with an air core, but a modified version was developed specifically to handle iron cores, like in JET device [21]. EFIT has been successfully used in this device, in COMPASS, and many others.

From the poloidal flux provided by the tool, using (1.35) and (1.36), it is possible to evaluate numerically the field. For this application, the derivative has been implemented using a finite differences method.

The characteristics of the method allow to study only purely 2D equilibrium fields. For this reason, it is not useful during a transient event where a 3D perturbation of the field is present. For the scope of this thesis, EFIT is used to obtain the equilibrium field at the beginning of the disruption, that can be considered 2D with a good approximation. The use of this field will be clarified in the following chapters.

Bibliography

[1] Albanese, R., Blum, J., & De Barbieri, O. (1987, September). Numerical studies of the Next European Torus via the PROTEUS code. In 12th Conf. on Numerical Simulation of Plasmas, San Francisco.

[2] Barabaschi, P. (1993). The MAXFEA code, ITER EDA Plasma Control. In Technical Meeting, Naka, Japan.

[3] Albanese, R., Mattei, M., Calabr, G., & Villone, F. (2003). Unified treatment of forward and inverse problems in the numerical simulation of tokamak plasmas.

[4] Khayrutdinov, R. R., & Lukash, V. E. (1993). Studies of plasma equilibrium and transport in a tokamak fusion device with the inverse-variable technique. Journal of Computational Physics, 109(2), 193-201.

[5] Jardin, S. C., Pomphrey, N., & Delucia, J. (1986). Dynamic modeling of transport and positional control of tokamaks. Journal of computational Physics, 66(2), 481-507.

[6] Albanese, R., & Villone, F. (1998). The linearized CREATE-L plasma response model for the control of current, position and shape in tokamaks. Nuclear Fusion, 38(5), 723.

[7] Kavin, A. A., Belyakov, V. A., Bulgakov, S. A., Kostsov, Y. A., Rumyntsev, E. N., Galkin, S. A., ... & Yagnov, V. A. (1997). Numerical simulation of plasma equilibrium and shape control in tight tokamak GLOBUS-M. In Fusion Technology 1996 (pp. 821-824). Elsevier.

[8] Bondeson, A., Vlad, G., & Lütjens, H. (1992). Resistive toroidal stability of internal kink modes in circular and shaped tokamaks. Physics of Fluids B: Plasma Physics, 4(7), 1889-1900.

[9] Liu, Y. Q., Bondeson, A., Fransson, C. M., Lennartson, B., & Breitholtz, C. (2000). Feedback stabilization of nonaxisymmetric resistive

wall modes in tokamaks. I. Electromagnetic model. Physics of Plasmas, 7(9), 3681-3690.

[10] Bialek, J., Boozer, A. H., Mauel, M. E., & Navratil, G. A. (2001). Modeling of active control of external magnetohydrodynamic instabilities. Physics of Plasmas, 8(5), 2170-2180.

[11] Strumberger, E., Merkel, P., Sempf, M., & Günter, S. (2008). On fully three-dimensional resistive wall mode and feedback stabilization computations. Physics of Plasmas, 15(5).

[12] Portone, A., Villone, F., Liu, Y., Albanese, R., & Rubinacci, G. (2008). Linearly perturbed MHD equilibria and 3D eddy current coupling via the control surface method. Plasma Physics and Controlled Fusion, 50(8), 085004.

[13] Park, W., Belova, E. V., Fu, G. Y., Tang, X. Z., Strauss, H. R., & Sugiyama, L. E. (1999). Plasma simulation studies using multilevel physics models. Physics of Plasmas, 6(5), 1796-1803.

[14] Czarny, O., & Huysmans, G. (2008). Bézier surfaces and finite elements for MHD simulations. Journal of computational physics, 227(16), 7423-7445.

[15] Albanese, R., & Rubinacci, G. (1988). Integral formulation for 3D eddy-current computation using edge elements. IEE Proceedings A (Physical Science, Measurement and Instrumentation, Management and Education, Reviews), 135(7), 457-462.

[16] Miki, N., Verrecchia, M., Barabaschi, P., Belov, A., Chiocchio, S., Elio, F., ... & Utin, Y. (2001). Vertical displacement event/disruption electromagnetic analysis for the ITER-FEAT vacuum vessel and in-vessel components. Fusion engineering and design, 58, 555-559.

[17] Villone, F., Barbato, L., Mastrostefano, S., & Ventre, S. (2013). Coupling of nonlinear axisymmetric plasma evolution with three-dimensional volumetric conductors. Plasma Physics and Controlled Fusion, 55(9), 095008.

[18] Albanese, R., Chiariello, A. G., Fresa, R., Iaiunese, A., Martone, R., & Zumbolo, P. (2022). Effectiveness of the Chebyshev Approximation in Magnetic Field Line Tracking. Energies, 15(20), 7619.

[19] Albanese, R., Chiariello, A. G., Di Grazia, L. E., Iaiunese, A., Martone, R., Mattei, M., ... & Zumbolo, P. (2023). Three-dimensional evaluation of the connection lengths in a Tokamak. Fusion Engineering and Design, 192, 113622.

[20] Lao, L. L., John, H. S., Stambaugh, R. D., Kellman, A. G., & Pfeiffer, W. (1985). Reconstruction of current profile parameters and plasma shapes in tokamaks. Nuclear fusion, 25(11), 1611.

[21] O'Brien, D. P., Lao, L. L., Solano, E. R., Garribba, M., Taylor, T. S., Cordey, J. G., & Ellis, J. J. (1992). Equilibrium analysis of iron core tokamaks using a full domain method. Nuclear fusion, 32(8), 1351.

[22] Albanese, R., Mattei, M., & Villone, F. (2004). Prediction of the growth rates of VDEs in JET. Nuclear fusion, 44(9), 999.

[23] Lazarus, E. A., Lister, J. B., & Neilson, G. H. (1990). Control of the vertical instability in tokamaks. Nuclear Fusion, 30(1), 111.

[24] Trefethen, L. N. (2007). Computing numerically with functions instead of numbers. Mathematics in Computer Science, 1, 9-19.

[25] Trefethen, L. N. Approximation Theory and Approximation Practice, SIAM, Philadelphia, 2013. Cited on, 426.

4

Force calculation

THIS chapter is focused on the description of the mathematical model of the technique capable to evaluate the net total forces on the vessel during a disruption, from the knowledge of the magnetic measurements only. The original contribution of this activity is focused on the development of part of this method.

4.1 The magnetic forces

The calculation of the magnetic forces acting on the vessel of a Tokamak is critical for the analysis of the robustness of the device, especially during transient phenomena. In fact, when the equilibrium field is stationary, the eddy currents induced into the structures are negligible (theoretically zero), as well as the forces. During a disruption, or a plasma instability, with the plasma-wall interaction, there is a sudden release of the energy from the plasma. This may lead to non-negligible displacement in the vessel, that can potentially cause serious damages.

In the activity here described, the total net magnetic forces are basically subdivided in two kinds: sideways (F_x and F_y) and vertical (F_z) (Fig. 4.1). The vertical force is mainly due to the component of the field independent on the toroidal angle, which is the axis-symmetric component, during the disruption, while the sideways forces are due to the other components.

Here it will be shown how it is possible to obtain a formulation, for the calculation of these forces, using only the knowledge of the field on the external surface of the vessel. The basis of this model is taken from [1, 2].
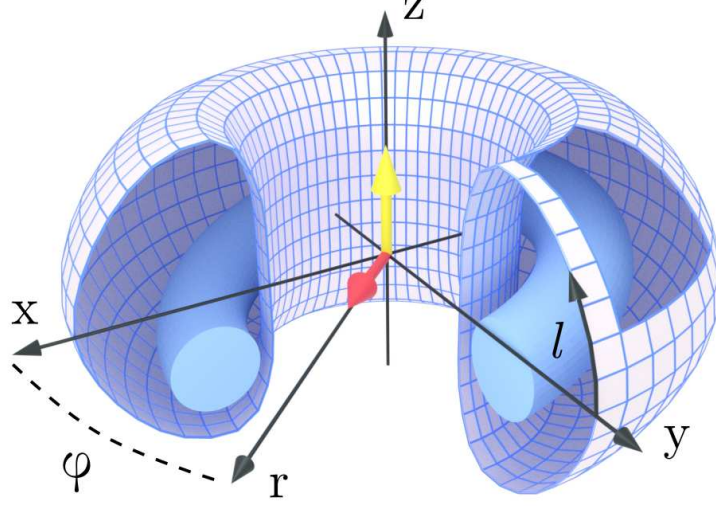
Figure 4.1: An example of net forces on the vessel [3]. A disrupted plasma (the light blue, deformed toroid) inside a non-axialsymmetric vessel causes such forces. The vertical is in the yellow direction (z-axis), the sideways in the red direction (radial). In the picture, also the cartesian directions and the direction tangent to the poloidal section of the vessel (l) are sketched.

In a Tokamak, the components that magnetically interact during a disruption are basically four: the plasma (p), the vessel (v), the poloidal (*pol*) and toroidal (t) coils. Then, in general, the net total force acting on a generic component c_1 due to the component c_2 is:

$$\boldsymbol{F}_{c_1 c_2} = \int_{V_{c_1}} \boldsymbol{j}_{c_1} \times \boldsymbol{B}_{c_2} dV \tag{4.1}$$

where $\boldsymbol{j}_{c_1}$ is the current density inside the element c_1, $\boldsymbol{B}_{c_2}$ is the field generated by the element c_2 inside c_1, and the integration is extended to V_{c1}, the volume of c_1.

Considering the previously introduced four components, the total force on the vessel is:

$$\boldsymbol{F}_v = \boldsymbol{F}_{vv} + \boldsymbol{F}_{vp} + \boldsymbol{F}_{vpol} + \boldsymbol{F}_{vt} \tag{4.2}$$

while the total force on plasma is:

$$\boldsymbol{F}_p = \boldsymbol{F}_{pp} + \boldsymbol{F}_{pv} + \boldsymbol{F}_{ppol} + \boldsymbol{F}_{pt} \tag{4.3}$$

Let's introduce the following definitions:

$$\begin{aligned} \boldsymbol{F}_{ii} &= \boldsymbol{F}_{pp} + \boldsymbol{F}_{pv} + \boldsymbol{F}_{vv} + \boldsymbol{F}_{vp} \\ \boldsymbol{F}_{ie} &= \boldsymbol{F}_{ppol} + \boldsymbol{F}_{pt} + \boldsymbol{F}_{vpol} + \boldsymbol{F}_{vt} \end{aligned} \tag{4.4}$$

which are, respectively, the net forces on the currents $\boldsymbol{j}_p$ and $\boldsymbol{j}_v$ due to their own fields $\boldsymbol{B}_p$ and $\boldsymbol{B}_v$, and the forces on the same currents due to the external sources' fields $\boldsymbol{B}_{pol}$ and $\boldsymbol{B}_t$. This means that, from a physical point of view, the force $\boldsymbol{F}_{ii}$ is the contribution to the force on the plasma + vessel system due to the "internal" sources, namely the plasma and the vessel themselves, while $\boldsymbol{F}_{ie}$ is the contribution due to all the sources external to the vessel. Summing together (4.2) and (4.3), and using definitions (4.4), is possible to obtain:

$$\boldsymbol{F}_p + \boldsymbol{F}_v = \boldsymbol{F}_{ii} + \boldsymbol{F}_{ie} \tag{4.5}$$

It is worth to underline that the net total force $\boldsymbol{F}_{ii}$ has to be zero [1]. This is due to the fact that the system $plasma + vessel$ can be considered as a closed conductor, electrically isolated from the external, and the currents are present only in a finite volume.

From the Maxwell equations $\boldsymbol{j} = \nabla \times \boldsymbol{B}/\mu_0$ and $\nabla \cdot \boldsymbol{B} = 0$, it is possible to write:

$$\mu_0 \boldsymbol{j} \times \boldsymbol{B} = -\nabla \left(\frac{\boldsymbol{B}^2}{2} \right) + (\boldsymbol{B} \cdot \nabla) \boldsymbol{B} \tag{4.6}$$

Here, the field considered in (4.6) is the total field due to all the sources, internal and external to the vessel, while the current density is the one present into the "internal" sources, plasma and vessel. Substituting into (4.1), the following is obtained:

$$\boldsymbol{u} \cdot \boldsymbol{F}_v = \frac{1}{\mu_0} \oint_{vessel+} \left[(\boldsymbol{u} \cdot \boldsymbol{B})\boldsymbol{B} - \frac{\boldsymbol{B}^2}{2}\boldsymbol{u} \right] \cdot d\boldsymbol{S} - \boldsymbol{u} \cdot \boldsymbol{F}_p \tag{4.7}$$

where $\boldsymbol{u}$ is one of the three unitary vectors in x, y or z directions, and the integration is over the external surface of the vessel.

The total force F_p acting on the plasma, during a disruption, is in general considered zero. This is because the extremely low mass of the plasma multiplied by the estimation of its acceleration gives, usually, a force in the order of some $Newton$, a quantity considered absolutely negligible.

Furthermore, the integral in (4.7) can be extended to any axial-symmetric surface S_{ax} outside the vessel surface, not touching the external conductors. This is possible because the integral in (4.1) can be extended in the vacuum region between "vessel+" and S_{ax} and the result remain the same, since the current density is zero.

This considerations allow to obtain the following integral:

$$\boldsymbol{u} \cdot \boldsymbol{F}_v = \frac{1}{\mu_0} \oint_{S_{ax}} \left[(\boldsymbol{u} \cdot \boldsymbol{B})\boldsymbol{B} - \frac{\boldsymbol{B}^2}{2}\boldsymbol{u} \right] \cdot d\boldsymbol{S_{ax}} \tag{4.8}$$

Considering a transient event, at the initial equilibrium instant with $\boldsymbol{B} = \boldsymbol{B}_0$, the current density $\boldsymbol{j}_v$ in the vessel is zero, so is the net force. Let's define $\boldsymbol{b}$ as the perturbed field due to the action of the transient phenomena. Therefore, at any instant, it is possible to write:

$$\boldsymbol{B} = \boldsymbol{B}_0 + \boldsymbol{b} \tag{4.9}$$

It is possible to consider $\boldsymbol{B}_0$ as an axial-symmetric field, and then all the 3D residual components in the field lie within in the $\boldsymbol{b}$ component. It is worth to clarify that the total field $\boldsymbol{B}$ respects the solenoidality, and also the equilibrium field $\boldsymbol{B}_0$. For this reason, also the field $\boldsymbol{b}$ has a null divergence.

Since, typically, it results $\boldsymbol{b} << \boldsymbol{B}_0$, it is possible to obtain the following formulation for the component $\boldsymbol{u}$ of the total net force, carrying out a linearization of (4.8):

$$\boldsymbol{u} \cdot \boldsymbol{F}_W \approx \frac{1}{\mu_0} \oint_{S_{ax}} [(\boldsymbol{u} \cdot \boldsymbol{b})\boldsymbol{B}_0 + (\boldsymbol{u} \cdot \boldsymbol{B}_0)\boldsymbol{b} - (\boldsymbol{b} \cdot \boldsymbol{B}_0)\boldsymbol{u}] \cdot d\boldsymbol{S}_{\boldsymbol{ax}} \tag{4.10}$$

It is important to notice two results obtainable from (4.8) and (4.10). Let's consider a Fourier spectral decomposition of $n = 1, 2, ..., M_\phi$ finite components of the field $\boldsymbol{B}$ in sense of the toroidal angle ϕ. If $\boldsymbol{B}$ has only an axial-symmetric (the harmonic $n = 0$) component, the integral in the sideways directions (x and y) is zero, and only the vertical component of the force survives. Vice versa, the harmonics $n > 0$ are responsible of the sideways forces, and do not impact on the vertical one. Then, as said earlier, only the axial-symmetric component of the field contributes in F_z. This result can be easily obtained from the formulation (4.8): in fact, from the two terms inside the integral, let's perform the inner product with x (y) and z directed unitary vectors and the integration along the ϕ direction. For the x (y) direction, the result of the integral is different from zero only for the $n > 0$ harmonics of the field, while for the z direction the contrary happens.

In the past [2], only in case of plasma with circular and elliptic sections, it has been demonstrated analytically that only the $n = 1$ component contributes to the sideways forces. Despite the lack of such demonstration for plasma of general shape, the same behavior has been assumed also in this activity. In particular, based on the assumptions made, these components are possibly present only in the $\boldsymbol{b}$ field. Then, in the following, only the $n = 0, 1$ components will be considered, even if the formulation shown below is valid for every $n >= 0$ component. This formulation is the original contribution of this activity, to which the candidate has made his contribution.

The integrals (4.8) and (4.10) have been calculated with a numerical approximation. The integration surface is subdivided in a number N_s of

elementary surfaces s defined by certain $\Delta\phi$ and $\Delta\theta$ values, for simplicity constant on each surface element. Each point of the surface can be represented in both quasi-toroidal (ρ,ϕ,θ) (Fig. 1.2) and cylindrical (r,ϕ,z) (Fig. 1.3) coordinate systems. In both systems, the angle ϕ is the toroidal angle. In quasi-toroidal coordinates, ρ and θ are the radius and angle of a polar coordinate system placed in the poloidal section, where ρ is defined relative to an arbitrary center. Approximately, the field on the surfaces $\boldsymbol{B}_s$ and its contributions $\boldsymbol{B}_{0s}$ and $\boldsymbol{b}_s$ are considered uniform on the surface element, and equal to their values on the point at the center, P_s. The same approximation is made for the perpendicular unitary vector $\hat{\boldsymbol{p}}_s$. Then, the area A_s of each surface is so defined:

$$A_s = R_s \Delta\phi \rho_s \Delta\theta \tag{4.11}$$

where R_s and ρ_s are, respectively, the cylindrical and quasi-toroidal radial coordinates of P_s.

After these considerations, the numerical evaluations of (4.8) and (4.10) have been made with following formulations, respectively:

$$\boldsymbol{u} \cdot \boldsymbol{F}_W \approx \frac{1}{\mu_0} \sum_{s=1}^{N_s} \left[(\boldsymbol{u} \cdot \boldsymbol{B}_s)\boldsymbol{B}_s - \frac{\boldsymbol{B}_s^2}{2}\boldsymbol{u} \right] \cdot \hat{\boldsymbol{p}}_s A_s \tag{4.12}$$

$$\boldsymbol{u} \cdot \boldsymbol{F}_W \approx \frac{1}{\mu_0} \sum_{s=1}^{N_s} \left[(\boldsymbol{u} \cdot \boldsymbol{b}_s)\boldsymbol{B}_{0s} + (\boldsymbol{u} \cdot \boldsymbol{B}_{0s})\boldsymbol{b}_s - (\boldsymbol{b}_s \cdot \boldsymbol{B}_{0s})\boldsymbol{u} \right] \cdot \hat{\boldsymbol{p}}_s A_s \tag{4.13}$$

4.2 Evaluation of the field from the normal component

Considering an event as a disruption, the field $\boldsymbol{b}$ can be attributed to sources present inside the vessel external wall, e.g. the plasma and the vessel itself. This means that the eddy currents inside the conductors external to the vessel are considered zero, then the field $\boldsymbol{b}$ has a null curl:

$$\nabla \times \boldsymbol{b} = 0 \tag{4.14}$$

in the whole volume outside the vessel wall, since no sources of $\boldsymbol{b}$ are present there. Obviously, also the solenoidality is always true:

$$\nabla \cdot \boldsymbol{b} = 0 \tag{4.15}$$

This volume is a connected space, but not simply connected. For this reason, a magnetic scalar potential cannot be defined, despite (4.14) and

(4.15) are verified everywhere in the domain. In fact, it is not true that the
circuitation of the field on any closed curve contained on the volume is zero.
If a curve is the border of a surface that intersects the torus (the volume
of the vessel), the circuitation is related to the total net toroidal current
circulating inside the internal volume, that is a source of b. Naturally, if the
total net toroidal current is zero, the problem is not present and it is possible
to define a magnetic scalar potential. Two cases can be considered, in which
the total net toroidal current is zero:

a) during the transient event, the total toroidal current inside the internal
   volume remains constant, then it cannot be considered a source of b;

b) if a Fourier spectral decomposition of $n = 1, 2, ..., M_\phi$ finite harmonics
   of the field b is performed, in sense of the toroidal angle ϕ, for the $n > 0$
   harmonics a toroidal net current cannot exists, as it would also mean
   having an axial-symmetric component of b.

Here, only the case b) is treated, since the case a) is not very interesting
from a practical point of view. It will be seen in the immediate following
that, with this hypothesis, a method capable to obtain all the three compo-
nents of the field b from the knowledge of only its normal component can be
formulated. A double Fourier series (4.16) is performed on this component,
with respect to the poloidal and toroidal angles. The points at which it is
calculated will be clarified later.

$$
\begin{aligned}
b_\perp(\theta, \phi) \approx \sum_{n=0}^{M_\phi} \sum_{m=0}^{M_\theta} & A_{nm} cos(m\theta) cos(n\phi) + B_{nm} cos(m\theta) sin(n\phi) + \\
& + C_{nm} sin(m\theta) cos(n\phi) + D_{nm} sin(m\theta) sin(n\phi)
\end{aligned}
\tag{4.16}
$$

In (4.16), $b_\perp$ is the normal component of the field b on a certain surface,
M_ϕ and M_θ are the maximum expansion order in ϕ and θ directions respec-
tively, and A_{nm}, B_{nm}, C_{nm}, D_{nm} are suitable coefficients. The impact of the
$n = 0$ harmonic, and a way to evaluate it, is treated later in the chapter.

4.2.1 Case $n > 0$

The formulation here presented is applicable to any of the $n > 0$ harmonics
of the field. Let's consider only one of them. As already said, it is possible
to define a scalar function potential F_n, such as:

$$
b^n = \nabla F_n
\tag{4.17}
$$

where $\boldsymbol{b}^n$ is the $n > 0$ harmonic of $\boldsymbol{b}$. Furthermore, from (4.15) applied to $\boldsymbol{b}^n$, it results in:

$$\nabla^2 F_n = 0 \tag{4.18}$$

In a cylindrical coordinates system, (4.18) can be written as:

$$\frac{1}{r}\frac{\partial}{\partial r}\left(r\frac{\partial F_n}{\partial r}\right) + \frac{1}{r^2}\frac{\partial^2 F_n}{\partial \phi^2} + \frac{\partial^2 F_n}{\partial z^2} = 0 \tag{4.19}$$

Let's perform a factorization of the function F_n, assuming that it depends on ϕ as follows:

$$F_n(r,\phi,z) = f_n(r,z)g_n(\phi) = f_n(r,z)cos(n\phi - \phi_{0n}) \tag{4.20}$$

where ϕ_{0n} is the phase. Then, (4.19) can be expressed as:

$$-\frac{\partial}{\partial r}\left(r\frac{\partial f_n}{\partial r}\right) - \frac{\partial^2 f_n}{\partial z^2} + \frac{n^2}{r^2}f_n = 0 \tag{4.21}$$

Substituting the expression for ∇ as:

$$\nabla = \left[\frac{\partial}{\partial r}, \frac{\partial}{\partial z}\right] \tag{4.22}$$

The first two terms in (4.21) can be written as:

$$\frac{\partial}{\partial r}\left(r\frac{\partial f_n}{\partial r}\right) + \frac{\partial^2 f_n}{\partial z^2} = \frac{1}{r}\nabla \cdot (r\nabla f_n) \tag{4.23}$$

and hence, the equation becomes:

$$-\nabla \cdot (r\nabla f_n) + \frac{n^2}{r}f_n = 0 \tag{4.24}$$

$$-\nabla \cdot (r\nabla f_n) + \frac{n^2}{r}f_n = 0 \tag{4.25}$$

$$\nabla f_n \cdot \hat{\boldsymbol{p}} = f_{np} \text{ on } \delta\Omega_v \tag{4.26}$$

$$f_n = 0 \text{ with } r \to \inf \tag{4.27}$$

$$\nabla f_n = 0 \text{ with } r = 0 \tag{4.28}$$

where $\delta\Omega_v$ is the border of a section of an axial-symmetric surface outside the vessel external wall, and $\hat{\boldsymbol{p}}$ is the unitary vector perpendicular to such surface. Eqs. (4.26), (4.27) and (4.28) are a suitable set of Boundary Conditions (BC) for (4.25), in particular they are the Neumann conditions on a

finite boundary ($\delta\Omega_v$), the null Dirichlet conditions at infinity, and the null
Neumann conditions on $r = 0$. A deeper discussion about these conditions
is now necessary.

It results from (4.17):

$$\nabla F_n \cdot \hat{\boldsymbol{p}} = \boldsymbol{b}^n \cdot \hat{\boldsymbol{p}} = \boldsymbol{b}_\perp{}^n \qquad (4.29)$$

where $\boldsymbol{b}_\perp{}^n$ is the perpendicular component of the $\boldsymbol{b}^n$ field. From the point
of view of the measurements, the available perpendicular component $\boldsymbol{B}_\perp$ is
the one of the total $\boldsymbol{B}$ field. In order to obtain the Neumann conditions for
(4.26), the following steps may be defined:

- from the total measure $\boldsymbol{B}_\perp$, the perpendicular component of the axial-
  symmetric initial equilibrium field, $\boldsymbol{B}_{0\perp}$, is subtracted, obtaining the
  perturbed perpendicular component $\boldsymbol{b}_\perp$;

- the $n > 0$ component $\boldsymbol{b}_\perp{}^n$ of interest is extracted from $\boldsymbol{b}_\perp$;

- the values of $\boldsymbol{b}_\perp{}^n$ have to be chosen at a certain ϕ section, to obtain
  f_{np}; the best choice is the section $\phi = \phi_{0n}$.

The calculation of $\boldsymbol{b}_\perp$ from the measurements is immediate when $\boldsymbol{B}_{0\perp}$ is
known. For this reason, a proper equilibrium code is necessary, e.g. the
codes shown in the previous chapter.

To obtain $\boldsymbol{b}_\perp{}^n$ from $\boldsymbol{b}_\perp$, a finite series expansion in n must be provided.
The fact that the field is required on a toroidal surface, even with a non-
circular section, allows to implement (4.16), obviously using only the $n > 0$
harmonics in ϕ. The coefficients A_{nm}, B_{nm}, C_{nm}, D_{nm} can be evaluated from
the knowledge of $\boldsymbol{b}_\perp$ at the measurement points, and performing a matrix
inversion, after a suitable choice of M_ϕ and M_θ. From (4.16), it is sufficient
to disregard the components different from the required n to obtain $\boldsymbol{b}_\perp{}^n$.
Furthermore, the use of a Fourier expansion allows to evaluate the value of
$\boldsymbol{b}_\perp{}^n$ for every θ and ϕ, albeit with a certain approximation, and then also at
the required section ϕ_{0n}.

The method here described is general, and can be applied to any toroidal
surface, with a given section shape. In certain cases analytical solutions for
(4.18) are available [2]. Here, for the sake of generality, a numerical approach
has been preferred. The differential equation has been solved using the Fi-
nite Element Method (FEM), through an appropriate tool in MATLAB$^{®}$
environment. The borders of the domain are the following:

- a closed curve, coincident with the poloidal section of the surface exter-
  nal to the wall, where the Neumann conditions from $\boldsymbol{b}_\perp{}^n$ are applied;

- a semicircle that, rigorously, should be extended to infinite, with null Dirichlet conditions;

- a vertical segment along z axis, with null Neumann conditions.

The boundary conditions for each border are sketched in Fig. 4.2. The dis-
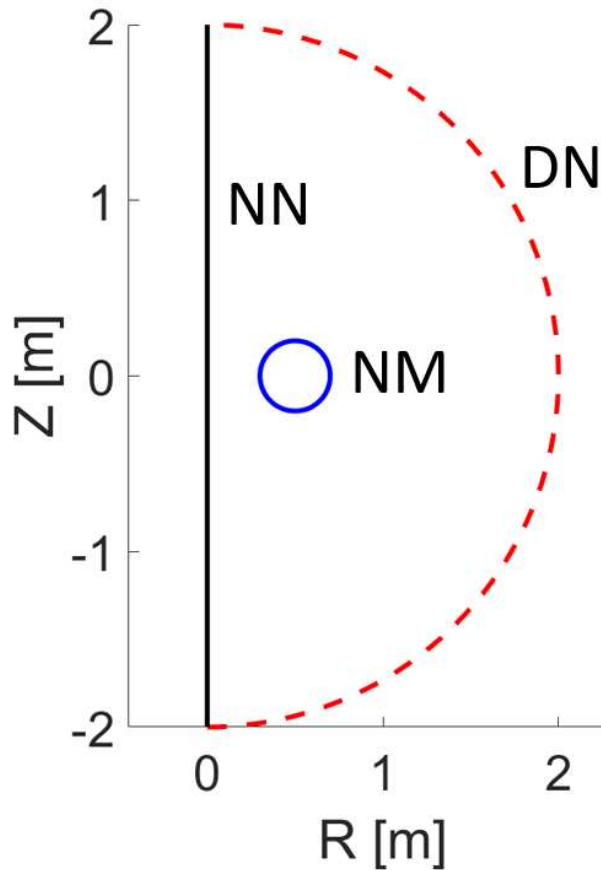

Figure 4.2: Scheme of the boundary conditions used: Neumann conditions from measurements (NM) on the surface external to the vessel in blue, Neumann null (NN) conditions on the z axis in black, and Dirichlet null (DN) conditions on the semicircle in dashed red.

cussion about the implementation of the Neumann conditions on the poloidal section of the vessel surface has already been addressed. Some considerations are needed for the other two conditions, on the semicircle and along the z axis.

Numerically, the condition at infinite cannot, obviously, be applied directly. Here an easy method has been implemented, albeit with a certain

level of accuracy, simply increasing the ray of the semicircle to a value for
which the solution of the differential equation can be considered negligible,
if compared with the solution on the vessel external surface. A paramet-
ric analysis has been carried out to determine it, considering the vessel of
COMPASS.

The null Neumann conditions on the vertical axis are rigorously correct
when the problem is axial-symmetric. In fact, with the formulation made
here, the Neumann condition coincides with the field $\boldsymbol{b_r}^{n=0}$, that must be
zero, due to the symmetry of the problem. In case of $n > 0$, instead, the $\boldsymbol{b_r}^n$
on the z axis is in general different from zero, and obviously variable with the
angle ϕ. No measurement is available in that area of the device, then it is not
possible to obtain the value of this field from the magnetic diagnostics. But,
as stated before, the only source of the perturbed field is inside the vessel
surface. Therefore, moving away from it, the value of the field must decrease.
In the activity here considered, the value of the perturbed radial field on the
z axis can be considered negligible compared with the field on the vessel
surface. For this reason, the Neumann conditions are simply considered null
also in $n > 0$ cases.

Once the solution f_n has been evaluated, the cylindrical components of
$\boldsymbol{b}^n$ can be computed as follows:

$$\boldsymbol{b_r}^n = \frac{\partial f_n(r, z)}{\partial r} cos(n\phi - \phi_{0n}) \tag{4.30}$$

$$\boldsymbol{b_\phi}^n = -n f_n(r, z) sin(n\phi - \phi_{0n}) \tag{4.31}$$

$$\boldsymbol{b_z}^n = \frac{\partial f_n(r, z)}{\partial z} cos(n\phi - \phi_{0n}) \tag{4.32}$$

From these, the cartesian components are immediate to obtain. The deriva-
tives in (4.30) and (4.32), and the value of $f_n(r, z)$ in (4.31) can be numerically
evaluated in any point from the solution of the differential equation and its
gradient on the mesh nodes, given by the MATLAB® tool, performing an
interpolation.

4.2.2   Case $n = 0$

The calculation of the vertical force, in this formulation, requires the knowl-
edge of also the tangent component on the external surface of the vessel. This
requirement does not change the main assumptions of this activity, that is
the use of the magnetic diagnostics to obtain the calculation of the total
forces, but surely introduces a grade of complexity, since a new kind of mea-
surements, different from the saddle coils, has to be added. Furthermore,

similarly to the problem with the saddle coils, the tangent field diagnostics are not always available on all the devices.

Despite this, it is still of interest to study this possible resolution, since it can be used when the field is obtained from equilibrium codes, or, in general, codes capable to give the tangent field on the surface vessel during a transient phenomena. Differently from the saddle coils case, this field is not required on different sections of the device, simply because it is necessary only for the axial-symmetric component. On COMPASS, an array of EPR coils is available at one section, then, in this case, the method is applicable.

Let's define the tangent field on the external vessel surface as $\boldsymbol{b}_{\parallel}$. Both this and perpendicular components can be expanded in a double Fourier truncated series expansion, as in (4.16). From this, it is sufficient to extract the $n = 0$ component, in order to have the perpendicular $\boldsymbol{b}_{\perp}{}^0$ and tangent $\boldsymbol{b}_{\parallel}{}^0$ axial-symmetric components anywhere on the surface approximately, which is allowed from the fact that a series expansion has been made. The toroidal component is automatically zero, since it cannot be generated in the axial-symmetric case.

From here, the radial $\boldsymbol{b}_r{}^0$ and vertical $\boldsymbol{b}_z{}^0$ components are easily obtainable, from the knowledge of the relation between the perpendicular and tangent unitary vectors with their radial and vertical homologues. In any point $\boldsymbol{r}$ of the surface, it is possible to say:

$$\begin{bmatrix} \boldsymbol{b}_{\perp}{}^0(\boldsymbol{r}) \\ \boldsymbol{b}_{\parallel}{}^0(\boldsymbol{r}) \end{bmatrix} = \begin{bmatrix} \boldsymbol{p}_r(\boldsymbol{r}) & \boldsymbol{p}_z(\boldsymbol{r}) \\ \boldsymbol{t}_r(\boldsymbol{r}) & \boldsymbol{t}_z(\boldsymbol{r}) \end{bmatrix} \begin{bmatrix} \boldsymbol{b}_r{}^0(\boldsymbol{r}) \\ \boldsymbol{b}_z{}^0(\boldsymbol{r}) \end{bmatrix} \tag{4.33}$$

where $\boldsymbol{p}_r(\boldsymbol{r})$, $\boldsymbol{p}_z(\boldsymbol{r})$, $\boldsymbol{t}_r(\boldsymbol{r})$ and $\boldsymbol{t}_z(\boldsymbol{r})$ are the r and z components, respectively, of perpendicular and tangent unitary vectors in $\boldsymbol{r}$. With a matrix inversion, it is possible to obtain the radial and vertical components:

$$\begin{bmatrix} \boldsymbol{b}_r{}^0(\boldsymbol{r}) \\ \boldsymbol{b}_z{}^0(\boldsymbol{r}) \end{bmatrix} = \begin{bmatrix} \boldsymbol{p}_r(\boldsymbol{r}) & \boldsymbol{p}_z(\boldsymbol{r}) \\ \boldsymbol{t}_r(\boldsymbol{r}) & \boldsymbol{t}_z(\boldsymbol{r}) \end{bmatrix}^{-1} \begin{bmatrix} \boldsymbol{b}_{\perp}{}^0(\boldsymbol{r}) \\ \boldsymbol{b}_{\parallel}{}^0(\boldsymbol{r}) \end{bmatrix} \tag{4.34}$$

This method is completely independent from the total net toroidal current circulating inside the external surface of the vessel, and its knowledge is not required.

This formulation is very simple; the candidate's contribution has been the evaluation of $\boldsymbol{b}_{\perp}{}^0$ and $\boldsymbol{b}_{\parallel}{}^0$, in order to obtain the radial and vertical components of the axial-symmetric harmonic of $\boldsymbol{b}$, using (4.34). From here, it is sufficient to add the equilibrium field $\boldsymbol{B}_0$ and use (4.12) or (4.13) to calculate the total net vertical force.

Bibliography

[1] Pustovitov, V. D. (2015). General approach to the problem of disruption forces in tokamaks. Nuclear Fusion, 55(11), 113032.

[2] Mironov, D. V., & Pustovitov, V. D. (2017). Sideways force due to coupled kink modes in tokamaks. Physics of Plasmas, 24(9).

[3] Yanovskiy V. V., Iaiunese A., Pustovitov V. D., Leonov S., Havlicek J., Isernia N., Markovic T., Matveeva E., Torres A., Villone F. (2023). Magnetic measurements of disruption forces in COMPASS. Report submitted for EPS2023 conference.

BIBLIOGRAPHY

5
Model validation

T HIS chapter is focused on the parametric studies of the numerical implementation of the model described in the previous chapter.

5.1 Validation of the model

From the formulation made in the previous chapter, it appears clear that many points must be validated, and the accuracy assessed, in order to provide a reliable tool with known characteristics in terms of capabilities and precision. The following points are here treated:

- numerical implementation of (4.16) and definition of a method to assess the suitable number of harmonics;

- assessment of the numerical implementation of the FEM for the resolution of the differential equation (4.25), with the assessment of the validity of the approximation made on its boundary conditions;

- study of the impact of the reduction of the measurement points, starting from a given set of virtual diagnostics.

The results of these validations are strictly dependent on the characteristics of the field of interest. For this reason, a couple of plasma disruptions concerning the COMPASS Tokamak have been considered, using CarMa0NL simulations. The two cases differentiates because of the shape of the mesh used to simulate the COMPASS vessel on CarMa0NL, and because of the types of disruptions simulated. More details in the following.

- The first case is the simulation performed considering the mesh as in Fig. 5.1, labeling it as the *Big Hole* (BH). This is a mesh based on the real COMPASS vessel, but mostly axial-symmetric, apart from the big hole placed at the south position. Its presence is a rough modeling of real 3D components of the vessel, that trigger a 3D behavior of the current flowing into the wall during a disruption. In the following, more accurate mesh models will be introduced. The disruption considered is a Current Quench, modeled simply imposing the nullification of the plasma current at a certain instant, starting from a diverted plasma equilibrium. Then, because of the presence of the big hole, a set of $n > 0$ modes in the field, on the integration surface, is triggered. The simulation was carried out over a time span $T_s = 2$ ms, based on the typical duration of these events [1, 2]. In the initial instant the total force on the vessel is zero, since the field is in equilibrium.
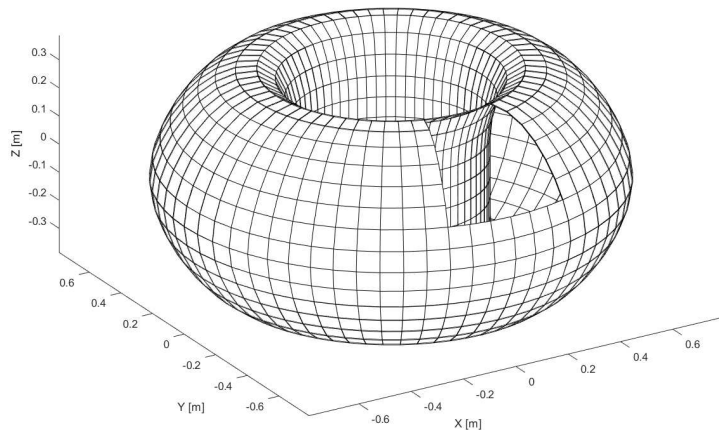
Figure 5.1: Mesh BH

- The second case is the simulation performed considering the mesh as in Fig 5.2, labeling it as the *Small Holes* (SH). This mesh has several holes on the vessel surface, and it is a more accurate model of the device vessel, since it takes into account the numerous openings. The disruption considered is a VDE, followed by a Current Quench, starting from a diverted plasma equilibrium. The simulation was carried out over a time span $T_s = 3$ ms.

For both cases, the phase of the mode $n = 1$ is evaluated using the formulation:

$$\phi_0 = \arccos\left(\frac{\overline{b_{ap}}(0)}{\max(|\overline{b_{ap}}|)}\right) \tag{5.1}$$
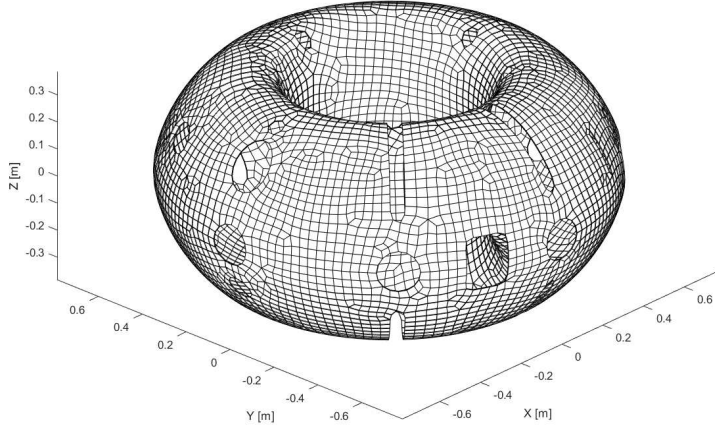
Figure 5.2: Mesh SH

where $\overline{b_{ap}}$ is the field averaged on each poloidal section, and it is a function of the toroidal angle. The data from CarMa0NL consists in:

- the value of the cartesian components of the flux density field in a set of points Σ_{20} located 20mm outside the vessel surface. These points are 28 in poloidal planes, repeated in 64 sections in toroidal direction. From these, perpendicular and tangential components are obtained;

- the value of the cartesian components of the magnetic flux density field on the sphere Σ_{sph} centered in the origin and with 1 meter of ray (spheres with bigger rays are not available, because of the presence of the external conductors);

- the sideways forces F_x and F_y and the vertical force F_z, evaluated with a numerical implementation of (4.1). For the sake of clarity, in the results, the sideways forces have been displayed using the amplitude $|F|_s$ and the phase $\underline{/F}_s$ instead of the cartesian x and y components.

If not differently specified, the simulation setup just described is used as a benchmark for the parametric analysis. Furthermore, as already said in the previous chapter, when concerning the calculation of the sideways forces, only the $n = 1$ harmonic of the perturbed field will be considered.

75

5.2 Choice of the number of harmonics of the Fourier expansion

For the choice of M_ϕ and M_θ in (4.16), a simple test has been performed. The expansion has been applied on the perpendicular and tangential components, and then the result has been compared with the same field used for the expansion evaluation. The error parameter used is a percentage Normalized Root Mean Square Error (NRMSE), defined as follows:

$$NRMSE(t) = \sqrt{\frac{\overline{(b_{Fou}^{(nor,tan)} - b_{ref}^{(nor,tan)})^2}}{\max\left[abs(b_{ref}^{(nor,tan)})\right]}} \cdot 100\% \qquad (5.2)$$

where $b_{Fou}^{(nor,tan)}$ and $b_{ref}^{(nor,tan)}$ are, respectively, the Fourier and the reference perturbed perpendicular or tangential field, and the average operation (the ‾ symbol at the numerator in (5.2)) has been performed on all the points of the integration surface, so as the max operation. The error defined in (5.2) is a function of time.

For the sake of simplicity, the toroidal harmonic has been fixed to a maximum value of one. The results are shown in the following Figs. 5.3, 5.4 and Tabs. 5.1 and 5.2. In the tables, the error displayed is obtained from another average, performed in time. For the analysis in the next section, the number of poloidal harmonics has been fixed to 6.

Poloidal harmonic order	1	2	3	4	5	6
Mesh BH	36.1%	22.0%	7.7%	7.2%	6.0%	5.4%
Mesh SH	24.6%	17.7%	11.9%	10.5%	9.1%	8.1%

Table 5.1: Fourier NRMSE on the perpendicular component of the perturbed field

Poloidal harmonic order	1	2	3	4	5	6
Mesh BH	15.4%	5.3%	4.0%	2.2%	2.1%	2.0%
Mesh SH	21.7%	11.9%	8.4%	7.2%	6.5%	6.1%

Table 5.2: Fourier NRMSE on the tangent component of the perturbed field

a)

b)
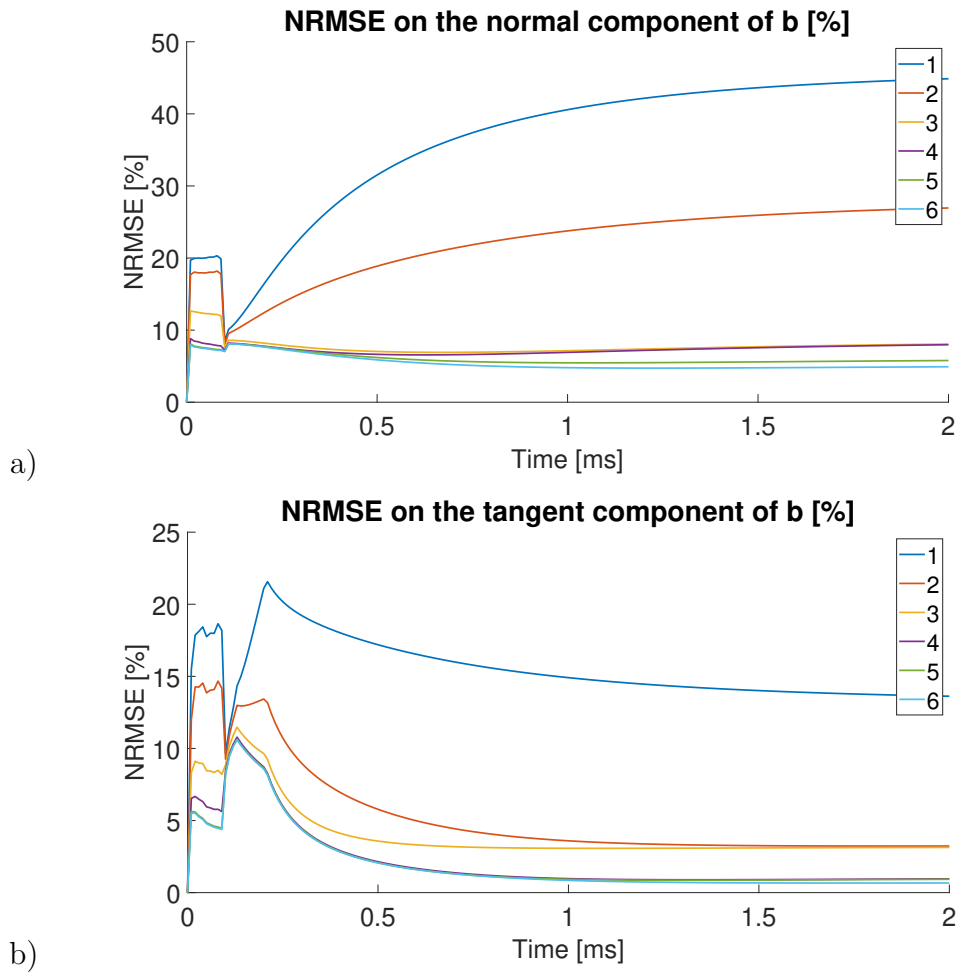
Figure 5.3: Fourier NRMSE on the a) perpendicular (normal) and b) tangent components of the perturbed field, mesh BH
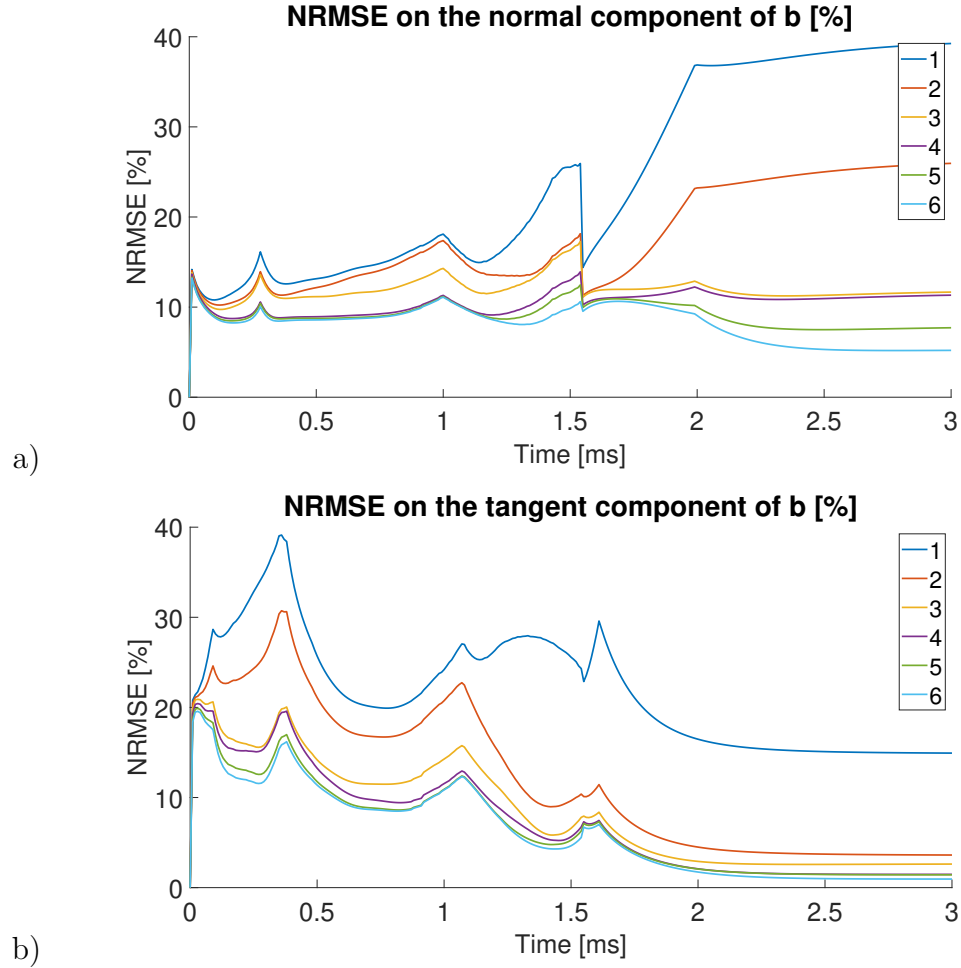
Figure 5.4: Fourier NRMSE on the a) perpendicular (normal) and b) tangent components of the perturbed field, mesh SH

5.3 Choice of the differential equation's parameters

Another test is performed on the choice of the parameters influencing directly the solution of the numerical implementation of the differential equation (4.25). These are basically the dimensions of the triangles of the mesh, in terms of maximum length of triangles' sides h_{max}, and the ray ρ_D of the semicircle where the null Dirichlet boundary conditions are imposed. Another point to clarify is the imposition of the null Neumann conditions on the z

axis. This aspect will be treated at the end of the paragraph. For simplicity, this test has been performed only in the case of the BH mesh.

In order to study the impacts of h_{max} and ρ_D, the following analysis has been performed. Based on the previous analysis on the number of Fourier harmonics expansion, $M_\theta = 6$ and $N_\phi = 1$ have been fixed. Then, the error of the field obtained from the differential equation on the validation sphere Σ_{val}, with ray 1 m, has been compared with the reference field from CarMa0NL simulation, changing the values of h_{max} and ρ_D. The dimension of the validation sphere has been chosen considering the limits of the simulation performed with CarMa0NL that provides the field. In fact, spheres of greater dimension are not available, because there would be an intersection with the active coils of the device, and the field evaluated by the tool is not reliable. Anyway, it is important to remember that the field of interest is only the one on the external surface of the vessel, where the Neumann boundary conditions obtained by the measurements (real or virtual) are imposed. The analysis here performed is useful only to confirm the reliability of the numerical implementation, and to establish a criterion for the choice of the differential equation's parameters. The percentage error, for the radial component of the field, is so defined:

$$e_{r_{\Sigma_{val}}}(t) = \overline{\left(\frac{abs(b_{r_{DE}}^{n=1} - b_{r_{ref}}^{n=1})}{\max_{\Sigma_{val}} \left(b_{r_{ref}}^{n=1} \right)} \right)} \cdot 100\% \tag{5.3}$$

where $b_{r_{DE}}^{n=1}$ and $b_{r_{ref}}^{n=1}$ are the values of the radial component of the $n=1$ harmonic of the perturbed field on Σ_{val} provided by the differential equation and CarMa0NL respectively, $\max_{\Sigma_{val}} \left(b_{r_{ref}}^{n=1} \right)$ is the maximum CarMa0NL field on Σ_{val}, and the $(\bar{\cdot})$ symbol represents an average operation performed on all the points of the sphere. This error is dependent on time. Similar errors $e_{\phi_{\Sigma_{val}}}$ and $e_{z_{\Sigma_{val}}}$ have been calculated for the toroidal and vertical components. The results of the parametric analysis are shown in Fig. 5.5, only for the case with $h_{max} = 0.05$ m, because this parameter has a very little impact, at least with the values considered. For the radial and toroidal components, excluding the case $\rho_D = 1.1$ m, the error is pretty similar for all the other cases examined. For the vertical component, also the case $\rho_D = 1.1$ m is similar to the others. The behavior is quite general, with the maximum error in the initial instants, when the perturbed field is lower, and then it decreases over time. For the following analysis, if not differently stated, the values of $\rho_D = 2$ m and $h_{max} = 0.05$ m will be used.
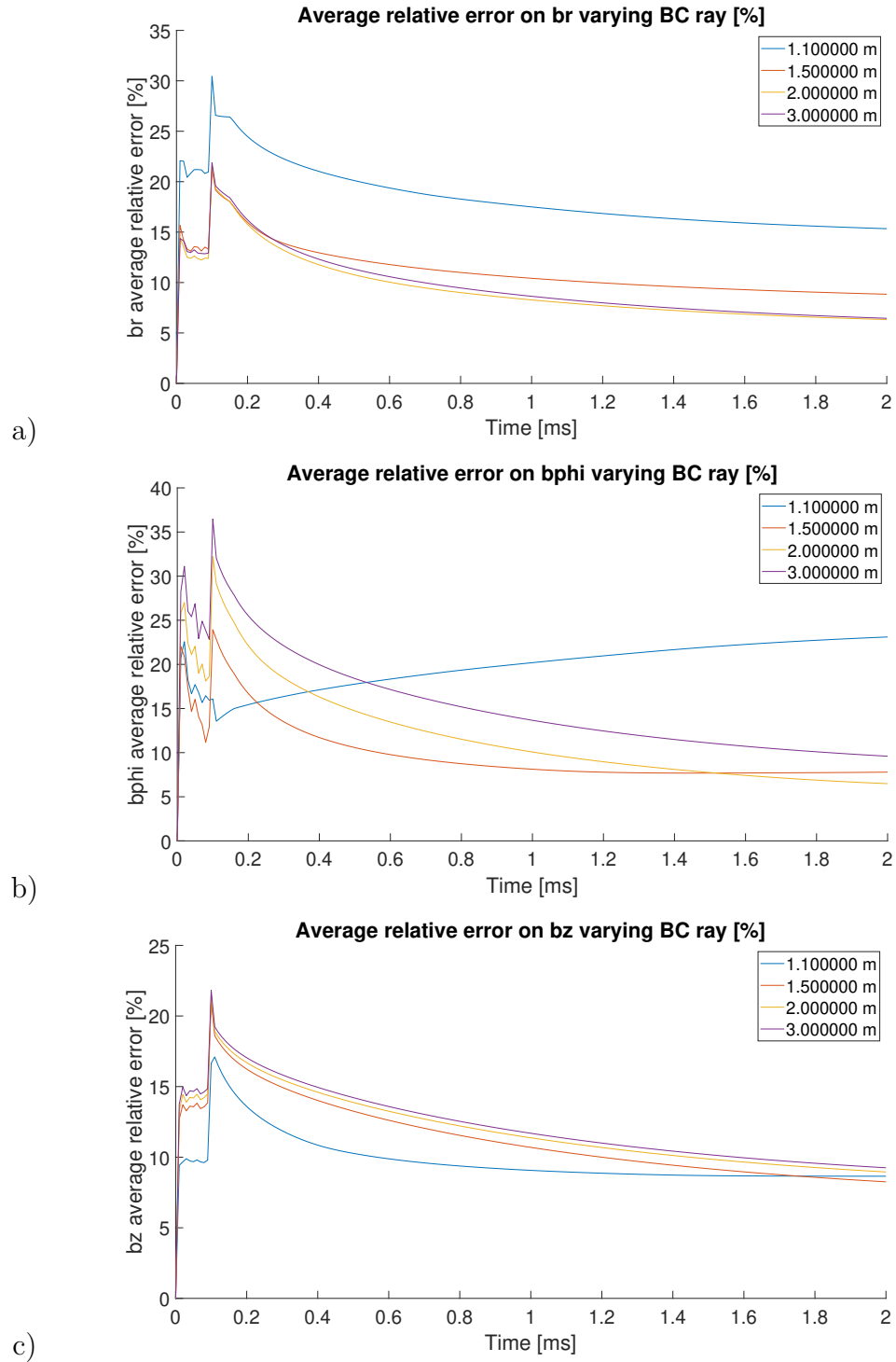
a)

b)

c)

Figure 5.5: $e_{r_{\Sigma_{val}}}(t)$ on the a) radial, b) toroidal and c) vertical components of the field, $h_{max} = 0.05$m, mesh BH

For the null Neumann B.C. on the vertical z-axis, the entity of the approximation has been evaluated comparing the mean absolute value of the $n = 1$ harmonic of the perturbed radial field on the axis with the same value on the vessel surface. The ratio between the two is below 1%. Then, the field on the axis has been considered negligible.

5.4 Number of points for the Neumann B.C. on the vessel surface

Another parameter is the choice of the number of points N_{Neu} on the vessel surface where to impose the Neumann B.C. This number is independent from the number of measurement points, and is in fact arbitrary. The analysis has been performed fixing the parameters already discussed, and changing the number of points along both θ (N_{Neu}^{θ}) and ϕ (N_{Neu}^{ϕ}) directions on the surface. For simplicity, these two numbers are kept the same. The error parameter is evaluated directly on the force. The amplitude $|F|_s$ and phase $\angle F_s$ of the sideways component obtained with the method here presented has been compared with the force evaluated by CarMa0NL, using a NRMSE, similarly to the analysis of the Fourier expansion on the field. In this case, the average is performed in time, because the force is a global parameter. This analysis involves only the differential equation, then the vertical force is not affected. The results in Tab. 5.3 show that the use of $N_{Neu}^{\theta} = N_{Neu}^{\phi} = 100$, which means $N_{Neu} = 10000$, is enough to obtain a stable result in the force error.

N_{Neu}^{θ} (N_{Neu}^{ϕ})	$|F|_s$		$\angle F_s$	
	Mesh BH	**Mesh SH**	**Mesh BH**	**Mesh SH**
25	12.3%	8.1%	3.4%	7.6%
50	9.1%	7.7%	1.3%	8.1%
100	6.4%	6.2%	1.3%	7.8%
200	6.3%	6.2%	1.3%	7.8%

Table 5.3: B.C. Neumann NRMSE error on the sideways forces

5.5 Reduction of the number of points of virtual measurements

In order to approach a more realistic case with the CarMa0NL simulations, the number of virtual diagnostics has been reduced, to be more similar to

the real distribution of the saddle coils measurements on the COMPASS
vessel. The original set of virtual measurements, here repeated for clarity, is
a set of 28 points equally distributed poloidally, reproduced on 64 sections.
In order to study what happens if the number of virtual diagnostics points
is reduced, the original grid of 28 x 64 points has been modified, decreasing
progressively the number of sections (considering 64, 32, 16, 8 and 4 sections)
and the number of points on each one (considering 28 and 14 points). Let's
remember that COMPASS is equipped with 24 saddles, unevenly distributed
on the poloidal section, repeated on 4 sections, for a total of 104 saddles, of
which 76 are effectively working. For this reason, the case with 14 poloidal
points on 4 sections is the most "realistic" one. The error on the force, used
in the previous section, has been used again. The results are shown in Tab.
5.4. It appears clear that, especially in the case with the mesh SH, in the
case with 4 sections the error is much greater than the error obtained with 8
sections. From 16 sections, the results remain very similar. In order to give
a graphical view of the worsening of the accuracy, as an example, the two
extreme cases, with 28 poloidal points on 64 sections and 14 poloidal points
on 4 sections, for meshes BH and SH, are shown in Figs. 5.6, 5.7, 5.8 and
5.9.

Number of sections		4	8	16	32	64
Force NRMSE	$\lvert F \rvert_s$	14.1%	6.4%	5.5%	4.8%	4.8%
(14 theta points)	$\angle F_s$	0.6%	0.3%	1.7%	1.4%	1.4%
BH	F_z	18.9%	9.0%	13.3%	13.0%	13.0%
Force NRMSE	$\lvert F \rvert_s$	10.9%	8.0%	7.0%	6.4%	6.4%
(28 theta points)	$\angle F_s$	0.8%	0.3%	1.6%	1.3%	1.3%
BH	F_z	9.0%	3.2%	2.6%	2.7%	2.7%
Force NRMSE	$\lvert F \rvert_s$	23.8%	12.5%	6.4%	6.5%	6.3%
(14 theta points)	$\angle F_s$	17.2%	11.0%	8.3%	8.4%	8.4%
SH	F_z	10.2%	8.7%	3.4%	2.2%	2.2%
Force NRMSE	$\lvert F \rvert_s$	28.4%	12.1%	6.0%	6.3%	6.2%
(28 theta points)	$\angle F_s$	17.3%	11.9%	8.6%	8.0%	7.8%
SH	F_z	7.2%	6.8%	2.7%	1.8%	1.7%

Table 5.4: Force NRMSE on the forces components, changing the number of
virtual diagnostics points
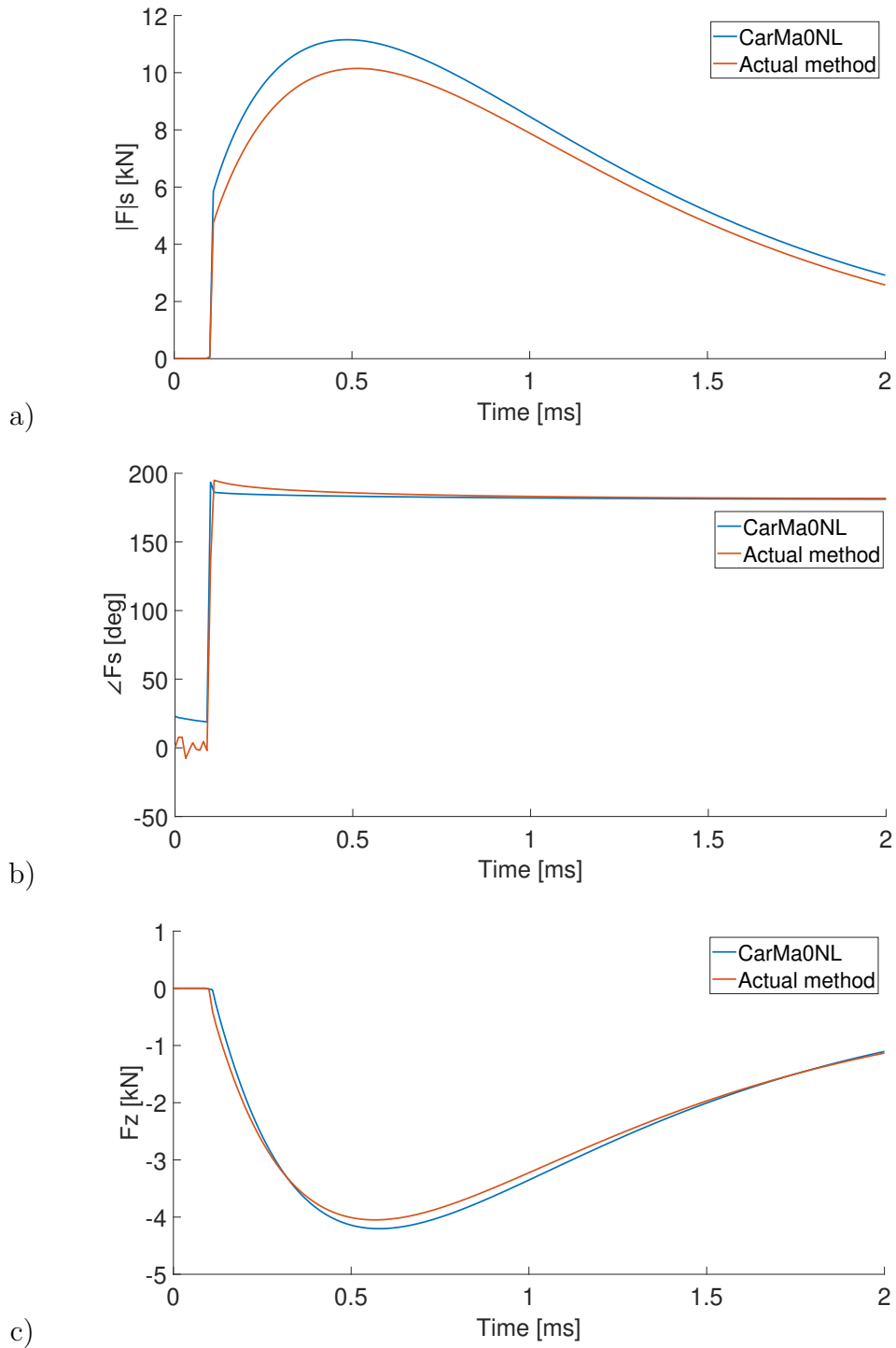
Figure 5.6: a) $|F|_s$, b) $\angle F_s$ and c) F_z, using 28 poloidal points on 64 sections, in the case with mesh BH
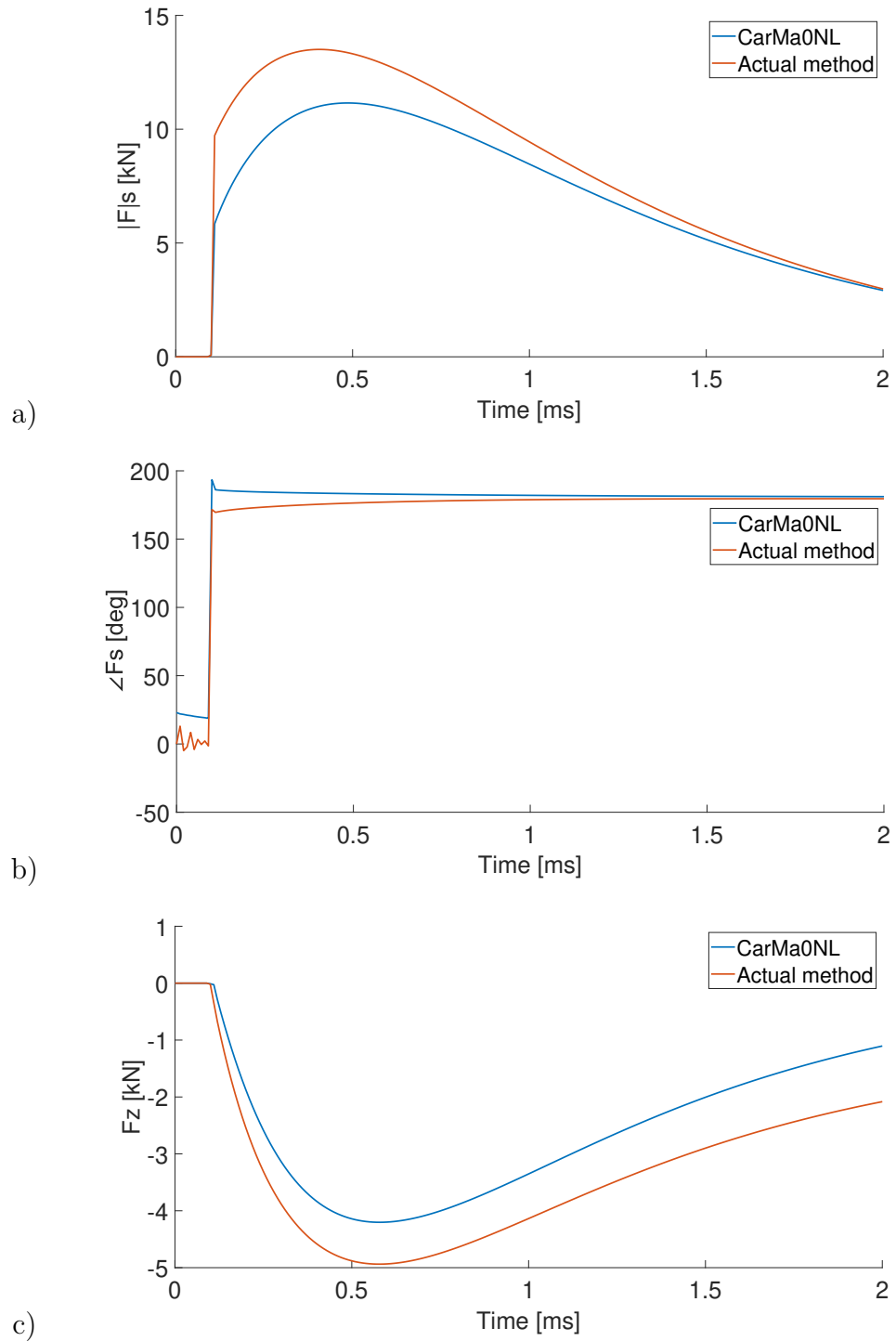
Figure 5.7: a) $|F|_s$, b) $\angle F_s$ and c) F_z, using 14 poloidal points on 4 sections,
in the case with mesh BH

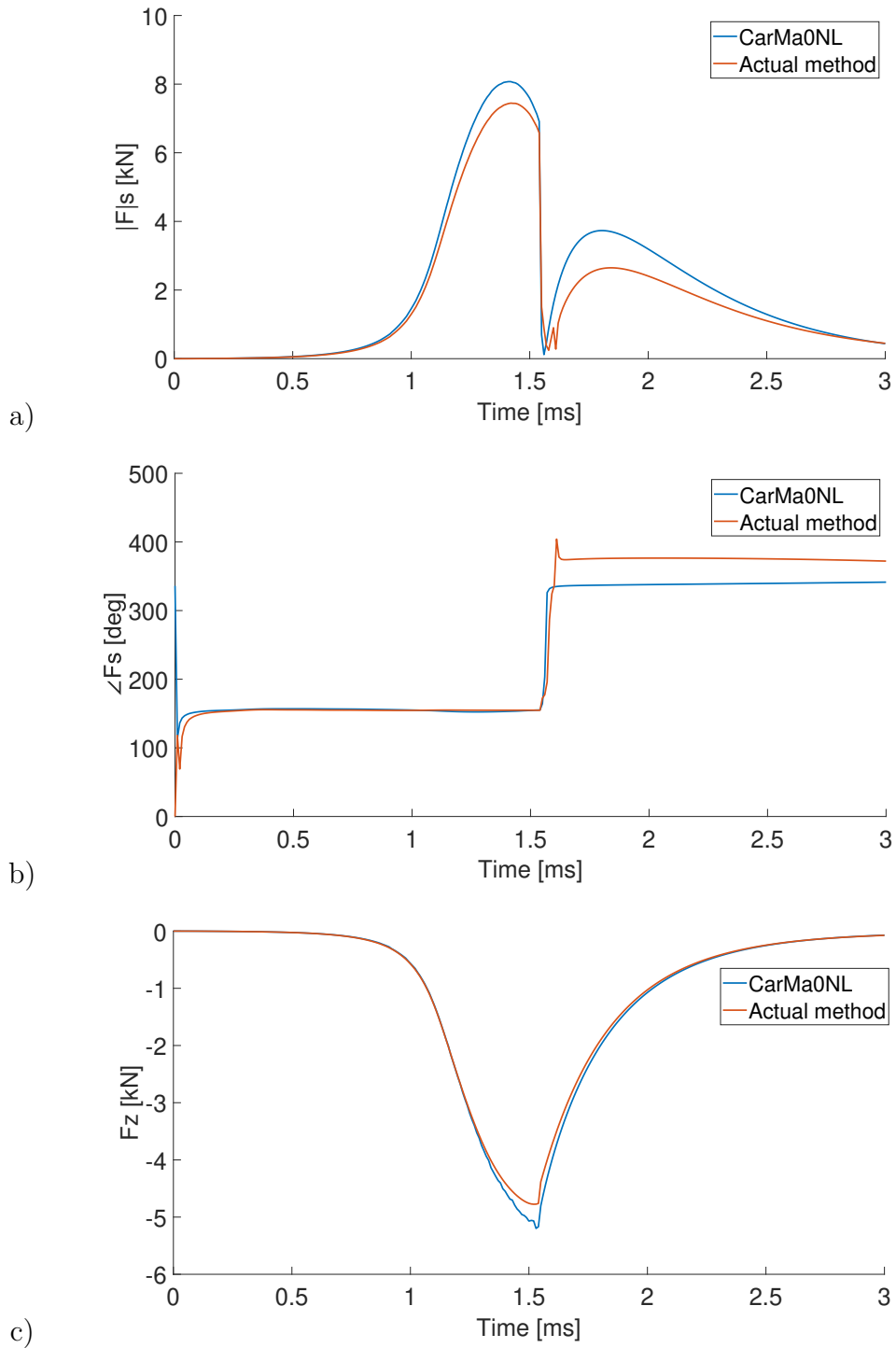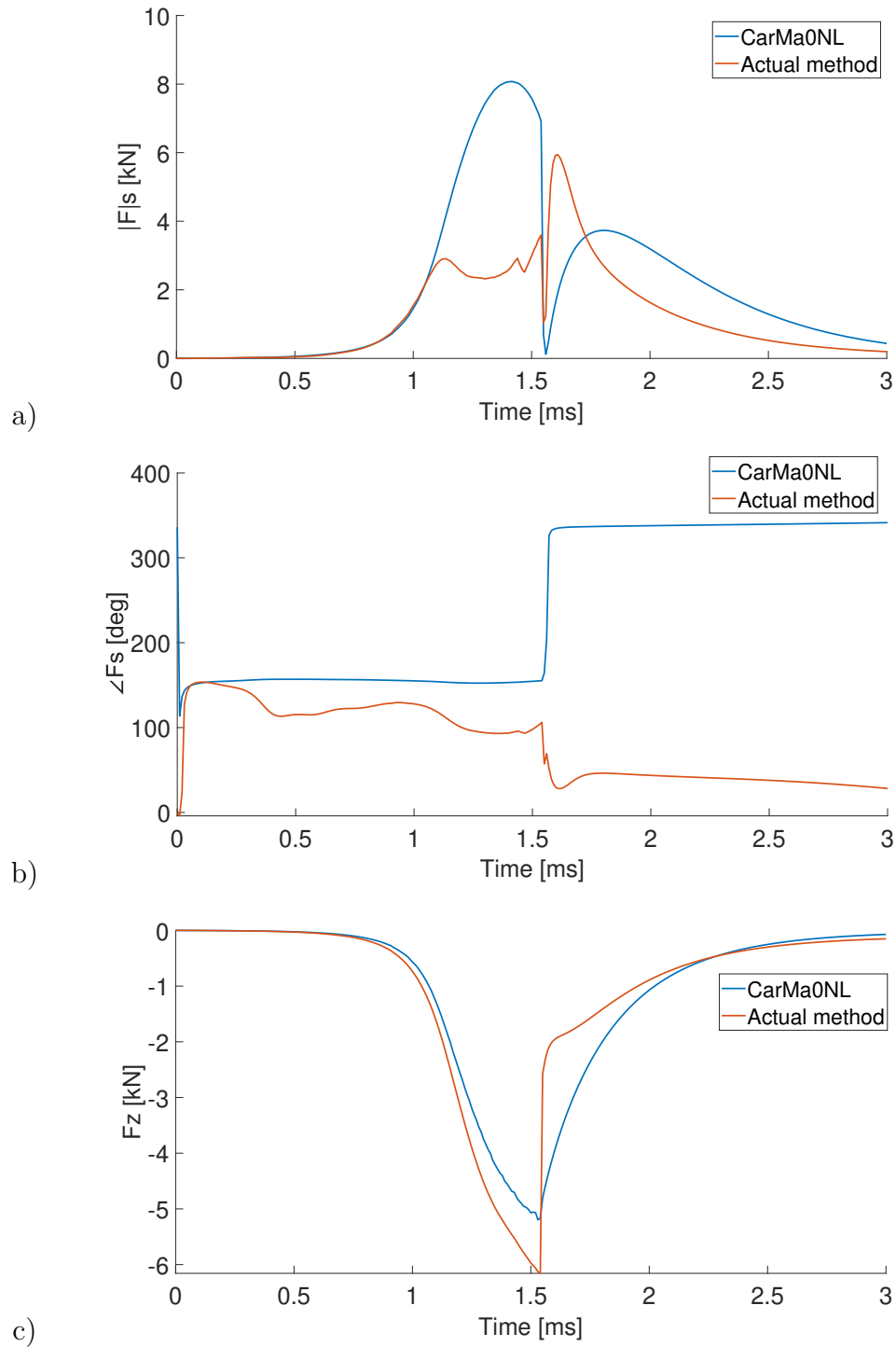Figure 5.8: a) $|F|_s$, b) $\angle F_s$ and c) F_z, using 28 poloidal points on 64 sections, in the case with mesh SH

Figure 5.9: a) $|F|_s$, b) $\angle F_s$ and c) F_z, using 14 poloidal points on 4 sections, in the case with mesh SH

These results suggest that, when the mesh has more openings distributed on its surface, the use of 4 sections strongly reduces the results accuracy.

This is a first step to link the simulation with the real measurements. Another test, concerning a much complex set of virtual diagnostics points, is described in the next chapter.

With the parameters set to the previously shown values, the computational time is approximately of 1 second per analyzed instant. The hardware on which the calculations were performed uses a CPU 11th Gen Intel(R) Core(TM) i7-1165G7 @ 2.80GHz. The mesh used for the numerical solution of the differential equation uses 3078 nodes and 5850 elements (Fig. 5.10).
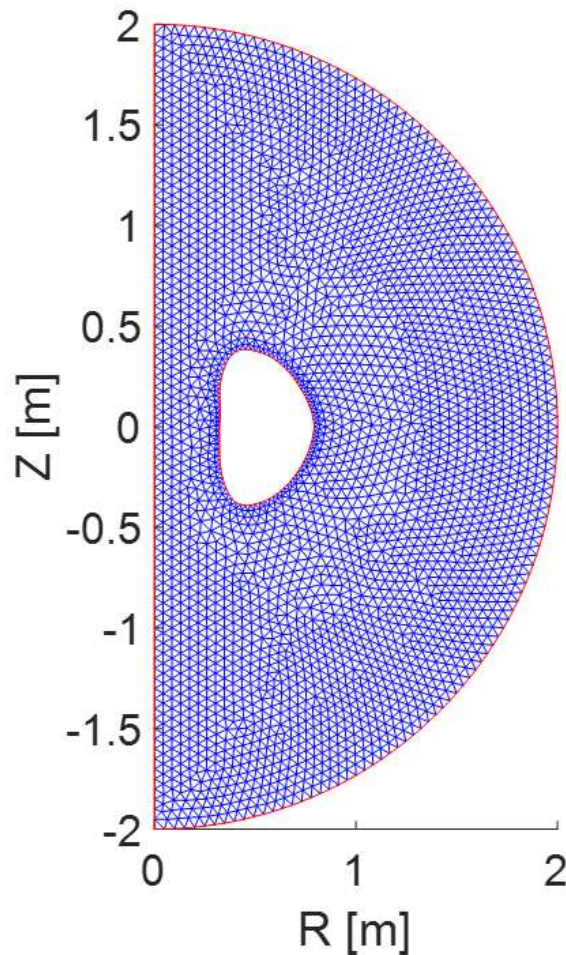
Figure 5.10: Mesh used for the differential equation numerical solution

Bibliography

[1] Villone, F., Barbato, L., Mastrostefano, S., & Ventre, S. (2013). Coupling of nonlinear axisymmetric plasma evolution with three-dimensional volumetric conductors. Plasma Physics and Controlled Fusion, 55(9), 095008.

[2] Gerasimov, S. N., Abreu, P., Baruzzo, M., Drozdov, V., Dvornova, A., Havlicek, J., ... & Contributors, J. E. T. (2015). JET and COMPASS asymmetrical disruptions. Nuclear Fusion, 55(11), 113006.

6
Results

This chapter contains the results obtained by the method, using a more advanced set of simulation data and the real diagnostics data obtained from the COMPASS magnetic diagnostics.

6.1 Use of a set of points similar to the COMPASS saddle distribution

Before to consider the real diagnostics data, a further analysis involving a CarMa0NL simulation has been performed. In this section, the forces have been calculated using the set of points shown in Figs. 6.1 for the saddle loops.
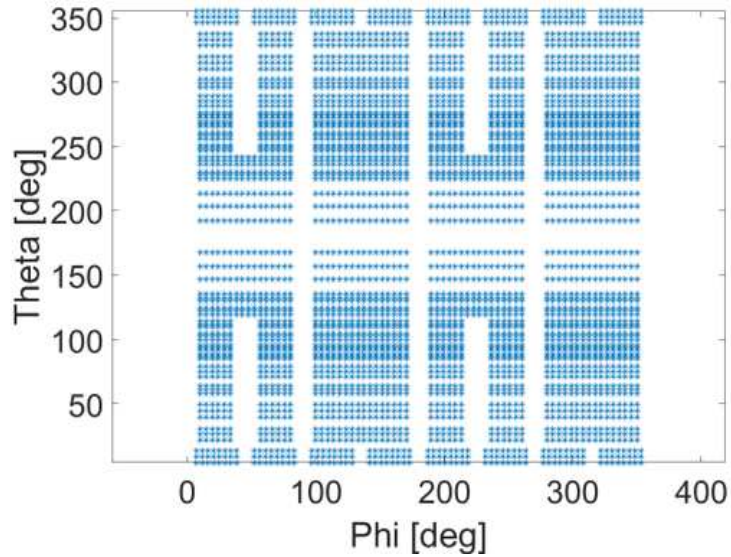
Figure 6.1: Set of points used to reproduce the saddle loops

This set has been created considering the real shape of the COMPASS
saddle coils (Fig. 6.2, where the position south, north, west and east of the
saddle is highlighted) and trying to reproduce it.
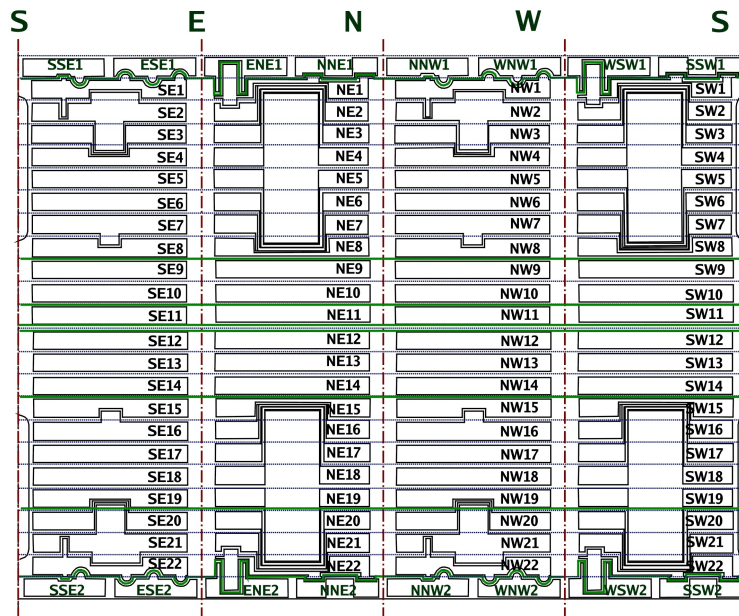
Figure 6.2: Saddle loops set of COMPASS device [1]

For the EPRs (the External Partial Rogowski coils, introduced in Ch. 2),

a set of points reproducing the real positions has been used, and is shown, along with the real and working saddle loops positions, in Figs. 6.3, 6.4 and 6.5.
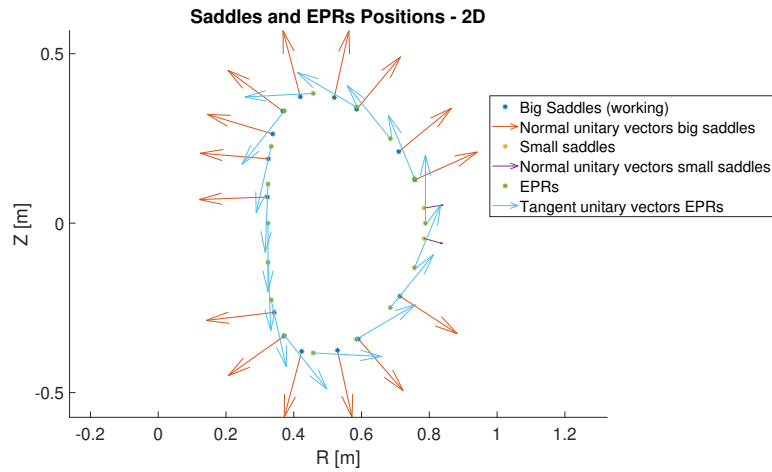
Figure 6.3: Positions of saddle loops and EPRs, 2D view
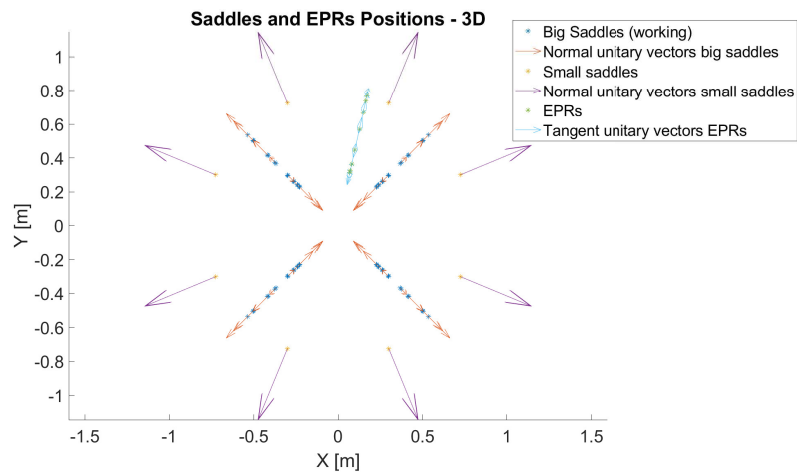
Figure 6.4: Positions of saddle loops and EPRs, 3D X-Y view

93

Figure 6.5: Positions of saddle loops and EPRs, 3D view

The perpendicular and tangential components of the perturbed field from
the tool CarMa0NL have been calculated and then used to evaluate the force,
respectively on the set of virtual saddle loops and EPRs, performing all the
steps already described.

It is important here to notice that the set of points is unevenly distributed
on the surface. This can led to problems concerning the Fourier approxima-
tion; in order to avoid this, a preliminary linear interpolation of the scattered
field data has been performed on a set of points evenly distributed, and these
points were used for the expansion. This approach is an important issue, and
the linear interpolation is just the easiest way to address the problem. Other
possible solutions are under study.

The simulations analyzed are the same of the previous cases, with meshes
BH and SH. The results, in terms of error with the CarMa0NL force, are
shown in Figs. 6.6 and 6.7. They are pretty similar to those obtained in the
previous chapter when 4 sections of points are used, especially in the case of
the mesh SH. In particular, it is clearly visible an error of a factor two, ap-
proximately, on the peak value of the amplitude of the sideways forces. This
suggest, again, that the set of saddle coils on COMPASS may be too rough
to be used efficiently in this method. In spite of this, it is encouraging to
observe that the shape of the amplitude of the sideways forces is reproduced
with good fidelity, along with the instant of the peak. In addition, the error
on the phase and on the vertical force are lower. For this reasons, the use
of the method makes sense, at least to understand the change of direction of
the sideways forces during the disruption, and to have a suggestion, in terms
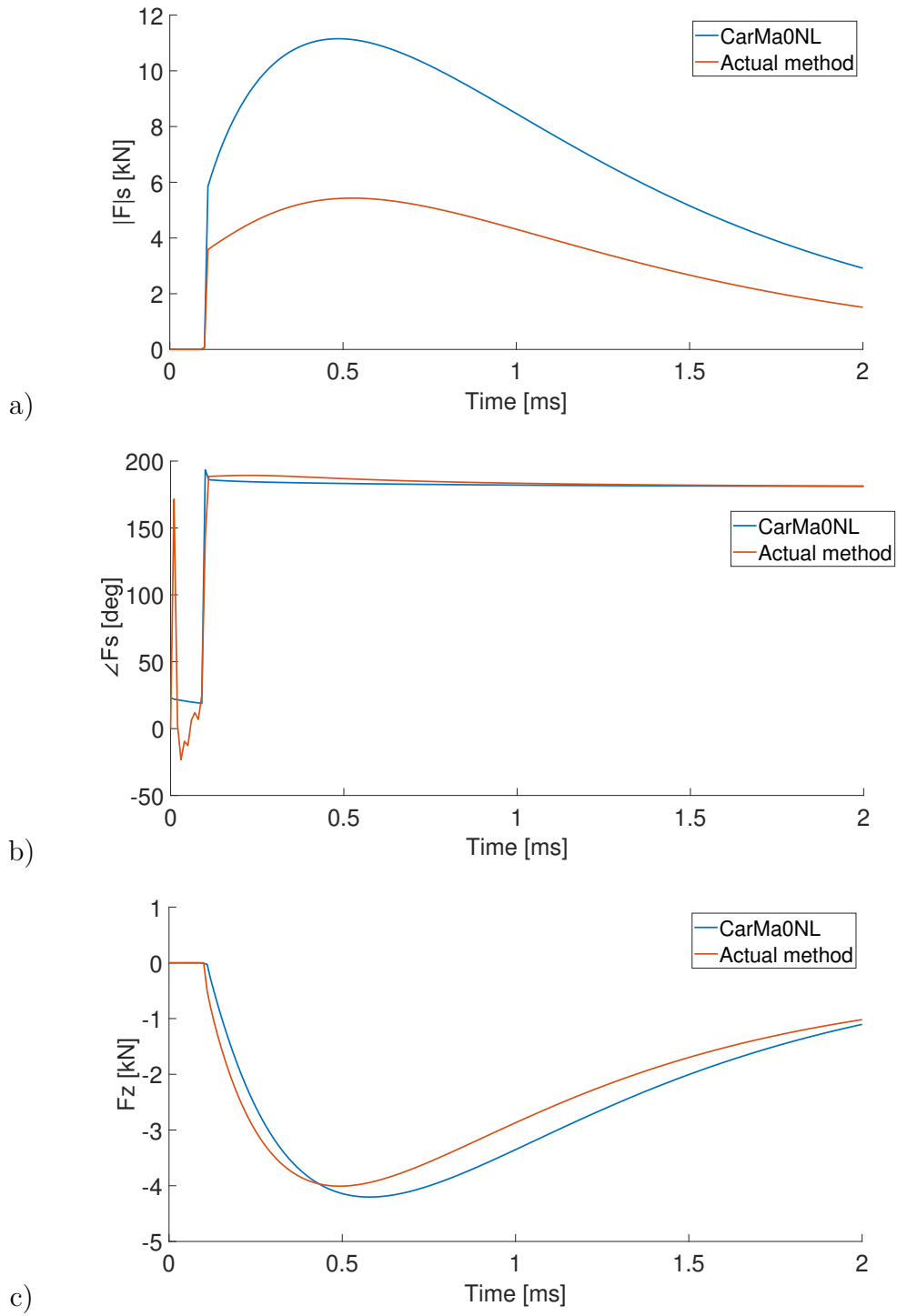of order of magnitude, in its peak value.

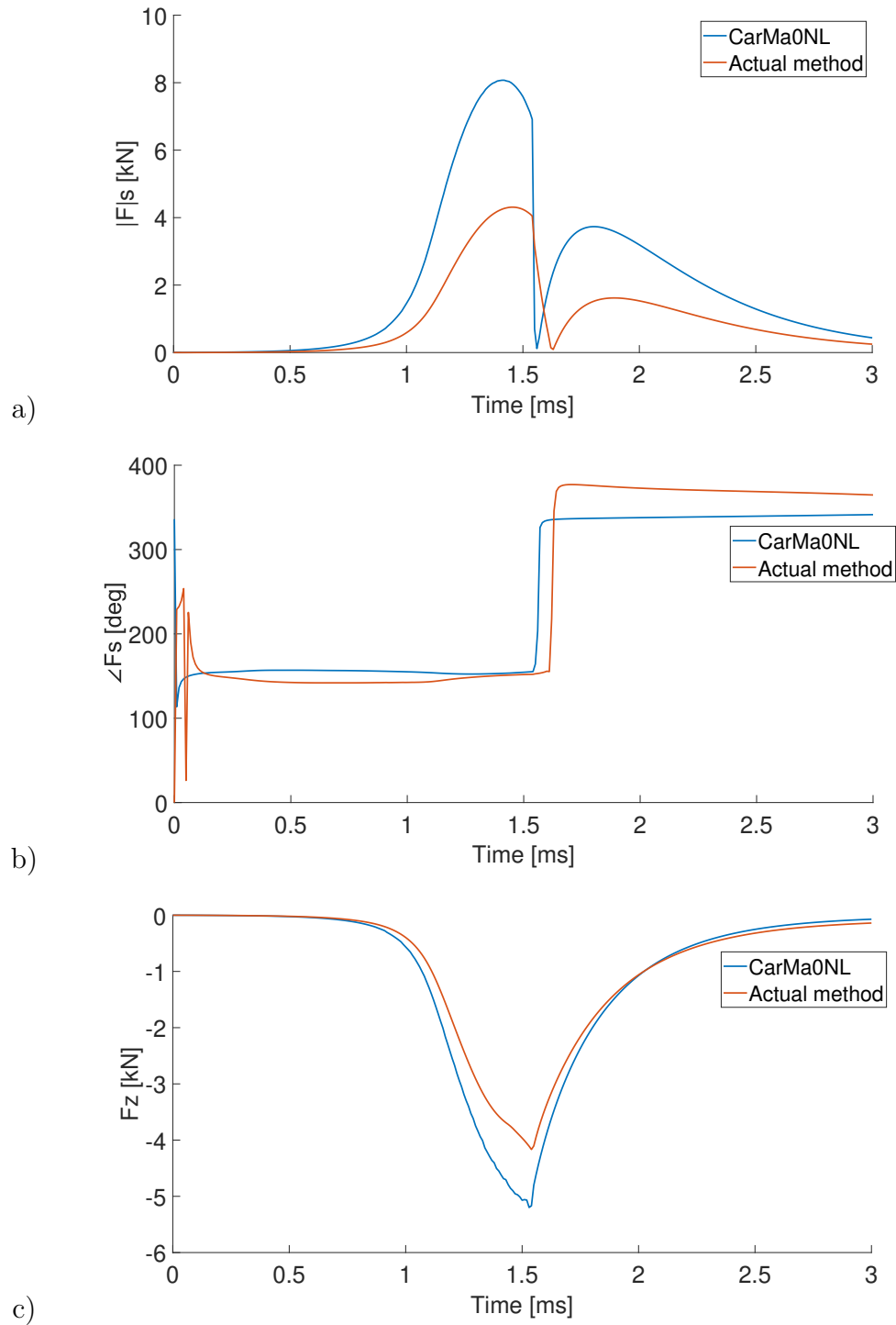Figure 6.6: a) $|F|_s$, b) $\underline{/F}_s$ and c) F_z in the case with mesh BH

Figure 6.7: a) $|F|_s$, b) $\angle F_s$ and c) F_z in the case with mesh SH

6.2 Application on COMPASS shots

The method here presented, without significant variations, has been applied in case of a real shot on the COMPASS device, along with a third CarMa0NL simulation with a different mesh for the vessel, the Protruding Mesh (PM) shown in Fig. 6.8. Differently from the meshes BH and SH, this mesh is
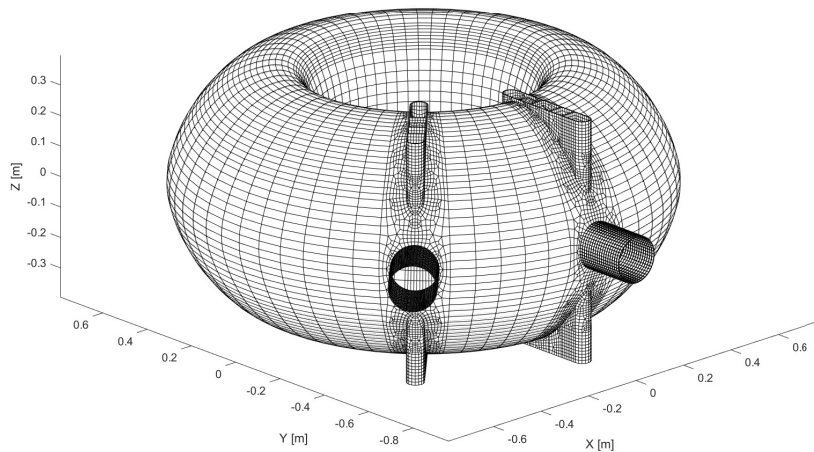

Figure 6.8: Mesh PM

equipped with 3D components that protrude from the surface, and it is the most realistic, among the three meshes here shown, if compared with the real shape of the COMPASS vessel. The disruption characteristics are the same of the SH case. This simulation has been designed with the idea to reproduce in the most faithful way possible a true disruption of COMPASS.

The only difference between the simulations and the measurements is the way to obtain the field. In the case of the simulations, both equilibrium field B_0 and perturbed field b are given by the simulation itself. Instead, from the measurements, the equilibrium field is provided by the EFIT tool, already described, and the perturbed field from the saddle loops and the EPR coils. It is important here to point out how these diagnostics were used.

The physical quantity measured by the saddle loops and the EPRs is the voltage induced during the operation phase of the device. Then, the field can be obtained directly from the Faraday-Neumann-Lenz law, with the hypothesis that the perpendicular field is uniform on the coil surface,

97

performing a numerical time integration, the cumulative sum of the voltage value at every instant, multiplied by the time step, 0.5 μs in the case of the COMPASS saddle loops and EPR coils, and divided by the area of each saddle or coil. Obviously, this formula requires the definition of an initial time instant, when the integration starts. This instant has been fixed as the initial instant of the disruption, which is easily guessable from the measurements. In this way, the field obtained is directly the perturbed perpendicular or tangent field, that can be used to evaluate the forces, as previously seen: the perpendicular $n = 1$ component becomes the Neumann B.C. for the differential equation used for the sideways forces, while the tangent axial-symmetric component, along with the perpendicular one, is used for the calculation of the vertical force.

Made this clarification, the forces are evaluated exactly as seen previously. Differently from the case when CarMa0NL is used, where the applications are limited to the possible simulations that can be made, here several hundreds of shots with proper and interesting disruptions are available. Unfortunately, for the saddle loops, a problem of voltage saturation is present when a disruption happens in presence of the maximum plasma current. This limits the analysis only to shots with a lower plasma current, which are still of interest.

As a first example, a shot very similar to the one simulated with the mesh PM has been studied. The instant of the disruption in the simulation has been taken coincident with the same instant in the simulation. Let's recall the results in Figs. 6.6 and 6.7, obtained previously using a set of virtual diagnostics similar to the real saddle loops. In that case, as already said, it is visible an error approximately of a factor two between the sideways forces from CarMa0NL and the sideways forces of the actual method. The same operation has been performed on the PM mesh. The comparison between the CarMa0NL forces, the forces obtained from the simulation with the virtual measurements points distributed as in Fig. 6.1, and the forces obtained with the real measurements are shown in Fig. 6.9. The shot analyzed is the #20829 in the COMPASS database.

It is quite interesting to observe that the forces obtained from the measurements are very similar, with a certain degree of approximation, to the forces obtained from the virtual diagnostics, and both have an error of a factor of two circa with the CarMa0NL sideways forces' amplitude. An additional observation is that, at the end of discharge, the forces do not reduce to zero, but seems to saturate to a constant value. This behaviour appears only when the real measurements are used, and the reasons are still under study.

In the following, other disruptions from COMPASS have been analyzed. The forces evaluated by the method are shown from Fig. 6.10 to 6.14. All

these shots are very similar, in terms of plasma parameters and disruption phenomena, to the shot # 20829 used as a reference. For example, shot # 20827 is identical, and also the shot # 20828 has similar forces values, with the difference of the initial time of the disruption. Shots # 20558, # 20561 and # 20562 are similar to each other, apart from the initial and final instants.
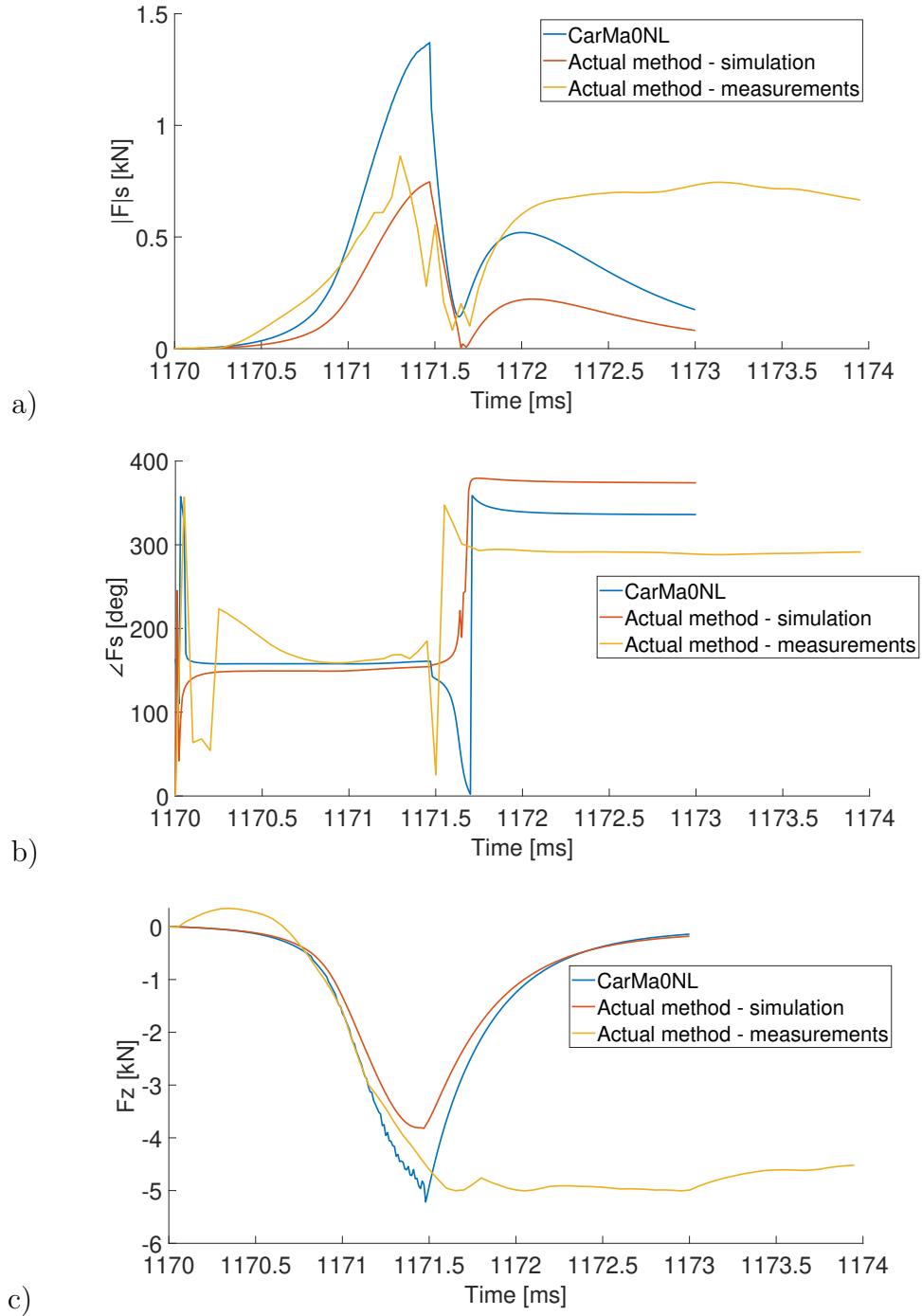
Figure 6.9: Comparison on a) $|F|_s$, b) $\underline{/F_s}$ and c) F_z in the case with mesh PM, between the results on CarMa0NL, the results of our method with the simulations data, and the diagnostics data from shot # 20829
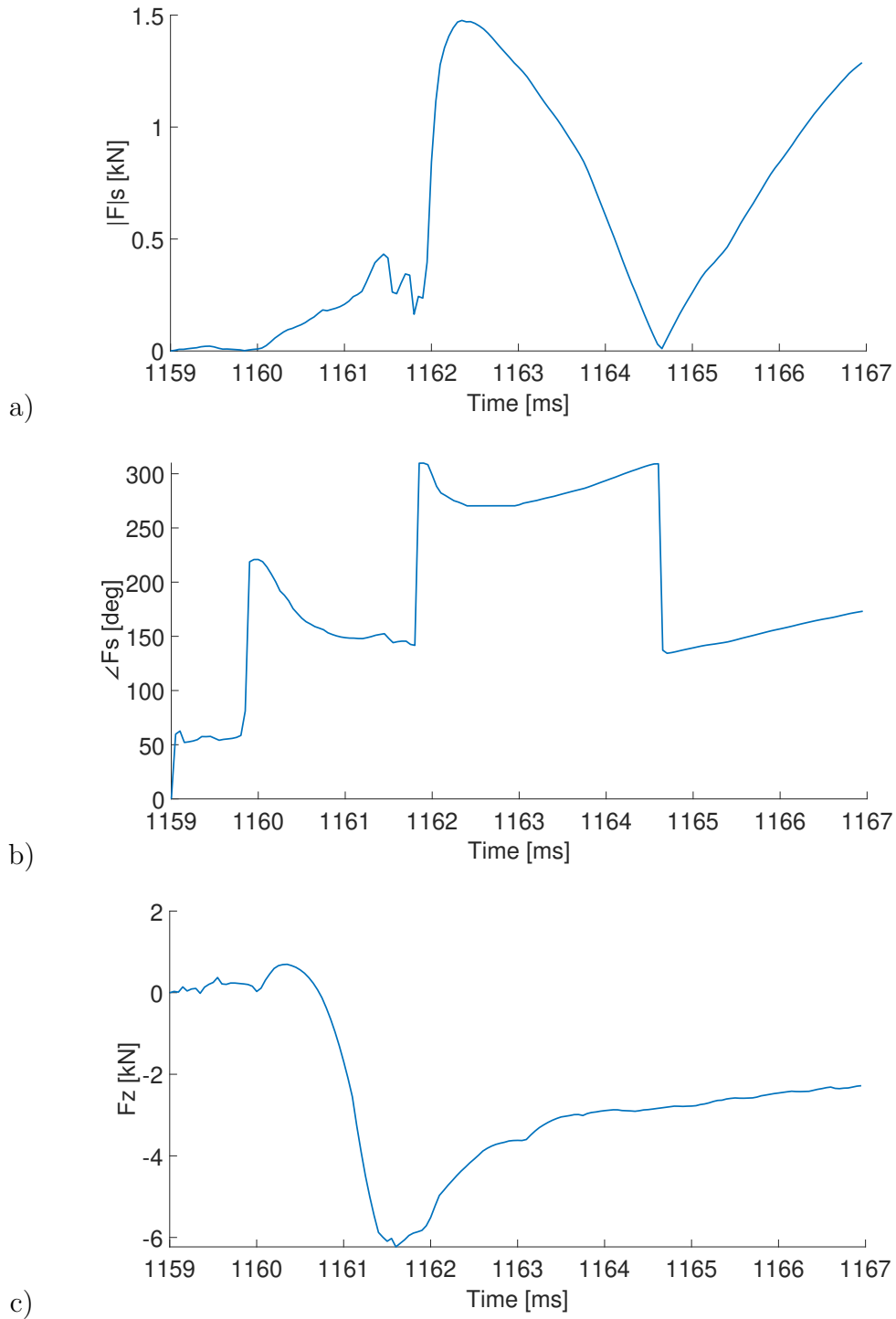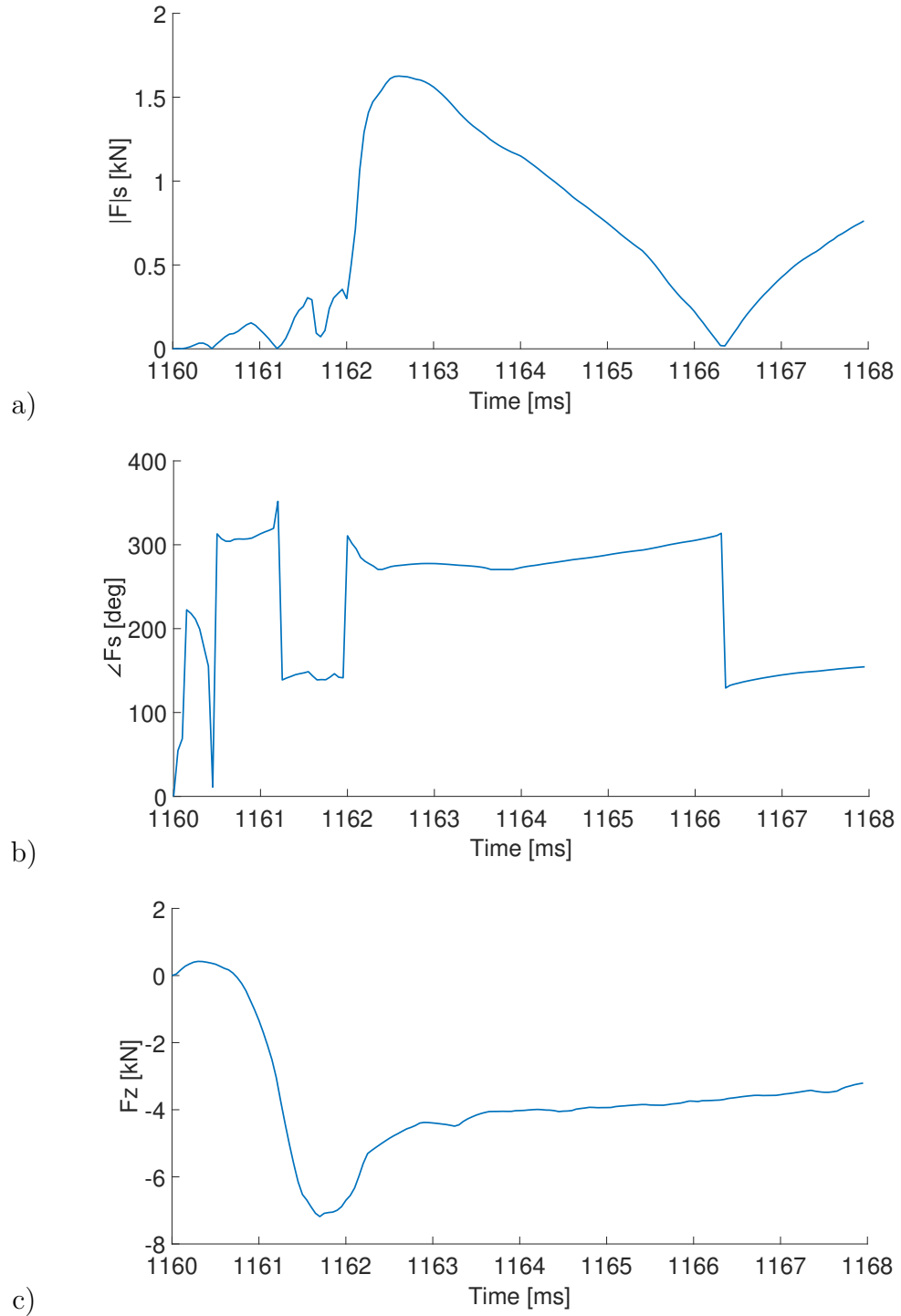
a)

b)

c)

Figure 6.10: a) $|F|_s$, b) $\underline{\angle F}_s$ and c) F_z obtained from the diagnostics data of the shot # 20558

101

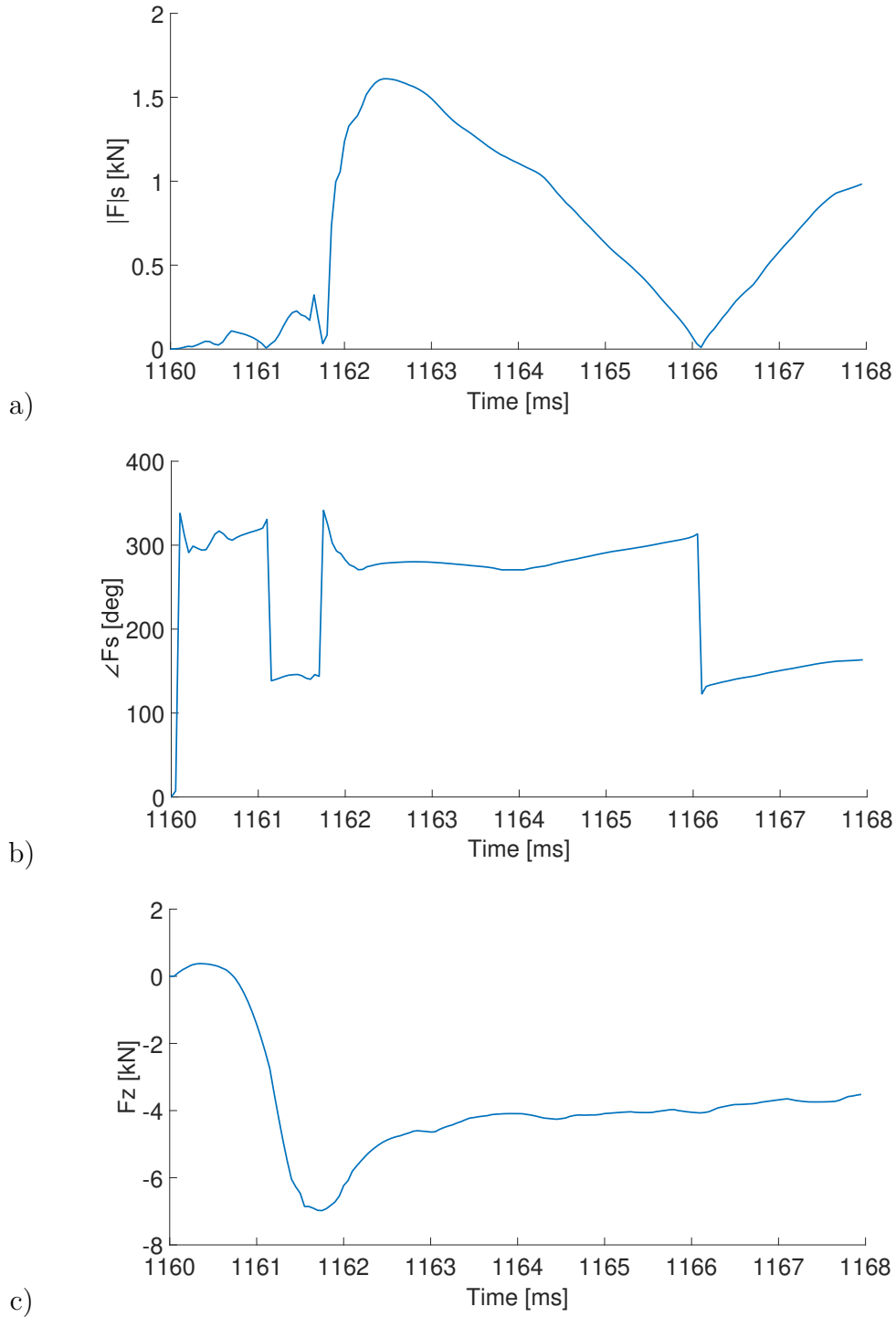Figure 6.11: a) $|F|_s$, b) $\angle F_s$ and c) F_z obtained from the diagnostics data of the shot # 20561

Figure 6.12: a) $|F|_s$, b) $\angle F_s$ and c) F_z obtained from the diagnostics data of the shot # 20562
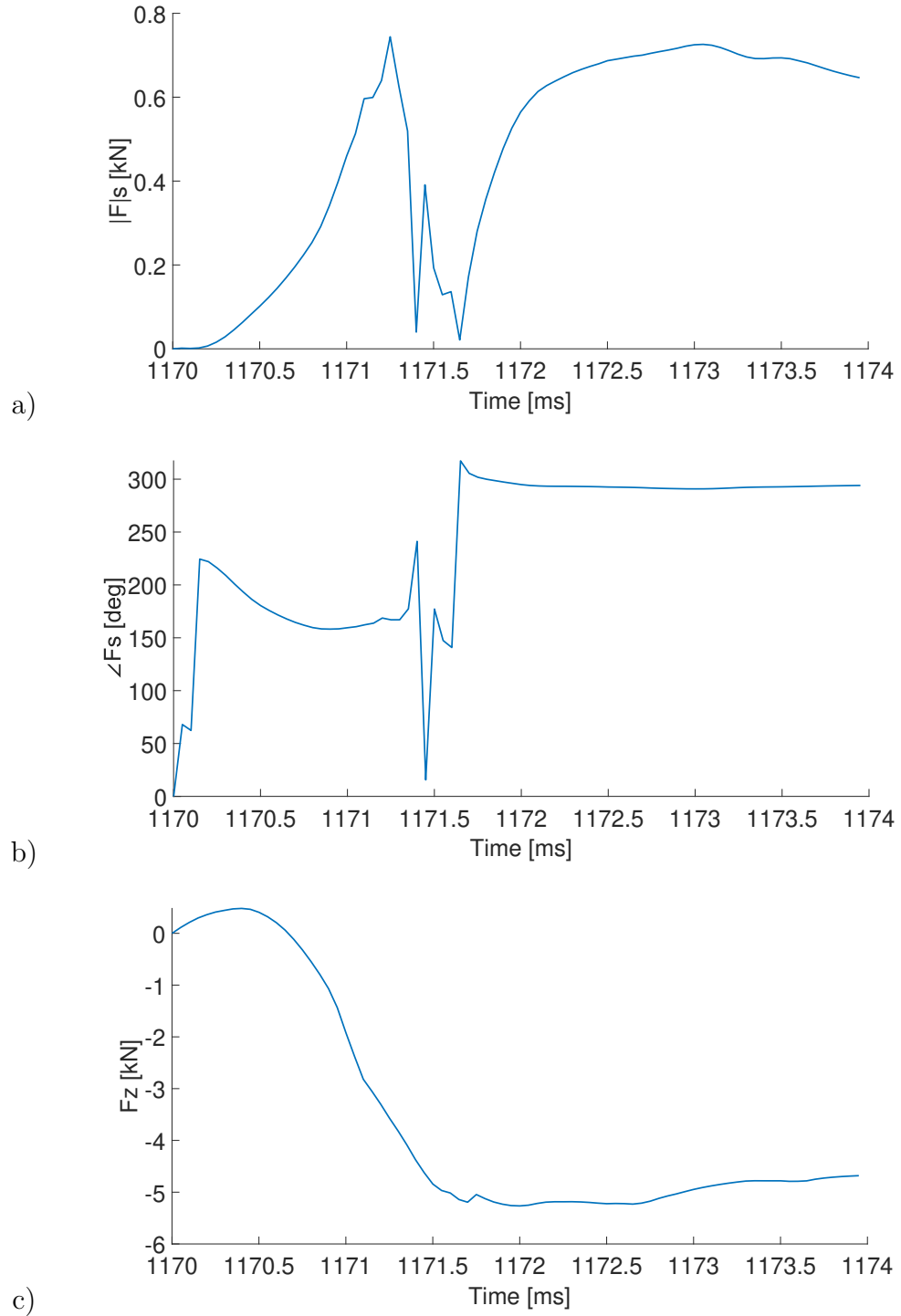
103

a)

b)

c)

Figure 6.13: a) $|F|_s$, b) $\underline{/F}_s$ and c) F_z obtained from the diagnostics data of the shot # 20827
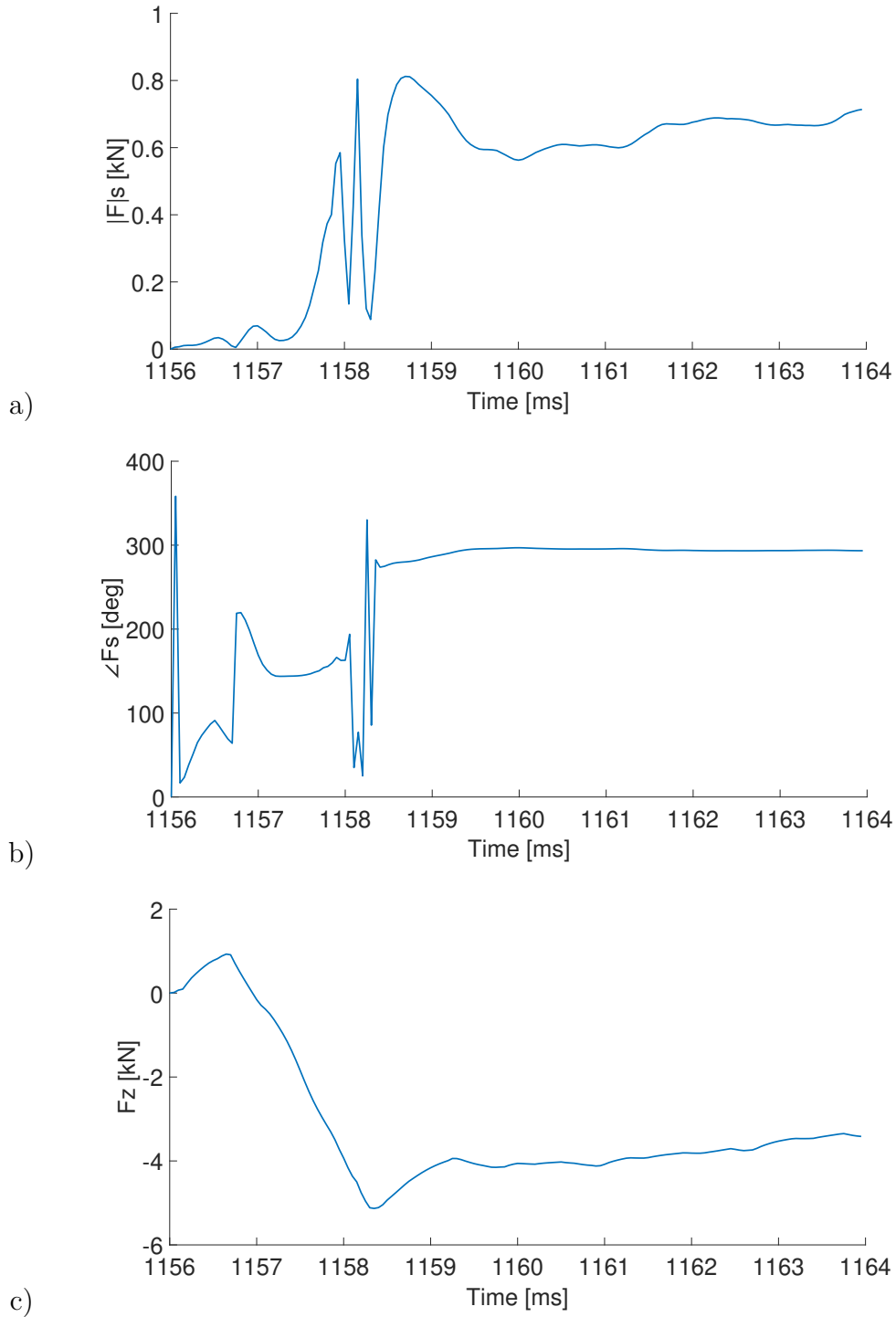
Figure 6.14: a) $|F|_s$, b) $\angle F_s$ and c) F_z obtained from the diagnostics data of the shot # 20828

Bibliography

[1] Markovic, T., Liu, Y. Q., Cahyna, P., Pánek, R., Peterka, M., Aftanas, M., ... & COMPASS Team. (2016). Measurements and modelling of plasma response field to RMP on the COMPASS tokamak. Nuclear Fusion, 56(9), 092010.

BIBLIOGRAPHY

7
Conclusions

T HE technique here proposed has shown a good capability to estimate the total net magnetic forces on a Tokamak vessel, more precisely the COMPASS device, during a disruption phenomena, from the knowledge of the information obtained from the magnetic diagnostics only: the saddle loops and the External Partial Rogowski coils.

In particular, the results obtained from the CarMa0NL simulations data have shown a good agreement between the reference simulated forces and the ones evaluated with the method here proposed, when a high number of virtual diagnostics has been used. A deep analysis concerning the reduction of diagnostics points has been carried out, highlighting the accuracy reduction and the limits of the method, on the prospective of an application on a real set of diagnostics. This last case has been addressed also, showing that the method is capable to estimate the amplitude of the sideways forces with an error of a factor two, and with a greater accuracy the phase and the value of the vertical force.

The tool developed here can be directly used with real COMPASS data as input, taking into account its limitations. In addition, it is absolutely general, and can be applied without important modifications on any device with suitable magnetic diagnostics on the external wall of the vessel.

Naturally, this activity can be expanded and a deep study of methods capable to increase the accuracy can be carried out. Some interesting future activities may be:

- comparison of the results obtained by the actual method with the results from other numerical tools and/or diagnostics data, in order to

increase its reliability and assess its generality;

- application of the method on different disruptions phenomena or on other transient events;

- application of the method on a monitoring system, potentially in real-time, of the forces on the vessel during a plasma discharge;

- application of the method on future devices, such as ITER, DTT, JT60SA, etc.;

- more efficient numerical implementation of the method, e.g. study of the possibility of the exploiting of high parallel computing technique.

In conclusion, this activity represents a contribution in developing a support tool in the design phase and operation of Tokamaks, with regards to the prevention and estimation of possible mechanical damage to the device during disruption phenomena.

A

Publications

A.1 Published and/or presented

1. Albanese, R., Chiariello, A. G., Fresa, R., Iaiunese, A., Martone, R., Zumbolo, P. (2022). Effectiveness of the Chebyshev Approximation in Magnetic Field Line Tracking. Energies, 15(20), 7619.

2. Albanese, R., Bolzonella, T., Chiariello, A. G., Cucchiaro, A., Iaiunese, A., Lampasi, A., Martone R., Piron L., Pizzuto A., Zumbolo, P. (2023). Error Field and Correction Coils in DTT: a preliminary analysis. Fusion Engineering and Design, 189, 113437.

3. Bonotto, M., Abate, D., Bettini, P., Iaiunese, A., Isernia, N., & Villone, F. (2023). Efficient Numerical Solution of Coupled Axisymmetric Plasma Equilibrium and Eddy Current Problems. IEEE Access, 11, 27489-27505.

4. Bolzonella, T., Pigatto, L., Piron, L., Villone, F., Albanese, R., Bonotto, M., ... & Zumbolo, P. (2022, June). Physics based design of a multi-purpose non-axisymmetric active coil system for the Divertor Test Tokamak. In 48th EPS Conference on Plasma Physics.

5. Albanese, R., Chiariello, A. G., Di Grazia, L. E., Iaiunese, A., Martone, R., Mattei, M., ... & Zumbolo, P. (2023). Three-dimensional evaluation of the connection lengths in a Tokamak. Fusion Engineering and Design, 192, 113622.

6. Albanese, R., Iaiunese, A., & Zumbolo, P. (2023). Solution of Grad-Shafranov equation with linear triangular finite elements providing magnetic field continuity with a second order accuracy. Computer Physics Communications, 108804.